DEVELOPMENT OF A NOVEL VARIABLE STIFFNESS DEVICE BASED ON MAGNETO-RHEOLOGICAL ELASTOMERS FOR SOFT ROBOTS

by

Taylan Atakuru

B.S., Mechanical Engineering, Middle East Technical University, 2014

M.S., Mechanical Engineering, Boğaziçi University, 2017

Submitted to the Institute for Graduate Studies in
Science and Engineering in partial fulfillment of
the requirements for the degree of
Doctor of Philosophy

Graduate Program in Mechanical Engineering

Boğaziçi University

2023

ACKNOWLEDGEMENTS

I would like to express my sincere gratitude to my advisor Prof. Evren Samur. This work would not have been possible without him. His expertise and constructive feedback have significantly enriched this work and helped me refine my research ideas. I would like to extend my sincere appreciation to the members of my thesis committee, Assoc. Prof. Can Aydıner, Prof. Nuri Ersoy, Assoc. Prof. Seval Genç, and Assist. Prof. Onur Özcan. I am grateful for their valuable input and the time they dedicated to reviewing my thesis.

I would also like to express my gratitude to Haptics and Robotics Lab family, Şeref, Serhat, Uğur, Berkhan, Rıza, Onur, Cem, Mohammad, Mehdi, Efe, Alican, Bora, Kübra, Timur, Oğuzhan and Fatih. I would like to extend my special thanks to my teammates Burcu and Günay for their contributions and assistance throughout my Ph.D. journey. Furthermore, I would like to thank SMB Lab members, Niccolo, Luca, Lucre, and Cami. I am grateful for their contributions and the collaborative atmosphere they provided me.

I would like to acknowledge the financial support provided by TerriNet. Their assistance has allowed me to focus on my research. I am deeply grateful for their investment in my academic pursuits.

My deepest appreciation goes to my family, Mom, Dad, and Seren. Thank you for your endless love and unwavering support. Without you, this achievement would not have been possible. And to my beloved wife Meral, thank you for the joy and peace you bring to my life.

This project was supported in part by the Boğaziçi University Research Fund under grant numbers 17641 and 19782.

ABSTRACT

DEVELOPMENT OF A NOVEL VARIABLE STIFFNESS DEVICE BASED ON MAGNETO-RHEOLOGICAL ELASTOMERS FOR SOFT ROBOTS

One of the biggest challenges in soft robotics is the variability and controllability of stiffness. Compliance is required for soft robots to enable dexterity and secure interactions with the environment, whereas rigidity is required to transmit forces when necessary. Stiffness variation of soft robots has been achieved through stiffening methods such as antagonistic arrangement of active elements, jamming by vacuum, and viscosity change under magnetic field. The methods can be compared in terms of speed of stiffening and destiffening, modes of stiffening, and stiffness variation. Magnetorheological elastomers (MREs) are effective in response time and suitable for different stiffening modes, such as bending, tension, and compression. However, stiffness variation data can only reach high values if a very high magnetic field is applied. Jamming-based methods appeal due to fabrication, low cost, and stiffness variation. However, the speed of this technology is not particularly remarkable. In addition, it requires an external membrane, creating design complications for system integration. No research that utilizes both methods simultaneously is found in the soft robotics literature. In this thesis, a hybrid method is proposed that combines a jamming-based approach with a viscosity-based one for stiffening of soft robots. The proposed method is innovative because stiffness variation is boosted by exploiting the advantages of magnetic jamming of MREs. In order to prove the proposed method, a number of steps was taken. First, the bending behavior of MREs is analytically, numerically, and experimentally investigated to analyze the effect of volume fraction of magnetic particles on stiffness variation. Second, a multi-layer jamming structure consisting of MRE layers and two flexible Neodymium-Iron-Boron (NdFeB) magnets is developed

to investigate the unique mechanics of magnetic jamming of MRE sheets exploring stiffness change both due to jamming and variable viscoelasticity. Third, a fiber jamming structure consisting of MRE fibers and a flexible NdFeB magnet is developed and integrated into a soft robot, the STIFF-FLOP manipulator. Stiffening tests are performed on the manipulator to prove the concept of magnetic jamming of MRE fibers. Results show that stiffness gain in bending and compression is achieved with the proposed method. Finally, a possible implementation of electronically-controlled magnetic jamming and stiffening is demonstrated on the manipulator which is embedded with electro-permanent magnets. The findings of this thesis show that the proposed hybrid stiffening method combining jamming with viscoelasticity modification is a promising approach to achieve variable and controllable stiffness in soft robots.

ÖZET

YUMUŞAK ROBOTLAR İÇİN MANYETOREOLOJİK ELASTOMER ESASLI YENİ BİR DEĞİŞKENLİ SERTLİK CİHAZININ GELİŞTİRİLMESİ

Yumuşak robot teknolojisindeki en büyük zorluklardan biri sertliğin değişkenliği ve kontrol edilebilirliğidir. Yumuşak robotların çevre ile hünerli ve güvenli etkileşimler sağlaması için yumuşaklık gerekirken, gerektiğinde de kuvvetleri iletmek için sertlik gerekir. Yumuşak robotların sertlik değişimi, aktif elemanların antagonistik düzenlenmesi, vakumla sıkışma ve manyetik alan altında viskozite değişimi gibi sertleştirme yöntemleriyle elde edilmiştir. Bu metotlar, sertleşme hızı, sertleşme modları ve sertlik değişimi açısından karşılaştırılabilir. Manyetoreolojik elastomerler (MRE'ler) yanıt süresinde iyidir ve eğilme, çekme ve sıkıştırma gibi farklı sertleştirme modları için uygundur. Ancak sertlik değişim verileri çok yüksek bir manyetik alan uygulandığında yüksek değerlere ulaşabilir. Sıkıştırma bazlı yöntemleri cazip kılan ise imalat, düşük maliyet ve setlik değişimi özellikleridir. Ancak bu teknoloji kayda değer bir hıza sahip değildir ve dahası bu yöntem, sistem entegrasyonunu karmaşık hale getiren bir vakum poşeti kullanmayı gerektirir. Yumuşak robotlar ile ilgili yapılan akademik çalışmalarda bu iki yöntemin bir arada kullanıldığı bir araştırmaya rastlanmamıştır. Bu tezde, yumuşak robotların sertleştirilmesi için sıkışmaya dayalı bir yaklaşımı viskoziteye dayalı bir yaklaşımla birleştiren hibrit bir yöntem önerilmiştir. Önerilen yöntem MRE'lerin manyetik sıkışmasının avantajlarından yararlanılarak sertlik değişimi yarattığı için yenilikçidir. Bu yöntemi kanıtlamak için birtakım adımlar atılmıştır. İlk olarak, manyetik parçacıkların hacimsel oranının sertlik değişimi üzerindeki etkisini analiz etmek için MRE'lerin bükülme davranışı analitik, sayısal ve deneysel olarak incelenmiştir. İkincisi, hem sıkıştırma hem de viskoelastisite değişkenliği nedeniyle sertlik değişimini kontrol ederek MRE tabakalarının manyetik sıkışmasındaki benzersiz mekaniği araştırmak

için iki adet esnek Neodimyum-Demir-Bor (NdFeB) mıknatıs ile MRE'lerden oluşan çok katmanlı bir sıkıştırma yapısı geliştirilmiştir. Üçüncüsü, MRE'lerden ve bir adet esnek NdFeB mıknatıstan oluşan fiber sıkıştırma yapısı geliştirilmiş ve yumuşak bir robot olan STIFF-FLOP'a entegre edilmiştir. MRE liflerinin manyetik sıkışması durumunu kanıtlamak için robot üzerinde gerekli sertleştirme testleri yapılmıştır. Elde edilen sonuçlar, önerilen yöntem ile bükme ve sıkıştırmada sertlik kazancının olduğunu göstermektedir. Son olarak, elektronik olarak kontrol edilen manyetik sıkıştırma ve sertleştirmenin olası bir uygulaması, sürekli elektro-kalıcı mıknatısların STIFF-FLOP robotuna yerleştirilmesi ile ispat edilmiştir. Bu tezin bulguları, sıkıştırma ve viskoelastisite değişikliğinin birleştirilmesi ile oluşturulan, sertleştirme için önerilen hibrit yöntemin, yumuşak robotlarda değişken ve kontrol edilebilir sertlik elde etmek için umut verici bir yaklaşım olduğunu göstermektedir.

TABLE OF CONTENTS

LIST OF FIGURES

LIST OF TABLES

LIST OF SYMBOLS

a	Cap width
A	Cross sectional area
b	Cap thickness
B_{AlNiCo}	Magnetic flux density of Aluminium-Nickel-Cobalt
B_g	Magnetic flux density in the air gap
B_{NdFeB}	Magnetic flux density of Neodymium-Iron-Boron
B_r	Remnant magnetization
B_{sat}	Saturation flux density
c	Variable dependant on volume fraction
d	The distance between permanent magnets
d_m	Magnet diameter
$\mathbf{D}$	Demagnetization tensor
E	Young's modulus
E_0	Matrix modulus
f	Volume fraction of MREs
F	Analytical holding force of an EPM
F_E	Elastic force
F_m	Magnetic force
g	Air gap
h	Height of an layer
$\mathbf{H}$	Magnetic field
H_m	Axial magnetic field intensity within magnet
H_g	Magnetic field intensity in air gap
I	Area moment of inertia
I_m	Current
$I_{preslip}$	Area moment of inertia before slip
I_{slip}	Area moment of after slip
K	Stiffness ratio

k_E	Elastic stiffness of the beam
k_H	Field-induced stiffness of the beam
L	Length of the beam
L_m	Magnet length
$\mathbf{M}$	Magnetization tensor
M	Mass in friction tests
M_r	Remnant magnetization
N	Number of layers or fibers in the jamming structure
N_m	Coil turn
N_{rods}	Number of magnets in an EPM
P	Resultant force
P_E	Experimental resultant force
$\mathbb{P}_{leak}$	Leakage permeance
U_E	Elastic energy of the beam
U_H	Magnetic energy of the beam
U_T	Total energy of the beam
w	Coil width
y	Tip displacement
$\bar{\chi}$	Effective magnetic susceptibility
δ	Deflection
μ_0	Permeability of the free space
Φ_{leak}	Pole-to-pole leakage flux
θ	Bending angle of the beam

LIST OF ACRONYMS/ABBREVIATIONS

2D	Two Dimensional
3D	Three Dimensional
AlNiCo	Aluminium-Nickel-Cobalt
CIP	Carbonyl Iron Particles
DEA	Dielectric Elastomer Actuator
DIC	Digital Image Correlation
EAP	Electro Active Polymer
EPM	Electropermanent Magnet
ER	Electrorheological
ERE	Electrorheological Elastomer
ERF	Electrorheological Fluid
FEA	Finite Element Analysis
FEM	Finite Element Method
FFA	Fast Fluidic Actuator
LMPA	Low Melting Point Alloy
LMPM	Low Melting Point Material
LMPP	Low Melting Point Polymer
LMPW	Low Melting Point Wax
MIS	Minimally Invasive Surgery
MR	Magnetorheological
MRE	Magnetorheological Elastomer
MRF	Magnetorheological Fluid
N/A	Not Applicable
NdFeB	Neodymium-Iron-Boron
PDMS	Polydimethylsiloxane
PLA	Polyactic Acid
PVC	Polyvinyl Chloride
SEM	Scanning Electron Microscope

SMA	Shape Memory Alloy
SMM	Shape Memory Material
SMP	Shape Memory Polymer
TT	Transformation Temperature

1. INTRODUCTION

Most of the conventional robots today are made of rigid components and materials. Although rigidity enables them to be strong and precise, however, their ability in a complex and unpredictable environment is limited due to rigid links. Robots that are flexible, versatile, and light have benefits especially when used in healthcare, search and rescue, and cooperative human assistance [1,2]. The requirement of adaptability of rigid robots to such challenging ambient conditions has made soft robots a significant research interest in recent years.

Soft robotics deals with robots that are made of materials with low elastic modulus, similar to those found in living organisms [3]. Young's modulus is a useful metric for assessing compliance of robots. Most conventional robots are made of metals and rigid plastics with a modulus greater than one GPa. In contrast, the materials in natural organisms have a modulus on the order of 10^2-10^6 Pa (see Figure 1.1). It means that the materials in conventional robots are three-to-seven orders of magnitude more rigid than the materials in natural organisms. This huge discrepancy is the reason why rigid robots are biologically incompatible and even dangerous for intimate human interaction. Unlike their conventional counterparts, soft robots consist of easily deformable materials such as fluids, gels, soft polymers, etc. These materials exhibit the same rheological and elastic properties as biological matter; therefore, soft robots can remain operational even when squeezed or stretched. This compliance/stiffness matching is crucial, especially in biomedical applications [2,4,5]. Stress concentrations that may cause physical injury or discomfort are eliminated when a soft robot is in contact with human tissue or organs because the surface of soft robots is adequately soft and deformable to distribute forces over a large contact area.

The need to construct soft robots with high deformability and compliance has increased the interest in using unconventional materials and morphologies. The variability and controllability of stiffness are major issues in soft robotics [6]. The stiffness

of a soft robot must be designed as a compromise between being stiff enough to exert substantial forces on its surroundings and precise to perform tasks and being compliant enough to adapt to the environment [7–10].

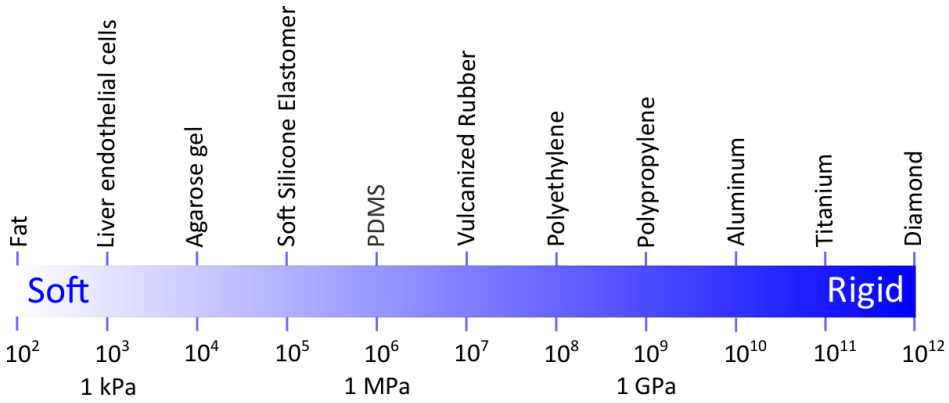

Figure 1.1. Young's modulus for various materials adapted from [11].

1.1. Motivation

The primary motivation behind this thesis is to design and develop a device that provides stiffness variation to soft robots. The device will have a high range of stiffness variation, a fast response time (i.e., high speed of stiffening and destiffening), and less complexity and be suitable for different modes of stiffening such as bending, tension, and compression. The developed device will be stiffness-controllable, flexible, and adaptable, which can be implemented into a soft robot module. There has yet to be research on applying a hybrid stiffening method combining magnetorheological elastomers and fiber jamming. The rationale of this study is to investigate the unique mechanics of magnetic jamming of MRE fibers to obtain a hybrid stiffening method combining viscosity-based and jamming-based methods for stiffness control of soft robots. A higher range of stiffness variation, less complexity, and faster response time is expected.

1.2. Objectives of the Study

The first objective is to investigate the bending behavior of magnetorheological elastomers. Cantilever bending experiments were performed under various external magnetic fields to investigate the stiffness variation of the MREs. MRE samples were manufactured to perform the experiments. The findings indicate that the stiffness of the produced MREs increases with the increasing external magnetic field and dependency on the sample's volume fraction (f).

The second objective is to investigate the unique mechanics of magnetic jamming of MRE layers. A hybrid stiffening method combining a jamming-based method with a viscosity-based method was obtained for the stiffness control of soft robots. The multi-layer jamming structure made of MREs and flexible NdFeB magnets was developed and validated through 3-point bending experiments and finite element simulations. It is aimed to achieve a higher range of stiffness variation, less complexity, and faster response time.

The third objective is to investigate the unique mechanics of magnetic jamming of MRE fibers. Fiber jamming structure composed of a flexible NdFeB magnet and MRE fibers was inserted in the stiffening channel of the STIFF-FLOP surgical manipulator. Stiffening tests on the structure-integrated soft robot were performed as proof of concept and performance assessment. The stiffness change in the structure made an actual soft robot implementation possible.

The last objective is to develop a stand-alone stiffening device in that stiffness change is controlled electronically. The device was composed of MRE fibers and EPM devices and was tested in the stiffening channel of the STIFF-FLOP surgical manipulator. This study can potentially lead to the development of a novel hybrid stiffening device implemented in the STIFF-FLOP, in which stiffness change is supplied and controlled by the proposed stiffening method.

1.3. Thesis Outline

The thesis is structured as follows: In Chapter 1, the background of this study is provided with motivation, and the objectives are outlined clearly. Chapter 2 examines actuation modalities, application areas, and variable stiffness methods used in soft robots in the literature. In addition, it includes a review of magnetorheological elastomers. Section 3 first covers the investigation of MREs' bending behavior under a magnetic field. Second, an overview of the layer jamming of MREs is presented together with the FEA study. Third, the fiber jamming of MREs is investigated in the stiffening tests using the STIFF-FLOP surgical manipulator. Finally, a novel variable stiffness device is developed using MRE fibers and electropermanent magnets (EPMs). Chapter 4 is dedicated to the results of the cantilever bending experiments, the multilayer jamming structure, the fiber jamming structure, and the variable stiffness device used in a soft robot implementation. Chapter 5 emphasizes the contributions made by this study and outlines the scope of future work.

2. LITERATURE REVIEW

2.1. Soft Robotics

Soft robotics is an emerging field that explores the design, development, and application of robots with soft and flexible materials. This section is dedicated to providing an overview of the current state of actuation mechanisms of soft robots and various soft robotics applications.

2.1.1. Actuation

Yasa *et al.* [12] highlights the various actuation modalities that are frequently used in soft robotics. Actuators can be considered as the artificial muscles of soft robots, enabling them to deform and exhibit movement. The choice of actuation modality plays a significant role in shaping soft robots' design, fabrication, modeling, control, and overall performance. This section examines the most promising actuation modalities for soft robotics. These include fluidic actuation, electrostatic actuation, thermal actuation, and magnetic actuation. These modalities are investigated to understand their impact on soft robots' design and fabrication processes. Each actuation modality exhibits unique characteristics that must be properly considered to achieve desired performance and functionality in soft robotic systems.

2.1.1.1. Fluidic Actuation. Fluidic actuation is a widely used modality for achieving controlled deformation in soft robots. It involves manipulating the fluidic pressure within the internal inflatable cavities of a soft robot to enable motion. Soft robots designed for fluidic actuation primarily consist of elastomeric materials, with inextensible reinforcement layers (such as fibers, fabrics, or stiffer materials) surrounding the inflatable cavities. These reinforcements restrict the direction of deformation, facilitating the desired motion. By pressurizing and depressurizing the internal cavities with fluids like air or water using pumps, the internal fluidic stress causes the robot's body to

deform. The working mechanism is depicted in Figure 2.1. The deformation rate can be adjusted by controlling the amplitude and duration of the fluidic pressure applied to each cavity.

The design of inflatable cavities and surrounding structures can vary depending on the intended tasks such as cylindrical, pleated, or ribbed [13–15]. These design choices directly influence the actuation speed of the soft robot. To achieve faster actuation, reducing the volume of fluid required for inflating the cavities is beneficial, enabling rapid changes in internal pressure [14]. Additionally, each segment's morphology has advantages and disadvantages, impacting the robot's overall performance and operational lifespan [15]. Inextensible reinforcement layers, also known as constraint layers, are employed to control the direction of deformation. These layers can be achieved by increasing the thickness of elastic materials or by using stiffer materials or inflexible fabrics. By incorporating constraint layers, the soft robot's structure becomes more robust and capable of precise and controlled movements. Hawkes *et al.* [16] developed a growing soft robot that utilizes air pressure for propulsion and navigation of the robot. Additionally, Tutcu *et al.* [17] utilized almost the same principle and developed a growing soft robot that can navigate in three-dimensional space. McDonald and Ranzani *et al.* [18] explored the current advancements in the onboard control hardware used in soft fluidic robots.

Fluidic actuation offers several benefits. It enables a wide range of motion, such as bending, elongation, and twisting. Additionally, it generates substantial forces. Furthermore, fluidic actuation does not require a continuous power supply to maintain the robots in their actuated state. By closing their valves, the robots can remain in that state without the need for constant power. However, fluidic actuation also entails certain drawbacks. The main drawback of fluidic actuation is its vulnerability to punctures. In addition, achieving precise control is challenging due to the nonlinear material response.

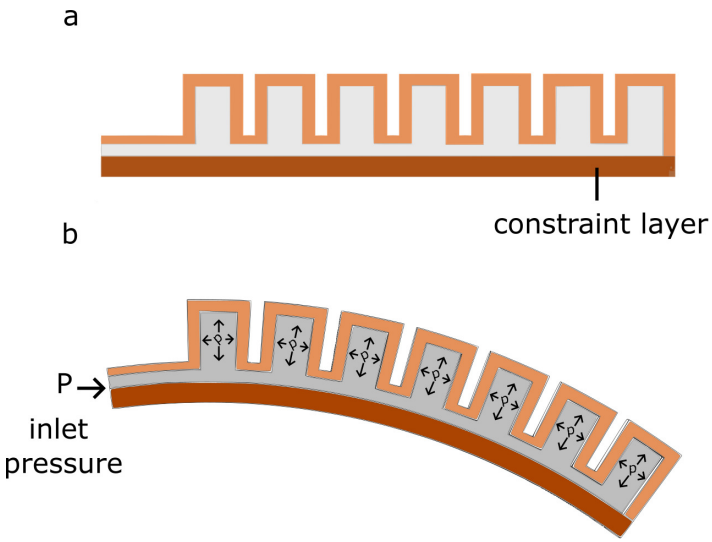

Figure 2.1. Schematic representation of fluidic actuation. (a) There is no inlet air or liquid in the inflatable cavity. (b) Actuation is caused by the fluidic pressure P inside the inflatable cavities of soft robots.

2.1.1.2. Electrostatic Actuation. Electrostatic actuation directly converts electrical energy into deformation within soft bodies. The actuator is composed of two opposing electrodes separated by a dielectric material (see Figure 2.2). Dielectric elastomer actuators (DEAs) utilize attractive electrostatic forces acting on two opposing stretchable electrodes. These electrodes are separated by a compliant dielectric layer composed of solid material [19]. Depending on the design, material properties, and desired actuation strains, DEAs can be activated by applying a voltage to the opposing electrodes, typically ranging from 0.3 to 27 kV [20,21]. The opposing electrodes attract each other when actuated, causing the solid dielectric material layer to compress or squeeze. Depending on their specific arrangements, DEAs exhibit various deformation patterns, including contraction, elongation, and twisting [22]. Controlling DEAs is relatively straightforward due to the direct relationship between the applied voltage and the resulting deformation magnitude. Additionally, the elastomeric forces exerted by the dielectric materials assist in resetting the shape of DEAs when the actuation voltage is reduced.

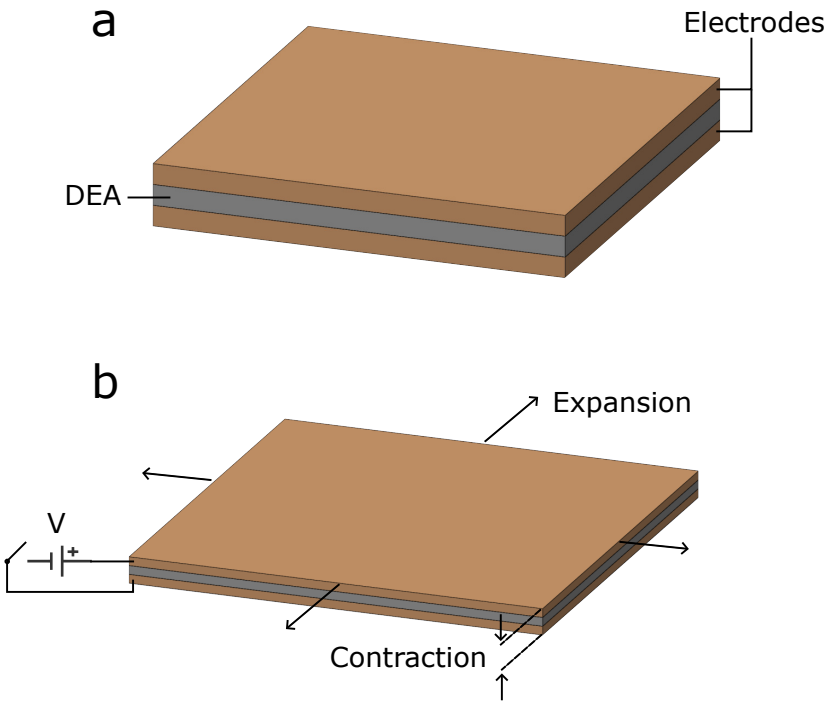

Figure 2.2. Schematic representation of electrostatic actuation. (a) A dielectric elastomer is sandwiched between two compliant electrodes. (b) Electrostatic forces cause deformation when a voltage is applied to the electrodes.

2.1.1.3. Thermal Actuation. Shape memory alloys (SMAs) are temperature-sensitive composite materials that are commonly used as artificial muscles for soft robots. They exhibit the shape-memory effect and the superelastic effect [23]. When they are heated above their transformation temperature (TT), deformation occurs, and the alloys exhibit either the one-way memory effect, where they retain the recovered shape below (TT), or the two-way memory effect, where they restore themselves to their original shape. The superelastic effect, on the other hand, involves the deformation recovery during a mechanical load-unload cycle at temperatures exceeding (TT).

To enable actuation, SMAs are utilized as structural components within the robot's elastomeric matrices. They are deformed, thereby driving soft robots' movement through shape changes induced by Joule heating. The working mechanism can be seen in Figure 2.3. It is stated in [24] that their deformation capacity can exceed 300% when designed in a spiral shape. Most SMA-based soft robots described in the liter-

ature rely on electrical stimulation, resulting in the requirement of tethering. SMAs have the disadvantage that their actuation depends on temperature changes, which ultimately lowers their energy efficiency.

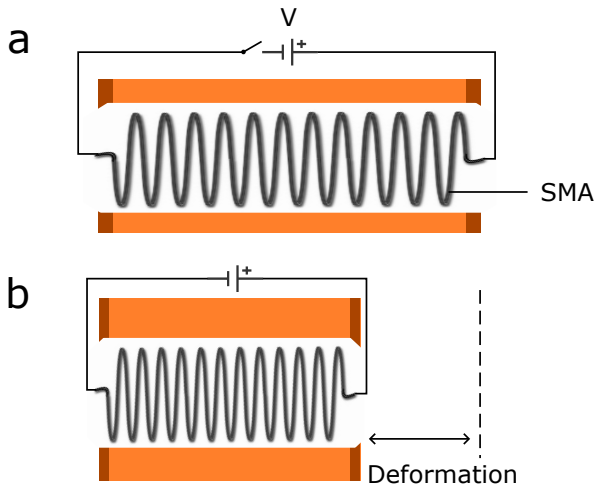

Figure 2.3. Schematic representation of thermal actuation. (a) An SMA is embedded into an elastomer matrix in a soft robot. (b) Joule heating causes SMAs to change shape, which results in activation.

2.1.1.4. Magnetic Actuation. Magnetic actuation is commonly achieved by aligning magnetic materials embedded within flexible structures in response to external magnetic fields [25, 26]. An illustration of the working mechanism can be seen in Figure 2.4. This actuation principle enables the development of compliant and untethered soft robots capable of operating safely in delicate and unstructured environments, including the brain and inner body cavities [26, 27]. Soft robots utilizing magnetic actuation incorporate microscopic ferromagnetic materials integrated into elastomeric matrices. The controlled spatial alignment of the magnetic domains within these materials during fabrication plays a crucial role in achieving the desired deformation and motion of the soft robot's body.

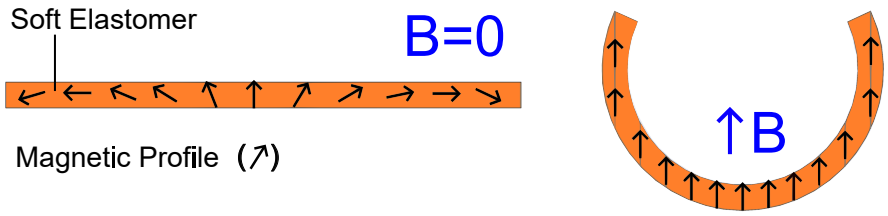

Figure 2.4. Schematic representation of magnetic actuation. Magnetic particles are embedded into a soft and flexible elastomer. The particles tend to align themselves in the direction of the applied external magnetic field, resulting in deformation.

2.1.2. Application Areas

Soft robots offer various benefits in contrast to traditional robots. These include safe human-machine interaction, adaptability to the outside environment, grasping fragile and delicate objects, cost-effectiveness, etc. These advantages cause them to be used in a wide range of applications. Some of the application areas are listed below:

(i) Industry: Soft grippers are used to perform certain tasks in the industry, such as pick-and-place operations, assembly, and handling of delicate objects. They offer safer human-robot collaboration thanks to their compliance and flexibility.

(ii) Medicine and Healthcare: Soft robots have the potential for gentle interaction with the human body. They have the ability to perform certain surgical operations in the medical field, such as minimally invasive surgery, rehabilitation, prosthetics, and wearable assistive devices.

(iii) Search and Rescue: Soft robots can navigate through complex and dangerous environments due to their compliant and deformable features, which makes them valuable in search and rescue operations.

(iv) Agriculture: Soft robots in agriculture are designed to perform tasks such as harvesting crops, inspecting plants, or handling delicate agricultural produce with minimum damage.

2.2. The STIFF-FLOP Manipulator

As an intended study, the stiffening device is proposed for the STIFF-FLOP manipulator [28]. The STIFF-FLOP, abbreviation of STIFFness controllable Flexible and Learn-able manipulator for surgical OPerations, is an EU-funded project. Inspired by an octopus, a soft robotic arm that can reconfigure itself and stiffen by hydrostatic actuation in MIS was designed and fabricated. The designed manipulator has three pneumatic chambers and a central channel that can be used to perform certain tasks, such as carrying camera cables if mounted or a different implementation of a stiffness modulation mechanism or system. Flexible fluidic actuators (FFAs) are used to actuate the three chambers, which enables the manipulator to squeeze and elongate without being damaged and perform omnidirectional bending. These features of the robot make it an excellent candidate for performing MIS operations. The STIFF-FLOP surgical manipulator can be seen in Figure 2.5.

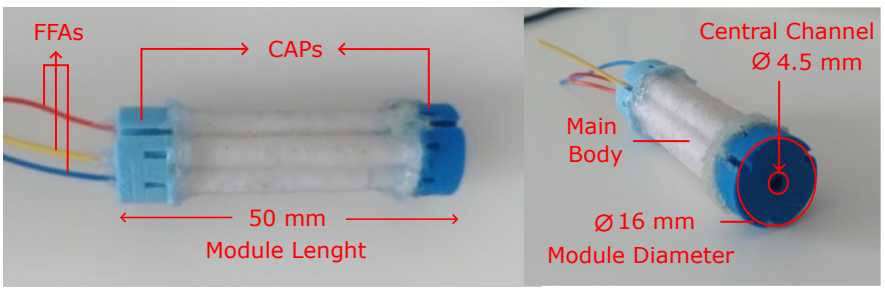

Figure 2.5. The STIFF-FLOP surgical manipulator developed by by Cianchetti *et al.* [28].

Various mechanisms have been used to achieve stiffness variation in the STIFF-FLOP manipulator. The stiffness of the manipulator is increased by 37% in [29] and 12.4% in [30] using the granular jamming method. Granular materials were inserted into the central channel of the manipulator. The diameter of the central channel is 8 mm in these studies. In [31], braided tendons and granular jamming were used in the central channel. When there is no tension in the tendons, the stiffness of the STIFF-FLOP manipulator was increased up to 17.4% in bending configurations. When there is tension in the tendons, it can increase the change in stiffness by up to 30.7%.

These mechanisms offered adequate stiffness variation ranges; however, the drawbacks, particularly for MIS operations, were the requirement for pneumatic input and the longer unstiffening time. These drawbacks can be removed using a hybrid stiffening device containing MRE fibers with an internal magnetic field controller in the STIFF-FLOP's central channel. The STIFF-FLOP manipulator has yet to be subjected to this promising stiffening technology. It might be a cutting-edge design that enables more effective MIS operations by reducing system complexity overall and eliminating the need for a pneumatic input.

2.3. Classification of Stiffening Mechanisms

Various methods have been proposed to achieve variable stiffness in the literature. Manti *et al.* [6] summarized on-demand stiffening methods under two main approaches based on soft actuation technologies (see Figure 2.6). Those are active actuators arranged in an antagonistic manner and semi-active actuators.

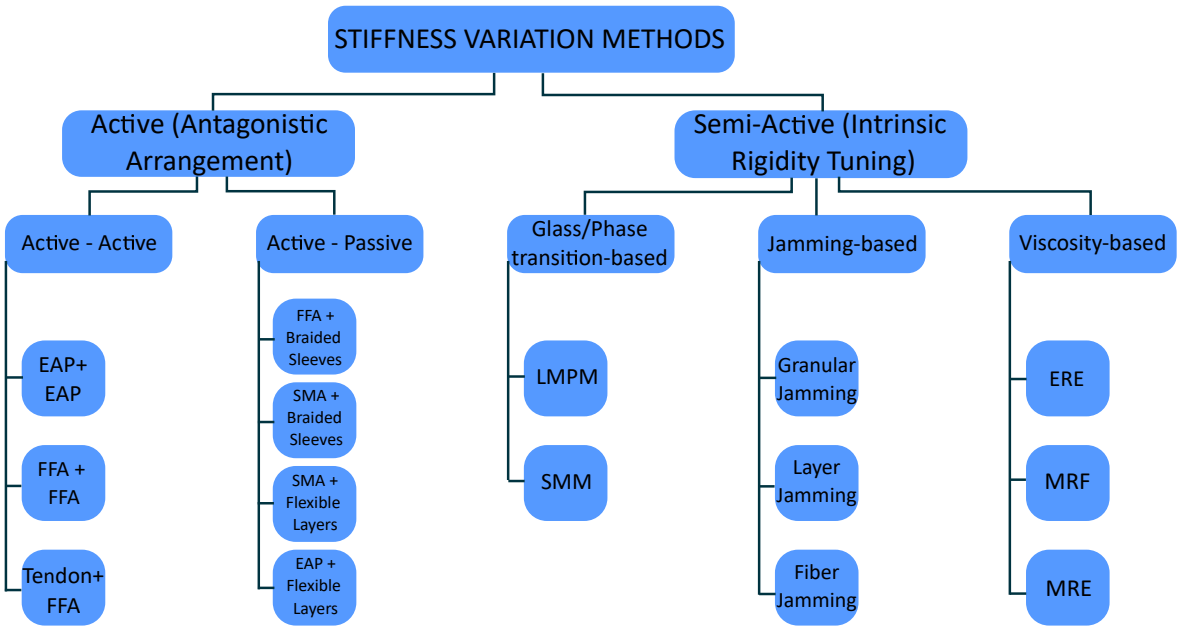

Figure 2.6. Various stiffening mechanisms are classified.

2.3.1. Antagonistic Arrangement

The antagonistic arrangement provides variable stiffness through the use of active elements that are applied to contrast each other or are coupled with passive structures.

2.3.1.1. Active-Active. Carpi *et al.* [32] used electroactive polymers (EAPs) to vary stiffness by controlling applied voltage only. They developed a variable stiffness transducer utilizing the EAP technology to develop hand orthoses for hand rehabilitation. Another example of active actuation technologies is the utilization of flexible fluidic actuators (FFAs), which employ elastomeric chambers designed to create asymmetric deformations in specific directions when inflated. Correll *et al.* [33] reported that a stiffening effect is generated without inducing bending when the FFAs are arranged in a trilayer structure. The structure is composed of two fluidic channels and a sandwiched constraint layer in the middle. When both sides of the trilayer design are inflated simultaneously, the structure experiences an increase in stiffness without bending. This allows for precise control over the mechanical response and enables the structure to maintain its overall shape while adjusting its stiffness characteristics. In addition, Suzumori *et al.* [34] developed a multi-directional bending mechanism that can change its stiffness by contracting and extending flexible fluidic actuators. A combination of different actuation techniques, such as tendon-driven actuators coupled with a pneumatic chamber like the ones in [35–38] is used for variable stiffness. In this method, the structure's stiffness is determined by the pressure inside the fluidic chambers and the tension in the tendons. The stiffness of the structure can be tuned by adjusting the pressure and tension. Higher pressure in the chambers and tension in the tendons result in a stiffer structure, while a compliant structure is obtained if the pressure and tension are reduced.

2.3.1.2. Active-Passive. If a passive structure is coupled with one of the actuation technologies, stiffness can also be changed. McKibben actuator is a typical type of FFAs consisting of a flexible fluidic chamber covered with a braided structure (sleeve

with fibers) with a specific geometry. When the angle of knitted fibers is 54.7 degrees, the expansion of the chamber is prevented [34], even if high pressure is applied. The actuator extends upon pressurization if the angle is less than 54.7 degrees, while it contracts if it is more than that value. The devices in [7, 39] coupled with braided sleeves are able to change their stiffness by air pressure. However, McKibben actuators have a miniaturization problem, especially for achieving actuation at smaller scales due to the size of the pneumatic pipes and manufacturing limits. In such cases, SMAs offer advantages over fluidic actuators. The biomimetic robots in [24, 40] use SMA with braided sleeves to control position and stiffness. One drawback of this method is that SMA actuators are connected to a braided sleeve in order to couple their antagonistic action. Alternatively, simpler methods can be employed to achieve stiffness variation. For instance, Henke and Gerlach [41] designed a multi-layered variable stiffness device that utilizes SMA wires. When the wires are activated, in which the layers are in form-closure, the flexural stiffness of the entire structure is enhanced. On the other hand, the structure's stiffness is decreased when the wires are not activated. The same principle is utilized with dielectric elastomer actuators (DEAs). EAP with flexible layers is used in [42] to enable stiffness change.

2.3.2. Intrinsic Rigidity Tuning

The other variable stiffness mechanism is the use of semi-active actuators, whose working principle relies on the change of mechanical properties of constitutive materials. Semi-active actuators can be classified into three methods based on their working principle. These are glass or phase transition-based methods, jamming-based methods, and viscosity-based methods.

2.3.2.1. Glass or Phase Transition-based. Low melting point materials are a class of glass or phase transition-based methods. They can be either wax, polymer, or alloy. Cheng *et al.* [43] developed a novel variable stiffness device using a thermally tunable and wax-coated soft material for soft robotic applications. Performance tests were performed on a wax-coated foam (polyurethane) beam. This work achieved a wide

range of stiffness variation (three orders of magnitude). The beam undergoes a phase transition from a rigid state to a compliant state and vice versa by controlling the temperature. The temperature change is supplied by a copper wire wrapped around the beam. The use of wax as a stiffness variation material offers several advantages. For instance, they are cheap, commercially available, and higher stiffness variation can be obtained. However, the speed of stiffening is not remarkable since it depends on thermal conditions. McEvoy and Correll [44] used a glass transition-based polymer, polycaprolactone (PCL) (melting point around 64 degrees), to drastically change the elastic modulus of their composite through external thermal input. The stiffness of the composite was tuned locally by Joule heating.

The temperature-sensitive alloys can also be promising alternatives to wax and polymers since they provide higher stiffness variation. Furthermore, they can be considered as a heat source through electric energy if a proper encapsulation is supplied to contain any potential liquid pouring, thereby eliminating the need for an external heat source. Shan *et al.* [45] developed a stiffness-tunable composite device. The device is made of an LMPA embedded in an elastomer, where the alloys provide controllable stiffness by Joule heating. Schubert and Floreano [46] developed a variable stiffness device using low melting point alloy (LMPA) embedded in a soft, flexible elastomer. The body of the device is made of polydimethylsiloxane (PDMS) and has microchannels in it. The molten alloy was filled into these channels. The stiffness of the device is tuned by using Joule heating. The device demonstrated a relative stiffness change higher than 25 times. In another study, Shintake *et al.* [47] developed a variable stiffness actuator consisting of DEAs and LMPAs embedded in an elastomer. The DEA was used for actuation, while the LMPA was responsible for the stiffness modulation. Similarly, shape memory materials can be used as stiffness variation materials, such as shape memory polymers in [48, 49] and shape memory alloys in [50]. However, the stiffening and de-stiffening take too much time to reach desired values, and they require heating elements which increase the complexity of the structures.

2.3.2.2. Jamming-based. Jamming-based technologies have been of interest to soft roboticists since they are simple to scale, easy to fabricate, inexpensive, and actuated by various mechanisms. Liu and Nagel [51] initially introduced the concept of jamming. Later, it has been described frictional interactions by nearest-neighbor jamming particles [52, 53]. In other words, an increase in relative shear stress between the particles results in a phase change in the structure. This change is generally supplied by external pressure. The structure is in the jammed (stiff) state when uniform pressure is applied, whereas it is in the unjammed state (compliant) in the absence of pressure. Thus, the structure makes a transition from a compliant state to a rigid state. Jamming structures have used elements with varying geometries, such as grains, layers, and fibers. The response of these structures upon loading can be seen in Figure 2.7.

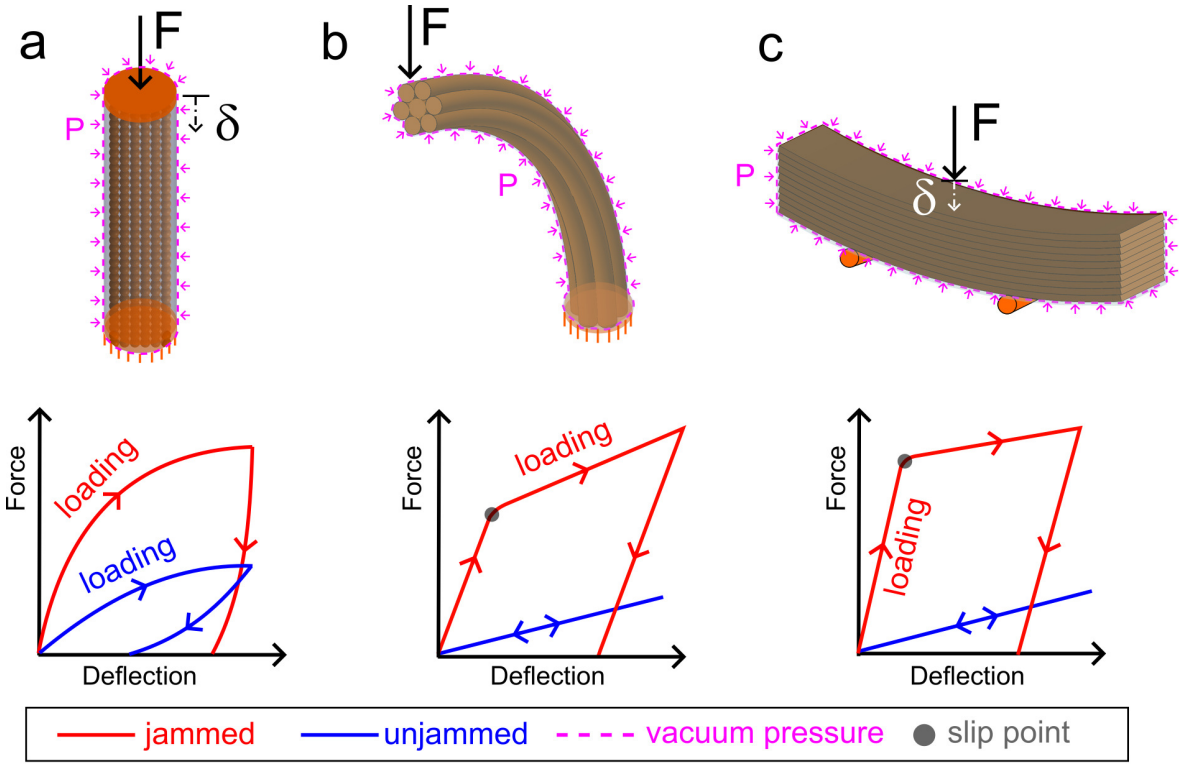

Figure 2.7. Schematic representation of the fundamental mechanical behavior of the jamming structures under loading. (a) Granular jamming structure under compression, (b) fiber jamming structure in cantilever bending, and (c) layer jamming structure in three-point bending configuration.

The stiffness behavior of the structure was explained physically as three stages of deformation [54]. The layers are cohesive during the pre-slip regime—the entire structure functions as one cohesive beam instead of separate, independent layers. The stiffness of the jammed structure is high as long as the shear forces induced in the layers are able to exceed the frictional forces caused by the magnetic forces. Beyond that point, stiffness starts to decline. In this transition regime, slipping starts to occur on the inner slip surfaces of the structure while shear forces are still at a level that cannot exceed the friction force on the outer slip surfaces. All layers are in slip during the full-slip regime, and the structure has the lowest stiffness value.

Granular jamming structures consist of granular materials in an air-tight envelope. The granular materials can freely move with respect to each other in the unjammed state. On the other hand, they become constrained when pressure is applied. Manti *et al.* [6] reported that granular jamming structures demonstrated impressive stiffness changes (up to 40:1), which makes them well-suited for robotic applications such as soft grippers and haptic interfaces. For instance, Brown *et al.* [55] developed a universal robotic gripper utilizing granular jamming to grasp complex-shaped and fragile objects. The operation principle is that the gripper conforms to a shape of an object to be picked up, a negative pressure is applied, then the object is manipulated. Cheng *et al.* [56] developed a multi-segment soft manipulator that utilizes granular jamming for achieving local stiffness control. As mentioned in Section 2.2, Cianchetti *et al.* [28] utilized a granular jamming principle to modulate the stiffness. The manipulator is composed of a silicone-based main body and an external braided structure. The body has three fluidic chambers and a stiffening chamber at the center. The stiffness of the manipulator was modulated through the use of coffee powder as granular material in the stiffening chamber.

Layer jamming consists of layers of compliant materials in an airtight envelope. When no vacuum is applied, the layers move freely with one another, and the structure's stiffness is generally relatively low. The stiffness increases dramatically by using vacuum pressure due to the friction interaction between the layers. It has several ad-

vantages over granular jamming. It offers a stiffness increase without a substantial change in volume, potentially more compact designs, and precise stiffness control. In addition, it can provide better stiffness variation due to the fact that the increased contact area between the overlapping layers results in a higher friction force. Kim *et al.* [57, 58] developed a snake-like manipulator based on the layer jamming principle to be used in MIS operations. The stiffness of the manipulator was tuned by overlapping the layers in the joint. Ou *et al.* [59] introduced layer jamming technology that enables the design of stiffness-tunable thin sheet interfaces. In this study, five different designs for layer structures were proposed, and the effect of different jamming materials was investigated to control the deformability of the interfaces. In addition, the benefits of utilizing layer jamming were demonstrated by developing three application prototypes such as stiffness-changing display, deformable furniture, and jamming shoe. Narang *et al.* [60] developed an analytical model for a two-layer jamming structure and a finite element model for a multilayer jamming structure.

Fiber jamming, on the other hand, is composed of longitudinal fibers enclosed in an airtight envelope. The fibers can rearrange like grains along one plane, whereas they slide with respect to each other like layers on the two other orthogonal planes. This property makes fiber jamming very useful in applications in which variable bending stiffness in more than one direction is needed, such as surgical operations and endoscopes [61–63]. Recently, Arleo *et al.* [64] developed a stiffness tunable actuator utilizing fiber jamming principle. They have achieved a stiffness ratio of up to 21.3.

According to Euler-Bernoulli beam theory, the bending stiffness depends on Young's modulus (E) and area moment of inertia (I). For the layer jamming structure, the area moment of inertia during the pre-slip region would be $I_{preslip} = bN^3h^3/12$, whereas it is the sum of the independent layers after the slip $I_{slip} = bNh^3/12$, resulting N^2 stiffness ratio between the unjammed and jammed structure. Where N stands for the number of layers in the jamming structure, b and h are the width and height of each layer, respectively. On the other hand, the theoretical modeling of fiber jamming structures under bending is not straightforward. Vasios *et al.* [63] highlighted various

possible packing arrangements. The highest packing density for circles is obtained with hexagonal packing. If we assume negligible gaps between the fibers, the change in stiffness of the fiber jamming structures can theoretically be calculated. The I during the pre-slip region would be $I_{preslip} = 5\sqrt{3}N^2d^4/144$, while it becomes $I_{slip} = \pi N d^4/64$ after the slip, resulting $1.23N$ stiffness ratio. The theoretical calculations indicate that less stiffness change is achieved with the fiber jamming structures. It is an expected result since the fibers are stacked in more than one direction.

2.3.2.3. Viscosity-based. The last method under semi-active actuators is the use of viscosity-based materials. Magnetorheological (MR) and electrorheological (ER) materials can undergo stiffness variations because of the applied magnetic and electrical fields, respectively. ER fluids are less common because of the drawbacks of using ferroelectric particles [65]. Besides, the ER elastomers are not widespread since it does not provide a useful stiffness change [66]. Magnetorheological fluids (MRFs) have the ability to change their rheological properties a magnetic field is applied. McDonald *et al.* [67] developed a valve utilizing MRFs for flow control of soft robots. Gaeta *et al.* [68] introduced a magnetically-controlled stiffening technique utilizing MRFs and jamming-based stiffening methods. Disadvantages like particle settling and controllability issues limit the use of MRFs, which makes another MR material more suitable for tunable stiffness: Magnetorheological Elastomers (MREs) [69, 70]. MREs overcome the problems that accompany the applications of MRFs. They exhibit a unique field-dependent material property when exposed to a magnetic field. Their stiffening and compliance speeds are higher than the other proposed methods, meaning they can provide fast responses (in milliseconds) and are more controllable [70, 71]. These features indicate that MREs have significant potential as a stiffness variation material.

2.3.3. Comparison of Stiffening Mechanisms

The state-of-the-art stiffness variation methods in the literature can be compared in terms of speed of stiffening and destiffening, modes of stiffening, and stiffness variation. Magnetorheological elastomers are effective in terms of the speed of stiff-

ening/destiffening and are suitable for different modes of stiffening, such as bending, tension, and compression. However, stiffness variation data can only reach high values if a very high magnetic field is applied to the material. Layer jamming technology is appealing due to fabrication, low cost, and stiffness variation. However, the speed of this technology (in seconds) is not particularly remarkable [6]. Moreover, the chosen actuation method can negatively affect the jamming structure's performance. A vacuum is practical because it can maintain constant isotropic pressure inside a jamming structure. However, it calls for a tethered external membrane, which can complicate system integration during design.

2.4. Magnetorheological Elastomers

Magnetorheological elastomers are composite materials that contain magnetic-field sensitive particles dispersed or arranged in a particular direction within an elastomer matrix [72]. The particles show a magnetorheological (MR) effect in the presence of a magnetic field, which provides a field-dependent material property to the material, such as controllable modulus and damping. This property is removed from the material in the absence of a magnetic field. MREs exhibit superior performance compared with another member of the MR material family, MR fluids, which makes them a perfect candidate for various applications [71]. MREs overcome the problems that accompany the applications of MR fluids, such as environmental contamination, deposition, and sealing issues. MREs are composed of three main components. Those are: an elastomer matrix, additives, and magnetic particles [73,74]. The magnetic particles should have low remanent magnetization, high saturation magnetization, and high permeability [75]. MR effect is maximized when the high permeability of the particles is used in the elastomer matrix due to a strong interparticle attraction [73]. The most commonly used magnetic particle is Carbonyl Iron Particles (CIP). The particles' shape significantly affects the performance of MREs [76]. The various forms of CIPs, including spherical shapes [77–79], irregular structures [80, 81], rod-like configurations [82], and plate-like arrangements [83–85], have demonstrated a influence on the effectiveness of MRE.

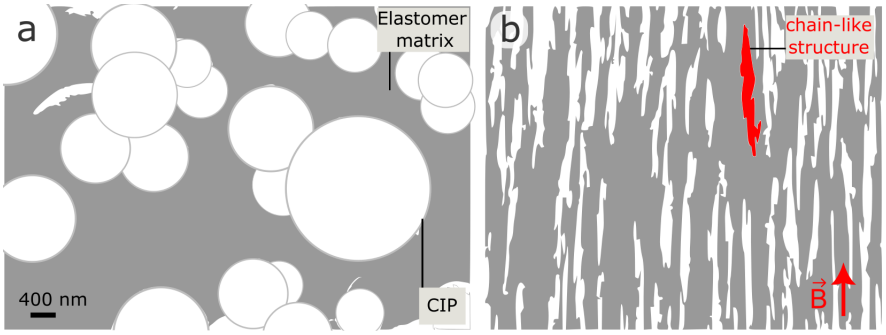

Figure 2.8. SEM image of CIP in the absence of magnetic field (a), chain formation under uniform magnetic field (b).

MREs can be classified into two categories: anisotropic MREs and isotropic MREs. The magnetic particles form a chain-like structure as the magnetic field is induced during the curing process in anisotropic MREs, whereas they are uniformly dispersed in isotropic MREs. An illustration of a scanning electron microscope (SEM) picture of the CIPs is shown in Figure 2.8.

Fabrication of both anisotropic MREs and isotropic MREs are shown in Figure 2.9. Firstly, silicon rubber as an elastomer matrix, silicon oil as an additive, and iron particles as magnetic particles are mixed thoroughly into a homogenous mixture. Second, air bubbles inside the mixture are removed through a vacuum chamber as in [73,86] or by heat treatment as in [87]. Third, the isotropic MRE is cured without a magnetic field, while the anisotropic MRE is cured with an external magnetic field. A strong magnetic field, usually above 0.8 T, is required to form a chain-like structure in the matrix along the direction of the magnetic field [87–89]. During the curing process of both isotropic MRE and anisotropic MRE, the temperature must be kept constant to maintain the flexibility of the material [87,88]. As for the friction properties of MREs, there are very few studies on the coefficient of friction. Li *et al.* [90] analyzed magnetic field influences on friction properties of MRE materials using a macroscopic experimental method. However, using MREs in a jamming structure for stiffness variation in soft robots has yet to occur in the literature.

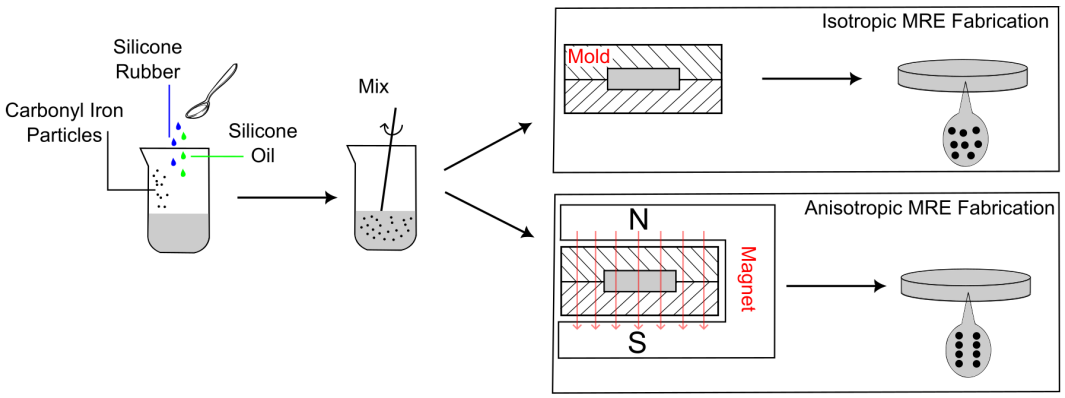

Figure 2.9. Fabrication process of anisotropic and isotropic MRE samples.

2.4.1. Historical Overview of MREs

Rabinow [91] first explored the MR effect in magnetorheological fluids (MRFs) in 1948. However, Rigbi and Jilken [92] conducted preliminary tests on MREs in 1983. In the initial stages of investigating MREs, the emphasis was on studying their dynamic small strain properties. Jolly *et al.* [93], and Ginder *et al.* [94] examined the changes in storage modulus and natural frequency in 1999. In their study, the developed quasi-static model was used to explain the modulus change inside of an MRE. Experimental testing was conducted to analyze the elastomer composite's material properties with ferrous particles inserted in a polymer matrix under a magnetic field. Since the early 2000s, there has been a notable increase in interest regarding MREs, with a particular emphasis on the investigation of their dynamic shear properties under small strain conditions.

Ginder *et al.* [95] in 2002 and Zhou and Jiang [96] in 2003 also investigated the magnetostrictive behavior of MREs. Diguet *et al.* [97] measured the magnetostriction of MRE by approximately 10% in 2010. Gong *et al.* [98] in 2012 measured the out-of-plane deformation of MRE optically using digital holographic interferometry. Stepanov *et al.* [99] in 2013 reported a large-scale deformation (such as the 250% elongation in a non-uniform magnetic field) with an MRE with a low Young's modulus of around 10 kPa.

Kallio [73] (2005) investigated the mechanical and viscoelastic behavior of isotropic and anisotropic MREs. He focused on the alterations in MREs' elastic and vibration-damping properties under magnetic field. Additionally, the study aimed to examine the impact of magnetic particle alignment on the overall composite properties of the MREs. Li *et al.* [100] (2009) highlighted the importance of MREs due to their recognized potential as sensing materials. Since then, there has been a growing interest in exploring the magnetic and electrical properties of MREs. Caglar [101] (2008) investigated the sensing behavior of MREs experimentally. Bica [102] (2009) demonstrated that the resistance of magneto-rheological elastomers (MREs) increases in response to higher magnetic fields and compressive forces. Boczkowska and Awietjan [103] (2012) examined the magnetization curves of MREs and observed a strong MR effect in the magnetic properties of anisotropic MREs. Li *et al.* [104] (2013) explored the sensing capabilities of MREs under various loading conditions and found, experimentally and theoretically, that anisotropic MREs demonstrate higher MR effects than isotropic MREs. Zhou *et al.* [105] (2013) investigated the dynamic equi-biaxial fatigue behavior of MREs (both isotropic and anisotropic MREs) using a bubble inflation test system. Schubert [106] (2014) performed various large-strain experiments with and without magnetic fields to characterize MREs. Constitutive models that capture the behavior of MREs were developed through the use of experimental data.

2.4.2. Applications of MREs

Li *et al.* categorized the devices that use MREs into three basic modes of operation: (a) shear mode, (b) squeeze and elongation mode, and (c) field-active mode. The modes are illustrated in Figure 2.10. Devices operating in shear mode typically include vibration absorbers [107–110] and vibration isolators [87, 111, 112]. In these devices, the MR material experiences shear forces that induce changes in its rheological properties, leading to adjustable friction and damping characteristics. On the other hand, squeeze and elongation mode devices involve vibration absorbers [113, 114], engineering mounts [115], and compressive spring element [116]. The squeeze mode has found applications in areas such as small amplitude vibration and impact dampers. In this

mode, the MR material is subjected to compression, resulting in changes in viscosity and stiffness, which can be utilized for effective vibration and impact damping. In the field-active mode, MREs can change their shape when subjected to a magnetic field. This property, known as magnetostriction, is a result of the movement of magnetized particles along the direction of the magnetic field. MREs working in field-active mode offer several advantages, including larger strain capabilities. These characteristics make them suitable for soft actuators and fast artificial muscles. Recently, Bose *et al.* [117] designed a linear and radial actuator and a controllable valve. Another example of an application utilizing the field-active mode of MREs is a soft actuator design by Kashima *et al.* [118]. Borcea and Bruno *et al.* [119] investigated the magneto-elastic behavior of the MR solid. They stated that isotropic MREs would compress in the direction of magnetic field, whereas anisotropic MREs would expand in that direction.

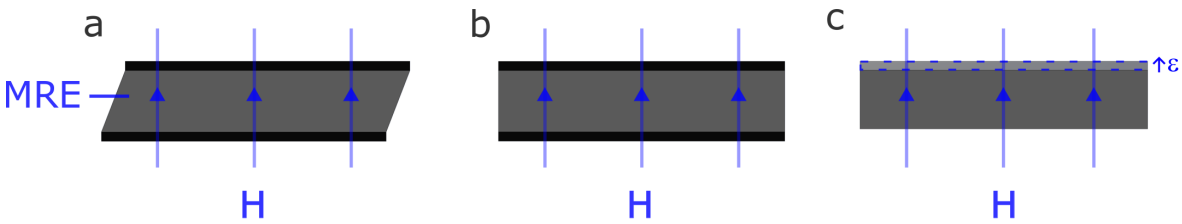

Figure 2.10. Scheme of basic operation modes for MREs: (a) shear mode, (b) squeeze/elongation mode, and (c) field-active mode. H represents the applied magnetic field.

3. MATERIALS AND METHODS

3.1. Cantilever Bending Behavior of MREs

In this section, the bending behavior of MREs is investigated to explain the influence of the volume fraction of magnetic particles on the magnetorheological (MR) effect and the applied magnetic field. Cantilever bending experiments were performed under various external magnetic fields.

3.1.1. Theoretical Background

The volume fraction of the magnetizable particles affects the modulus, E, of MREs, which exhibits a remarkable variation in response to an applied magnetic field. Presenting an analytical model that defines the increase in E is crucial for accurately analyzing the relationship between the applied field and f. Continuum mechanics theories and statistical or kinetic theories, which derive magnetoelastic properties using an energy-based method, are the two main approaches used to explain MREs' magnetoelasticity. We have developed our governing magnetoelastic equations based on a study by Lockette *et al.* [120] that derive the cantilever bending behavior of MREs. Their study used a beam theory model with an elastic strain density. They coupled it with demagnetizing effects in the magnetic energy density to predict the material response to applied magnetic fields. A schematic of the cantilever beam can be seen in Figure 3.1.

The MR effect, which is the difference between no-field modulus and field-induced modulus, can be defined as

$$\Delta E = \frac{E(\mathbf{H}) - E(H=0)}{E(H=0)}, \tag{3.1}$$

where $E(\mathbf{H})$ and $E(H=0)$ are field-induced modulus and no-field modulus, respectively.

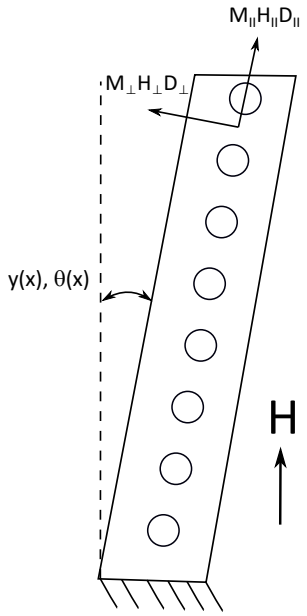

Figure 3.1. Schematic of the beam model developed by Lockette *et al.* [120]. The magnetic field H, magnetization M, and demagnetizing tensor D components are shown in parallel and perpendicular directions. $y(x)$ and $\theta(x)$ are the transverse bending deflection and deflection angle of the beam, respectively.

The resultant force exerted by the produced MRE can be calculated using the superposition principle to derive the cantilever bending behavior of the MRE. The total force consists of magnetic and elastic components

$$P(y, H) = F_E(y) + F_H(y, H), \tag{3.2}$$

where P is the resultant force at the tip, y is the tip displacement, F_E is the elastic force, and F_H is the force due to magnetic interactions.

F_E only depends on y due to the material's inherent elasticity, while F_H depends on displacement and applied magnetic field. When there is no magnetic field ($F_H(y, 0) = 0$), Equation (3.2) yields $P(y, 0) = F_E(y)$, which means there is no magnetic force component at the tip of the MRE sample. This is a valid simplification for soft-magnetic particles, like in our case, since they have zero remnant magnetization, which means the material does not have an inherent magnetic stiffness under zero applied field. Lockette's experimental study also indicates that the resultant force's

elastic and magnetic components show a nearly linear behavior with tip displacement. Therefore, Lockette *et. al.* employed an energy approach to model the beam's elastic and magnetic parts. The total resultant energy per unit length can be found using both magnetic and elastic parts

$$U_T = U_E + U_H, \tag{3.3}$$

where U_E and U_H are the elastic energy per unit length and magnetic energy density of the beam, respectively.

Using Bernoulli-Euler beam theory, elastic energy per unit length of the cantilever beam U_E is given as

$$U_E = (\frac{EI}{2})(\frac{d^2y}{dx^2})^2 - P(\frac{dy}{dx}), \tag{3.4}$$

where E is the modulus of elasticity of MRE in the absence of a magnetic field, and I is the area moment of inertia. Using the linear magnetic energy as in [121]

$$U_H = \mu_0(\frac{1}{2}\mathbf{M}\cdot\mathbf{H}A + \frac{1}{2}\mathbf{MD}\cdot\mathbf{M}A), \tag{3.5}$$

where μ_0 is permeability of the free space, A is the cross sectional area of MRE, $\mathbf{M}$ is the magnetization, and $\mathbf{D}$ is demagnetization tensor. The parallel and normal components of $\mathbf{M}$, $\mathbf{D}$, and $\mathbf{H}$ are shown in Figure 3.1. The parallel and normal components of the magnetization of a composite material can be written as

$$M_{\parallel} = H\bar{\chi}cos\theta \tag{3.6}$$

$$M_{\perp} = \frac{\bar{\chi}}{1+\bar{\chi}}Hsin\theta, \tag{3.7}$$

where $\bar{\chi}$ is the effective magnetic susceptibility of the MRE.

The magnetic energy density can be obtained as follows if we assume a small angle assumption, $dy/dx \sim \theta$

$$U_H = \mu_0\left\{\frac{1}{2}\bar{\chi}H^2\left[1-(\frac{dy}{dx})^2\right] + \frac{1}{2}\frac{\bar{\chi}}{1+\bar{\chi}}(\frac{dy}{dx})^2 + \frac{1}{2}\left[\frac{\bar{\chi}}{1+\bar{\chi}}(\frac{dy}{dx})\right]^2\right\}A. \tag{3.8}$$

Therefore, the total energy per unit length of the beam (U_T) is obtained as

$$U_T = \mu_0 \left\{ \frac{1}{2}\bar{\chi}H^2 \left[1 - (\frac{dy}{dx})^2\right] + \frac{1}{2}\frac{\bar{\chi}}{1+\bar{\chi}}(\frac{dy}{dx})^2 + \frac{1}{2}\left[\frac{\bar{\chi}}{1+\bar{\chi}}(\frac{dy}{dx})\right]^2 \right\} A + (\frac{EI}{2})(\frac{d^2y}{dx^2})^2 - P(\frac{dy}{dx}). \tag{3.9}$$

The governing differential equation is obtained by minimizing U_T, $dU_T/dx = 0$, which yields

$$\frac{d^3y}{dx^3} - \frac{\mu_0 AcH^2}{EI}\frac{dy}{dx} - \frac{P}{EI} = 0, \tag{3.10}$$

where

$$c = \frac{\bar{\chi}^3}{(1+\bar{\chi})^2}. \tag{3.11}$$

Equation (3.10) was reduced by Lockette *et al.* to be able to find the maximum value of y. It is as follows

$$y = \frac{3P}{k}\left[\frac{1}{\psi^2} - \frac{tanh\psi}{\psi^3}\right], \tag{3.12}$$

where

$$\psi = \sqrt{\frac{3k_H}{k_e}} \tag{3.13}$$

$$k_H = \frac{\mu_0 AcH^2}{L}, \tag{3.14}$$

where k_e is the elastic stiffness of the beam, k_H is the field-induced stiffness of the beam, and L is the free length. Using Bernoulli-Euler beam theory, k_e can be found as

$$k_e = \frac{3EI}{L^3}. \tag{3.15}$$

E of composite materials is related to (f) by the viscosity law [122]. The following formula can be used to evaluate E

$$E = E_0(1 + 2.5f + 14.1f^2), \tag{3.16}$$

where E_0 is the matrix modulus. This equation is inadequate for volume fractions higher than 30% [123]. The primary interest is how the rheological behavior of MREs is affected by the volume fraction of filler particles and the applied magnetic field, which Equation (3.1) and Equation (3.16) give us this information. However, this equation needs to be revised for higher volume fractions [123].

3.1.2. Experiments

A stand-alone isotropic MRE module was designed and produced for the proof-of-concept. The module's geometry was selected as a cylinder considering the fact that the stiffening channel of the soft robots is generally cylindrical in shape. The produced module was performed on the cantilever bending experiments. MRE compounds are made of magnetizable particles with sizes ranging from nano to micro and an elastic matrix. Previous studies found that softer elastomeric matrices can provide a better MR effect [124]. We chose our matrix material as polydimethylsiloxane (PDMS) to observe advanced stiffness change in the produced MRE. Non-processed PDMS is an elastic, transparent, and biocompatible material, making it suitable and applicable to minimally invasive surgery (MIS) devices.

3.1.2.1. Sample Preparation. PDMS, Sylgard 184, an elastomer matrix, and carbonyl iron particles with an average size of 5 μm were mixed thoroughly into a homogenous mixture until all ingredients were evenly mixed. The mixture was put into a 3D-printed mold. Air bubbles inside the mixture were removed first, and then the MRE samples were cured for 4 h at 54°C in the vacuum oven (NUVE EV 018). Four different isotropic MRE samples containing 9.09%, 18.18%, 27.27%, and 36.36% volume fraction f were prepared to perform the cantilever bending experiment. The components and consumables to prepare the isotropic MRE test samples are shown in Figure 3.2.

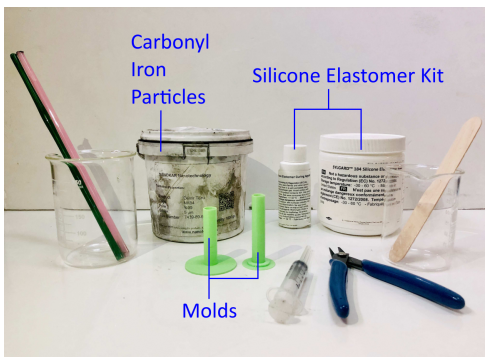

Figure 3.2. MRE material fabrication components and consumables.

3.1.2.2. Cantilever Bending Experiment. Figure 3.3 shows a schematic of the experimental setup. The setup consists of two identical neodymium permanent magnets (N35 grade, with dimensions 50 mm X 50 mm X 10 mm) with an iron back plate. The setup was equipped with a positioning mechanism, with which it is possible to vary the distance between the magnets (d) and, thus, the intensity of the magnetic field crossing the sample. The MRE sample, with a diameter of 10 mm and length of 40 mm, was placed on one of the permanent magnets with the help of a clamp; therefore, it can be considered as a cantilever beam since the proximal end is fixed, and the distal end is free.

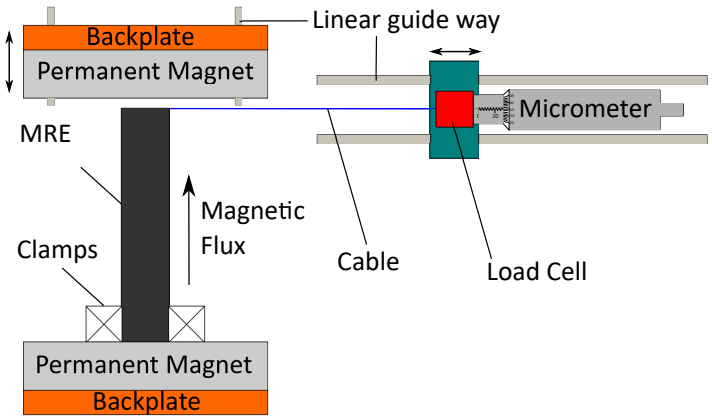

Figure 3.3. Experimental setup for cantilever bending of MRE samples. The micrometer was used to pull a non-extensible cable which is attached to the tip of the MRE sample.

In this experiment, the tip of the MRE sample was deflected incrementally by a micrometer screw gauge with a resolution of 0.01 mm. At the same time, the resulting force (P_E) was measured using a 1-kg miniature load cell. The tests were performed for 16 cases, a combination of each MRE sample and four different magnetic fields. The magnets were removed from the experimental setup to conduct the experiments without an external field. The value d was set to 60 mm, 90 mm, and 120 mm, and a teslameter (PCE-MFM 2400) was used to measure the magnetic field. The results were found to be 32 mT, 64 mT, and 203 mT for distances of 120 mm, 90 mm, and 60 mm, respectively. Force measurements were repeated three times for each test.

3.2. Layer Jamming of MREs

In this work, the unique mechanics of magnetic jamming of MRE layers is investigated as a first step to obtain a hybrid stiffening method combining a jamming-based method with a viscosity-based method for stiffness control of soft robots. The primary motivation to combine magnetic jamming with viscoelasticity modification is to achieve an increase in stiffness variation by triggering both methods with a single source of actuation. The use of MREs in soft robotics is reviewed in [125]. It highlights that MREs are used as a magnetostriction-based actuator, a micro-actuator that rotates when exposed to a magnetic field, a pneumatic valve, a soft inchworm robot for terrestrial locomotion, and a soft skin sensor for localizing deformations. In addition, the article shows an example of a variable stiffness surgical manipulator that utilizes MREs and electromagnets in a soft robot design [126]. Recently, it is presented a magnetically-controlled stiffening mechanism that entails layers, fibers, and granules as scaffolding materials enclosed with a flexible pouch filled with MRF [68]. In this part of the thesis, MREs as layer scaffolding materials are used that avoid the use of MRF and pouch. Thus, we overcome the problems associated with MRF such as leakage or particle settling. However, using MREs in a jamming structure for stiffness variation in soft robots has yet to occur in the literature.

The main focus of this paper is to explore stiffness change both due to jamming and variable viscoelasticity of MRE layers. Although modulus and damping behaviors of MREs in the presence of a magnetic field are well documented in the literature [73, 74, 106], there are very few studies on how surface friction of MRE materials change under an applied magnetic field [90]. Physical interaction of different MRE samples under a magnetic field has never been studied before. Therefore, the effects of jamming and variable viscosity on stiffness change in a stack of MRE layers before a possible soft robot implementation had to be investigated. Actual implementation of the proposed hybrid stiffening method for soft robotic applications is studied in Section 3.3.

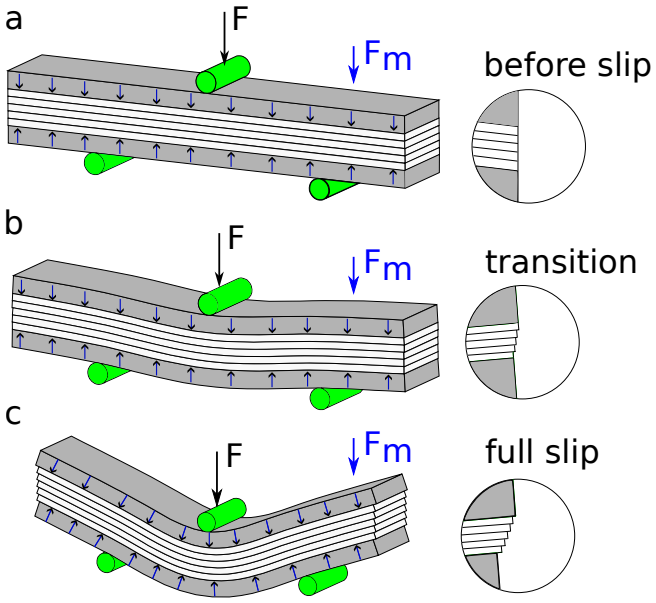

Figure 3.4. Schematic illustration of the three deformation regions within a multi-layer jamming structure. (a) In the pre-slip region, there is no slip at the interfaces between the layers. (b) The partial-slip region, where some interfaces begin to slip, and the bending stiffness gradually decreases. (c) All layers are in a slip in the full-slip region.

A layer-jamming structure consists of compliant MRE layers and two flexible Nd-FeB magnets (see Figure 3.4). MRE layers were stacked between two flexible magnets with the same magnetic polarization. The magnets (grey) jam the MRE layers (white) with magnetic forces (F_m). The magnitude of the applied magnetic force and the layer-to-layer friction coefficient determine the range of these regimes. The magnetized (ON State) and unmagnetized (OFF State) NdFeB magnets were used in three-point bending tests to compare the jammed and unjammed structures' stiffness.

3.2.1. Sample Preparation

The MRE samples were manufactured using PDMS (Sylgard 184, Dow Corning Inc.) as an elastomer matrix, and 5 µm carbonyl iron particles. The matrix material consists of two components: the part (A) and the hardener component (B). These were mixed with the ratio of A:B = 10:1, and 30 % by weight of its thinner. Afterward,

carbonyl iron particles (CIP) was mixed thoroughly into the homogenous mixture until all ingredients were evenly mixed. The mixture was placed into a vacuum chamber for 15 min at -1 bar to ensure proper elimination of air bubbles. Then, the mixture was put into aluminum molds. The curing process was performed at 100 °C for 1 hour without a magnetic field to have isotropic MRE samples. Five different MRE samples containing 0% (pure PDMS) 10%, 20%, 30%, and 40% volume fractions (f) were prepared to perform large strain experiments. The size of the samples used in the tests is 60 mm in length, 10 mm in width, and three different thicknesses: 1 mm, 2.5 mm, and 5 mm.

Flexible magnets were manufactured to provide a magnetic field to the MRE layers. The magnets were made of the same elastomer matrix, PDMS (Sylgard 184, Dow Corning Inc.), and hard magnetic neodymium-iron-boron (NdFeB) microparticles (MQP-S-11-9-20001, Magnequench, Co. Ltd.): both were mixed with a mass ratio of 10:1. The fabrication methods in MRE production were also applied in producing the flexible magnets. The length, width, and thickness of the magnets are 60 mm, 10 mm, and 2.5 mm, respectively. The manufactured MRE samples and flexible magnets are shown in Figure 3.5. The manufactured flexible magnets were subjected to a large uniform magnetic field of 2.1 T using a dipole electromagnet (5403AC, GMW Associates) (see Figure 3.6). Magnetic field measurements were done using a Teslameter (PCE-MFM 2400).

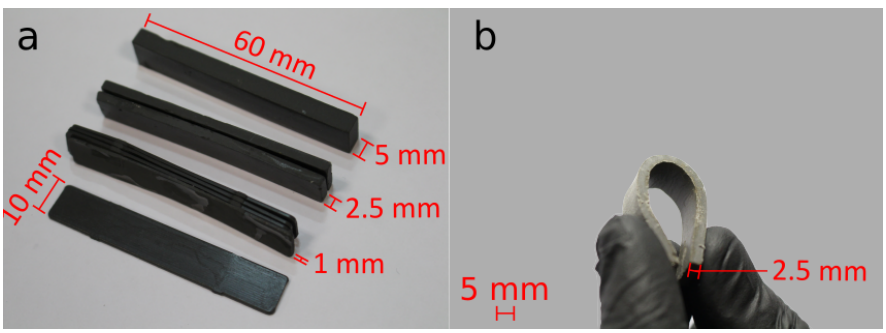

Figure 3.5. (a) The fabricated MRE specimens with three different thicknesses. (b) An image of a flexible NdFeB magnet.

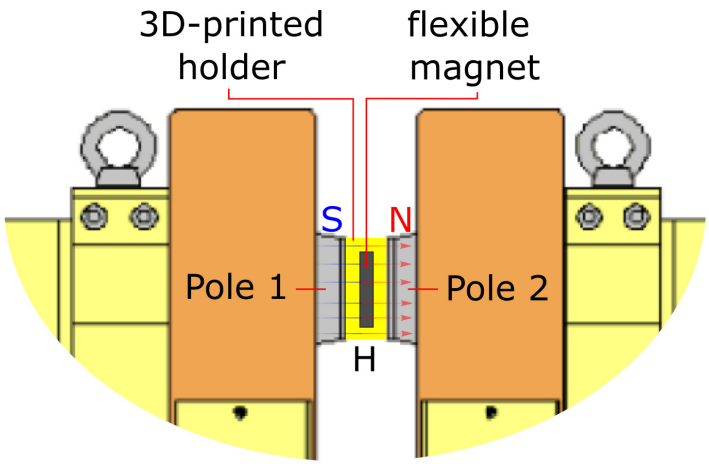

Figure 3.6. Schematic of the magnetization process. A uniform magnetic field is applied through a flexible NdFeB magnet. The magnet and its holder (a non-magnetic 3D-printed part) were placed between the magnetic poles of the electromagnet.

3.2.2. Experiments

There are two types of experiments conducted in this study. First, tensile tests were conducted to characterize the MRE samples. Second, the performance of the jamming structure was evaluated with and without the use of magnetic forces through 3-point bending tests.

3.2.2.1. Tensile Tests. Uniaxial tension tests were performed in the absence of a magnetic field to characterize the mechanical behavior of the MRE samples. The tests were conducted on the 2.5 mm thick MRE samples. The schematic of the experimental setup can be seen in Figure 3.7. The setup has a force measuring unit equipped with a 3-kg miniature load cell, a micrometer screw gauge with a resolution of 0.01 mm, and a stepper motor. In this experiment, the MRE samples were clamped using 3D-printed parts. The samples were tested up to 25 % engineering strain using the stepper motor running at a constant rotational speed corresponding to 0.2 mm/s tension speed. The tension force was measured using the load cell attached to the moving clamp. The tests were displacement controlled.

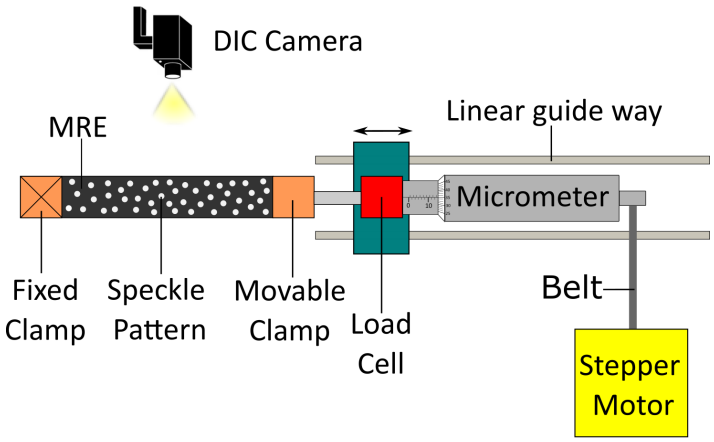

Figure 3.7. Schematic of the experimental setup for uniaxial tensile test. The sample was sprayed with white paint to create a random speckle pattern. The distal end of the MRE samples was fixed, while the proximal end was attached to the load cell.

A Digital Image Correlation (DIC) system was used to measure strains optically with a high-resolution camera (Pike F505B, Allied Vision Technologies). The Mullins effect, a well-known effect in rubber-like materials, is observed in the MREs since they are sensitive to stress softening [106, 127]. To eliminate this effect, a six-cycle test procedure was performed. The first three cycles were used for stress softening, whereas the last three were used to characterize the material. The tests were performed for each MRE sample and the PDMS sample.

3.2.2.2. Friction Tests. The experimental setup used in the tensile tests was adapted to measure the coefficients of friction between both the MRE samples and the NdFeB samples. The schematic of the experimental setup is shown in Figure 3.8. In this experiment, 3D-printed parts were glued to the MRE samples and the NdFeB magnet. One of the 3D-printed parts was fixed to the ground, while the other was attached to the load cell. A known mass M was placed onto the upper 3D-printed part. The material at the top was displaced 10 mm horizontally at a constant speed of 0.1 mm/s while the resulting force was measured. The tests were performed for ten pairs consisting of the MRE samples and NdFeB magnet, and MRE-to-MRE interactions. The number of repetitions for each test is three.

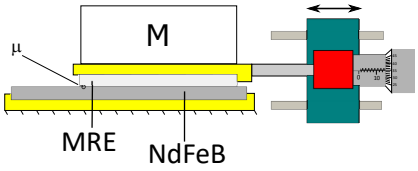

Figure 3.8. Schematic of the friction test setup. Kinetic coefficients of friction μ between MRE-to-MRE and MRE-to-NdFeB are calculated by taking the average of the measured force in the dynamic range.

3.2.2.3. 3-point Bending Test. The three-point bending test was used to evaluate the layer jamming structure (see Figure 3.9). The structure consists of two flexible magnets at the top and bottom and the MRE layers at the core. The magnets attract each other and jam the MRE layers since they are placed so that their pole directions are the same. In the OFF State, non-magnetized flexible magnets were used, while magnetized flexible magnets were used in the ON State. The tests were performed for 30 cases, a combination of five different MRE volume fractions (f) (including PDMS, i.e., f=0), two states (ON State and OFF State), and three different test configurations. The configurations are a single-layer MRE with 5 mm thickness, two MRE layers with 2.5 mm thickness, and five MRE layers with 1 mm thickness. The force measuring unit was placed vertically down to measure forces. The number of repetitions for each test is five. The samples were preconditioned by bending a few times with bare hands before each test to mitigate the Mullins effect.

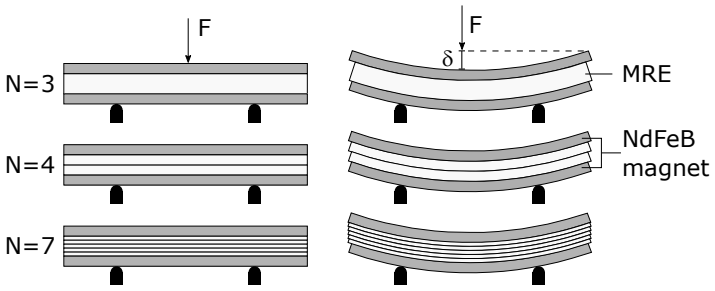

Figure 3.9. Schematic of 3-point bending test. N stands for the number of layers in the jamming structure. The MRE layers (white) and the flexible magnets (grey) are deflected while the resultant force is measured. The thickness of the overall jamming structure is 10mm, and the deflection (δ) is 5 mm.

3.2.3. Finite Element Analysis

Finite element analyses were performed for three purposes: material characterization, magnetic simulations, and multilayer jamming simulations. First, a finite element model was developed to validate our tensile test data with DIC measurements. The simulations were performed using the Static Structural module of ANSYS to characterize the PDMS sample and the MRE samples with 10, 20, 30, 40 % volume fractions (f) and the flexible NdFeB magnet. The materials were modeled in 3D and stretched up to 25% engineering strain, as in the experiments. Curve-fitting was performed on the experimental data using a hyperelastic model.

Second, magnetic simulations were performed on a three-layer jamming structure model using the Magnetostatic module of ANSYS in 3D. The model consists of two flexible magnets, an MRE material at the core, and an air domain. The geometry of an overall model is shown in Figure 3.10. The thickness of the MRE is 5 mm, and the size of the magnets is 60 mm in length, 10 mm in width, and 2.5 mm in thickness. The magnetic properties of the NdFeB magnet were obtained directly from the manufacturer. They were calculated based on an estimation using the volumetric loading magnetic powder. The retentivity and coercivity values were set to 447 mT and 296 kA/m (H_c), respectively. Magnetic parameters such as MRE permeability with 10, 20, 30, 40 % (f) are retrieved from [106]. The values are 1.6, 2.2, 3.7, and 6, respectively. Schubert [106] measured the magnetic flux density of the MRE samples at multiple locations across the specimen to determine the permeability of MREs. Cylindrical samples containing varying quantities of iron particles were positioned on the cradle between the magnets. Subsequently, the magnetic flux was quantified using a Gaussmeter. In addition, the permeability of PDMS is assumed to be 1. The magnetic simulations were performed for 20 cases, a combination of five different MRE volume fractions (f), and four different deflections. The deflections are 0 mm, 2.5 mm, 4 mm, and 5 mm. The average magnetic forces produced from the top and the bottom magnets were obtained. These values were interpolated for the entire deflection range.

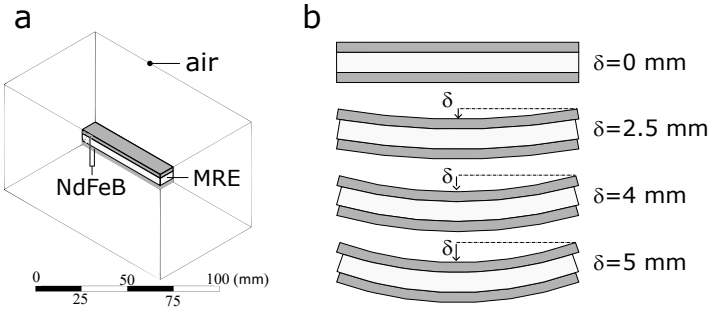

Figure 3.10. (a) 3D FEM of the three-layer jamming structure for magnetic simulation. An MRE layer with 5 mm thickness was placed between two NdFeB magnets, and the structure was surrounded by air. (b) Front view of the model. The simulations were performed for four different cases. For each case, a cylindrical coordinate frame was assigned to determine the polarization direction of the magnets.

Third, finite element simulations were conducted in 2D to predict the mechanical behavior of the N-layer jamming structure. The model consists of two NdFeB layers, N-2 MRE layers, and three rollers (see Figure 3.11). The layers and the supports were modeled with 2D plane-stress elements with material properties, dimensions, and boundary conditions the same as in the experiments.

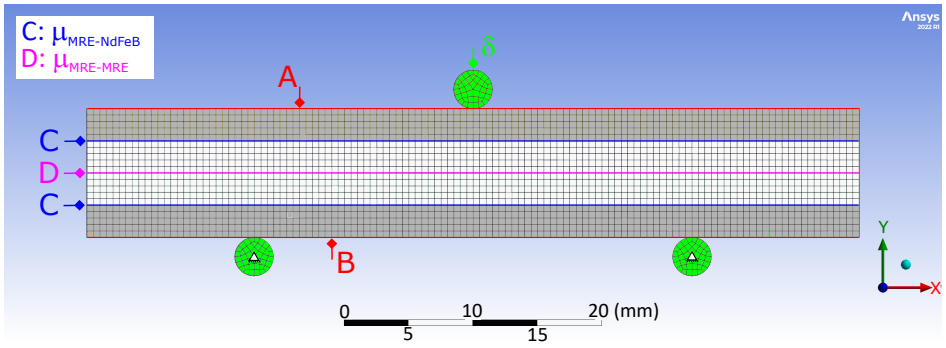

Figure 3.11. Finite element model for N-layer jamming structure. The top roller was displaced 5 mm in -y direction. The bottom rollers were fixed. The magnetic force density values obtained from magnetic simulations were applied to surfaces A, and B. Frictional contact type was used in all interfaces. The surfaces C and D were defined as contact surfaces for the MRE-to-NdFeB and MRE-to-MRE interfaces, respectively.

The interaction between two adjacent MRE layers and the interaction between NdFeB-MRE layers were modeled using the contact elements with a constant coefficient of friction values stated in Table 4.4. The magnetic force values obtained from magnetic simulations were applied to the structures' top and bottom surfaces. The top layer was deflected 5 mm incrementally while the resulting force was measured. Large deflection and quasi-static solutions were enabled in the simulations.

3.3. Fiber Jamming of MREs

Change in stiffness in layer jamming structures is valid only in one direction. On the other hand, fiber jamming structures are effective in soft robotic applications because variable bending stiffness in more than one direction is achieved [54]. In this section, we investigate the unique mechanics of magnetic jamming of MRE fibers to obtain a hybrid stiffening method combining a jamming-based method with a viscosity-based method for stiffness control of soft robots. The STIFF-FLOP surgical manipulator, described in Section 2.2, was selected as an intended application.

3.3.1. Design of the Fiber Jamming Structure

This section describes the combination of the MRE-based and fiber-jamming stiffening methods to obtain a fiber jamming structure. The structure is merged with the STIFF-FLOP manipulator. The fiber jamming structure-integrated STIFF-FLOP manipulator is shown in Figure 3.12. The manipulator consists of three equally-spaced fluidic chambers embedded in an elastomer matrix and a fiber jamming structure at the central channel. The fiber jamming structure has a length of 50 mm and a diameter of 6.5 mm. It consists of MRE fibers covered with a flexible NdFeB magnet. The magnet is used to jam the MRE fibers. The thickness of the magnet is 1 mm. To compare the stiffness of jammed and unjammed fiber structures, magnetized (ON state) and unmagnetized (OFF state) NdFeB magnets were utilized.

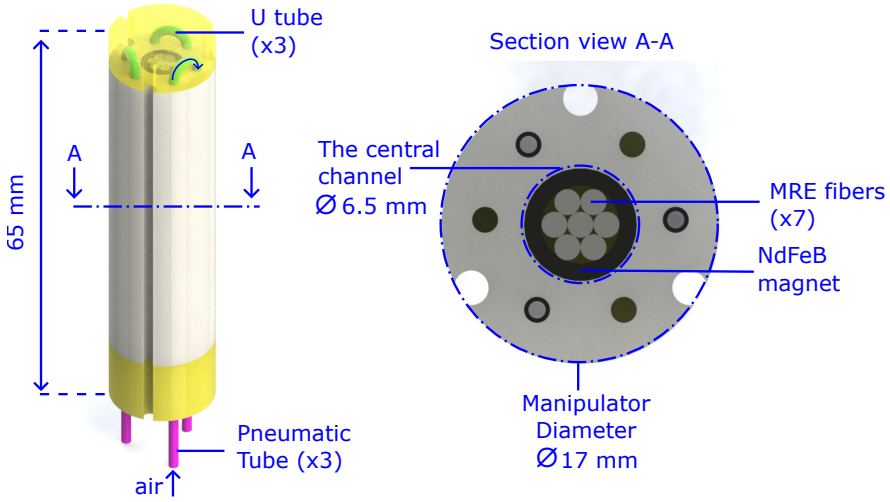

Figure 3.12. CAD drawing of the STIFF-FLOP soft manipulator with an integrated variable stiffness device. The stiffening device is inserted in the central channel of the STIFF-FLOP manipulator. The manipulator's length and diameter are 60 mm and 17 mm, respectively.

There are two different fiber jamming structures inserted in the central channel. First, a fiber jamming structure consisting of a single piece of MRE enclosed by a flexible NdFeB magnet was designed. The design was placed in the stiffening chamber to analyze the stiffness gain due to the MR effect. Second, another structure was designed utilizing the principle of optimal packing congruent pieces based on [128]. In this article, they presented the best packing densities of the circles in a circle. Due to the manufacturing constraints, the number of fibers used in the structure was selected to seven. The MRE fibers are illustrated in Figure 3.13. The fibers are enclosed by a flexible NdFeB magnet, in which magnetic polarization is in the radial direction. The diameter of the single piece of MRE and the seven fibers are 4.5 mm and 1.5 mm, respectively. Polyvinyl chloride (PVC) tubes with an inner diameter of 1.5 mm and an outer diameter of 2 mm are used for inflating the fluidic chambers. They are connected to the chambers in the fabrication process of the modules. The manipulator's overall length is determined by the length of the module (50 mm), the base (10 mm), and the tip (5 mm).

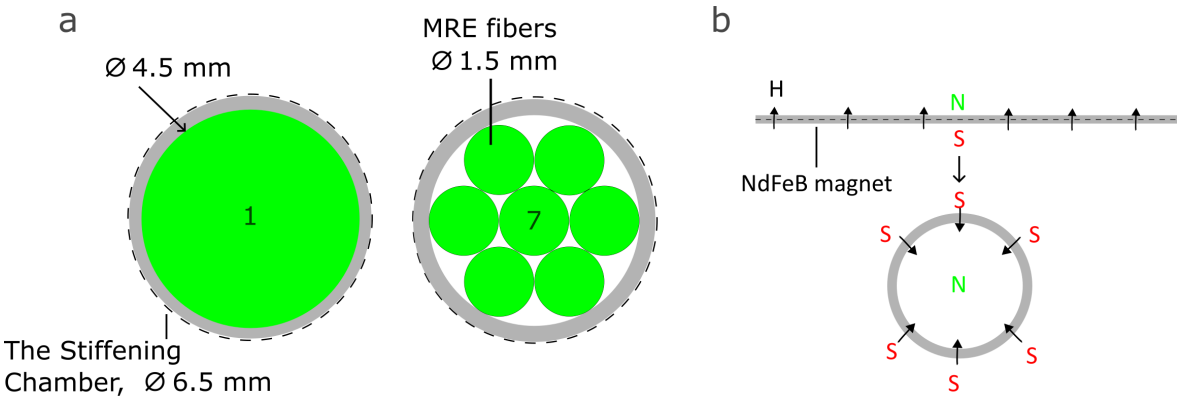

Figure 3.13. (a) A schematic of the packed MRE fibers and a NdFeB magnet in the stiffening chamber. (b) Magnetic polarization of the NdFeB magnet.

The MRE-based and the fiber jamming-based stiffening system is combined with flexible fluidic actuation. The actuation chambers are inflated to achieve omnidirectional bending and elongation of the silicone module. When one chamber is activated, the cylinder bends in one direction; when two chambers are activated at the same pressure, the cylinder bends in the plane between the two chambers; and when all of the chambers are activated at the same pressure, the cylinder elongates along its central axis. An overview of the chamber activation is showcased in Figure 3.14.

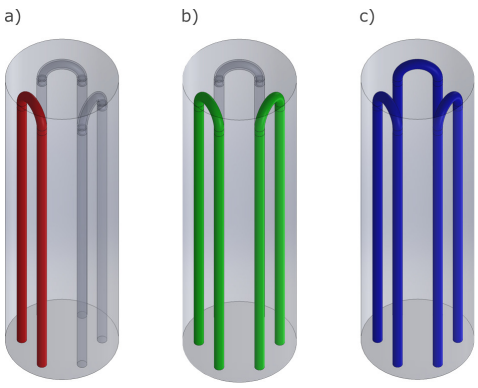

Figure 3.14. Scheme of the module highlighting the fluidic chamber activation. The module bends in (a) and (b) and elongates in (c).

3.3.2. Soft Robot Fabrication

The single-module STIFF-FLOP manipulator with the fiber jamming structure has several silicone molding steps. The fabrication process of the manipulator can be seen in Figure 3.15. First, the chamber molds are threaded with an inextensible polyester thread around a 3D-printed cylinder. The cylinder is made up of three parts: an inner core and two side parts. Six molds are placed in a module mold Figure 3.15a. In this way, the radial expansion of the chamber is prevented. The mold is filled with uncured silicone (EcoFlex 0050, SmoothOn) and left to cure at room temperature. The chamber molds are removed after the silicone has completely cured, beginning with the core and then sliding out the other two side parts. This disassembly of the chamber molds allows them to be loosened within the cured body, allowing easier removal while keeping the thread in place. Second, another layer of silicone is applied to the inside of the chambers to integrate the thread within the body. In order to complete the second layer process, the thin rods (core) with a diameter of 1.5 mm are inserted into the chamber. The second curing step is thus performed by pouring the same uncured silicone into the remaining free space of the side parts Figure 3.15b. Third, the fiber jamming structure composed of MRE fibers covered with a flexible NdFeB magnet was inserted into the stiffening chamber of the STIFF-FLOP manipulator Figure 3.15c. The MRE fibers and the flexible NdFeB magnets were manufactured using the manufacturing technique mentioned in Section 3.2.1. Finally, the main body of the manipulator is sealed at the top and bottom caps with hard silicone (DragonSkin 30, Smooth-On). Three actuation pipes are fixed to the bottom of the module. On the other hand, the U-shaped internal pipes are fixed to the top of the module Figure 3.15c. They are used to connect the double chambers. Figure 3.15d shows the manufactured soft robot. The molds used in the fabrication were disposable and manufactured using a 3D printer (ENDER 3-Pro). Twelve modules were manufactured to perform stiffening tests. There are four cases: a combination of two states (i.e., ON and OFF States) and two different numbers of fibers in the stiffening chamber. Three modules were fabricated for each case to show the module's reproducibility.

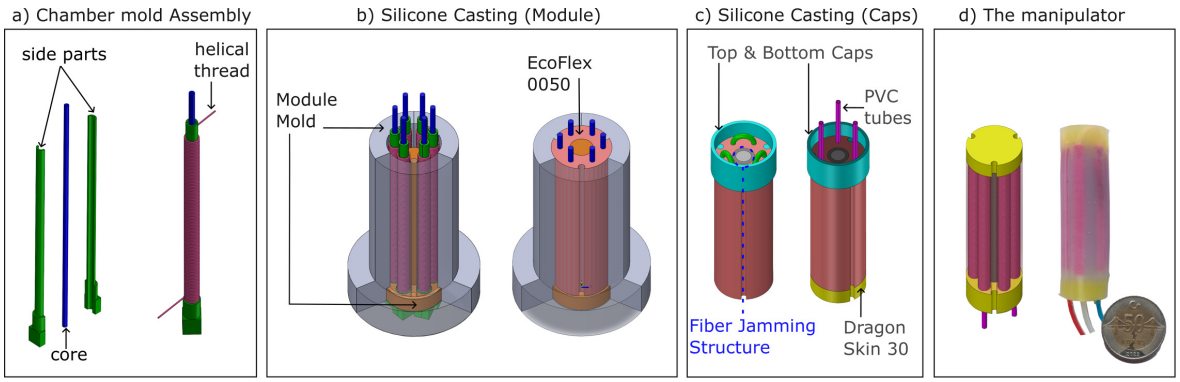

Figure 3.15. Fabrication of the single module STIFF-FLOP manipulator with the proposed MRE fibers and NdFeB magnet. (a) The 3D-printed side parts and a core are assembled, then polyester is winded around the mold. (b) The silicone casting of the body of the module. (c) Fiber jamming structure are inserted, then the top and bottom ends are sealed to the body. (d) The manipulator is fabricated.

3.3.3. Experiments

This section is dedicated to the characterization of the STIFF-FLOP manipulator that is integrated with the proposed MRE fibers. Experimental tests with and without the flexible NdFeB magnet were conducted to assess the manipulator's dexterity and stiffening capacity under a magnetic field.

3.3.3.1. Performance Tests. Fluidic chambers were actuated individually, in pairs, and all simultaneously to characterize the bending and elongation performances of the STIFF-FLOP module. Pressures ranging from 0 to 0.9 bar were imposed in the case of single fluidic chamber activation. In order to calculate the bending angle, a video of the module under continuously increasing pressure was recorded at the front view and elaborated in vector graphics software, Inkscape. An algorithm was used to analyze the captured images with a step of 0.1 bar and determine the bending angle from the curvature of the module. An imaginary line was drawn on the tip of the module, then the angle between the imaginary line and the horizontal determined the bending angle. The same process was used to activate two chambers under the same pressure

simultaneously. The activation of three fluidic chambers results in elongation, and the length variation was measured using the same pressures as for the bending tests. The same algorithm was used to evaluate the elongation, which considers the module's length at each step. The tests were repeated three times for the modules consisting of a single piece of MRE and seven MRE fibers.

3.3.3.2. Stiffening Tests. The stiffening of the fiber jamming structure is changed using the principle of magnetic jamming force induced by flexible NdFeB magnets. The tests were performed in two different configurations, magnetic (ON State) and unmagnetized (OFF State) NdFeB magnets. Stiffening tests were performed in two deformation modes. First, the tip of the fiber jamming-integrated STIFF-FLOP module was deflected 10 mm to measure the change in stiffness using the force-measuring unit described in Section 3.2.2. The structure was tested in the base condition, where no actuation exists in the fluidic chambers. Second, the fiber jamming structure was compressed 5 mm in the longitudinal direction. The number of repetitions for each test is five. In addition, three different structures were tested for each type of experiment. Hence, the number of experiments is 60.

Figure 3.16 reports the component layout for the motion. Pressurized air obtained from the compressor goes into the air regulator to decrease the pressure to around 3 bar. The pressure line is divided into three separate lines, each for an air channel of the module. An inlet valve and an exhaust valve are used to control the air pressure of each channel. The pressure sensor monitors the pressure of the channels. A bang-bang controller is utilized to control the pressure of channels. An Arduino Mega 2560 is used for data acquisition, and the same board is used for control relay modules for turning on and off solenoid valves. A 1-liter air tank is used to eliminate sudden spikes in the pressure of each channel.

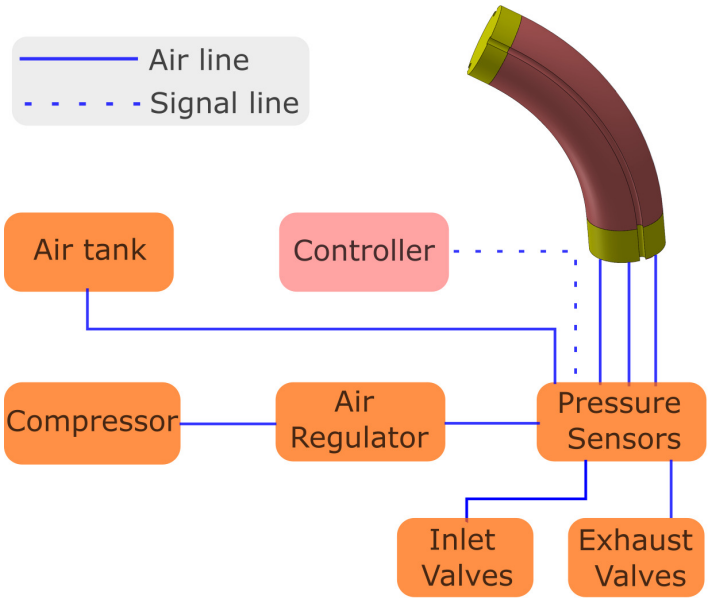

Figure 3.16. A scheme of the components used in the activation of the STIFF-FLOP manipulator.

3.4. Implementation of Electronically-controlled Magnetic Jamming

This section is dedicated to developing a novel variable stiffness device that utilizes MRE fibers and electropermanent magnets (EPMs) in a soft robot design. In Section 3.3, we have achieved stiffness change both due to jamming and variable viscoelasticity of MRE fibers when fiber jamming structure is implemented to the STIFF-FLOP surgical manipulator. Although we proved stiffness gain with this hybrid stiffening method (combining a jamming-based and a viscosity-based method) for stiffening of soft robots, the proposed mechanism in its present form cannot be used in soft robots. It is because the jamming transition is not controlled. This section proposes a novel variable stiffness device based on MRE fibers and EPMs. EPM devices are used to jam the MRE fibers. EPM is a solid-state device whose external magnetic flux can be stably switched on and off by a discrete electrical pulse. The operation principle of an EPM is described here with the theoretical background. The stiffening device, consisting of MRE fibers and EPMs in a compact manner, has been designed, manufactured, and implemented into the STIFF-FLOP manipulator.

3.4.1. Electropermanent Magnets

The magnets can be classified into two main categories depending on the source of magnetism: permanent magnets and electromagnets. Permanent magnets are made from magnetized materials and create their own persistent magnetic field. They can be found in nature, such as lodestone, or made industrially. The artificial permanent magnets are mostly made from the elements iron, nickel, and cobalt and their alloys. Permanent magnets retain magnetic properties until the temperature exceeds the Curie temperature of the magnet material. Electromagnets consist of a coil of wire wrapped around a core made from soft magnetic material. When the current flows through the coil, the core is magnetized and behaves like a magnet. The field disappears when the current is turned off.

Electropermanent magnet, on the other hand, is a hybrid type magnet, a combination of a permanent magnet and an electromagnet. An EPM is a solid-state device whose magnetic flux can be switched between the ON and OFF states due to a discrete electrical pulse. This makes an EPM a more desirable device since the energy is consumed only during the switching between the states, and the transition can be controlled electronically. McDonald *et al.* [129] manipulated the material characteristics of MRFs by utilizing EPMs, enabling regulate the pressure within soft actuators. Recently, Gaeta *et al.* [68] demonstrated the capability of EPMs to control stiffness electronically.

3.4.1.1. Working Principle of EPMs. An EPM consists of two permanent magnets (a hard and a soft magnet), metal caps, and a coil. The target surface and the caps are separated by an air gap, which is denoted as g. The soft and hard magnets have almost the same remanent magnetization; however, they have different coercivity values. The hard magnet has a very high coercivity, whereas the coercivity value of the soft magnet is relatively low. The magnets have the same length (L_m) and diameter (d_m). The caps and coil are made from iron and copper, respectively. The working principle of an EPM device in operation can be seen in Figure 3.17.

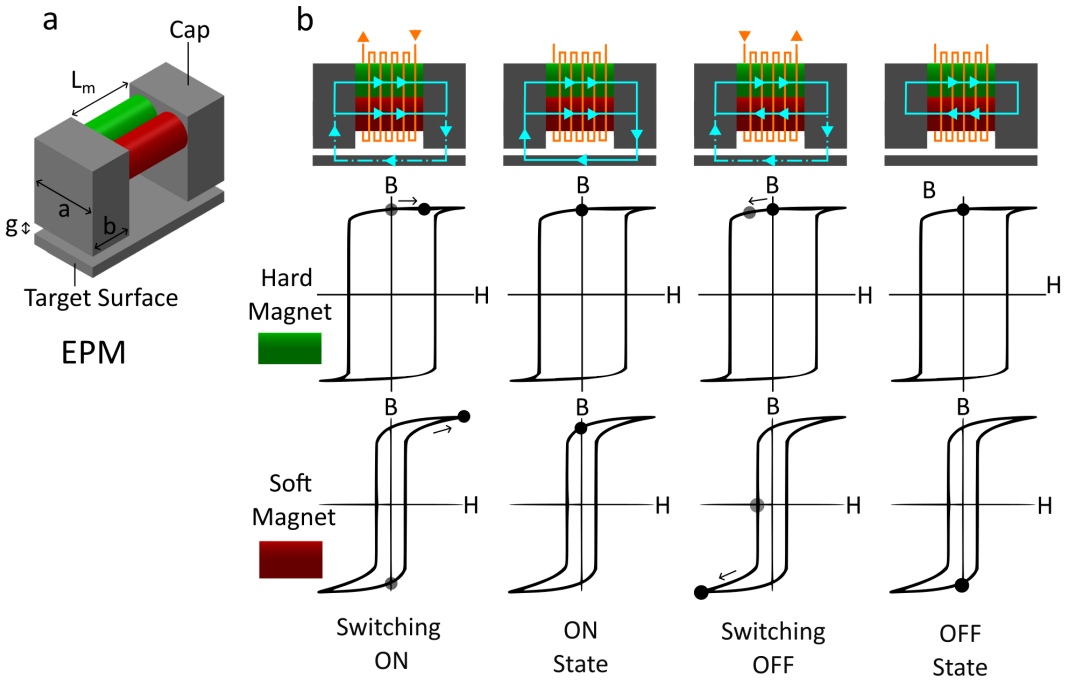

Figure 3.17. The operation principle of the EPM device (a) An EPM device. (b) The operation states and corresponding B-H curves of the soft and the hard magnets. Adapted from [130].

The direction of the current and magnetic flux in the EPM device are illustrated as orange and cyan arrows, respectively. The switching current flows through the coil, and the soft magnet is magnetized up to a saturation point. A part of the flux flows through the target surface (illustrated by cyan dotted lines), however, the majority of the flux device goes through the EPM device. When the soft magnet is fully saturated, the switching current is turned off, i.e., magnetic field intensity is reduced to zero. However, magnetic flux density is equal to the remanent magnetism. The remanence (i.e., retentivity) value is almost the same for the hard and soft magnet in the ON state. When switching to the OFF state, the current is turned on in the opposite direction. The soft magnet is demagnetized up to the point of full saturation but this time in the third quadrant of the B-H curve. The polarity of the soft magnet is changed. When the soft magnet reaches full saturation, the switching current is turned off again. The magnetic flux density is equal to negative remanent magnetism. In the OFF state, magnetic flux flows only through the magnets.

3.4.1.2. Theoretical Background. This section describes the magnitude of the holding force of the EPM using a magnetic circuit approach. The equations are retrieved from [130]. The axial magnetic field intensity within the magnets and the magnetic field intensity in the air gap are denoted as H_m and H_g, respectively. The coil carries a current I_m, and has N_m turns. Consider a loop passing through the magnets, the air gaps, and the keeper bar, Ampere's law states

$$H_m L_m + 2H_g g = N_m I_m. \tag{3.17}$$

Using Gauss's law for magnetic fields and a magnetic circuit approach, the flux conservation can be expressed as

$$\frac{\pi}{8} d_m^2 N_{rods}(B_{AlNiCo} + B_{NdFeB}) = B_g ab + \Phi_{leak}, \tag{3.18}$$

where B_g is the magnetic flux density in the air gap, Φ_{leak} is the pole-to-pole leakage flux, N_{rods} is the number of the magnets used in the EPM device, a is the width of the keeper bars, b is the thickness of the keeper bars, and B_{AlNiCo} and B_{NdFeB} are the axial magnetic flux density in the soft and hard magnet, respectively. It can be used as a straight-line demagnetization curve [131] for the NdFeB magnet

$$B_{NdFeB} = B_r + \mu_0 H_m, \tag{3.19}$$

where μ_0 is the permeability of free space. It is possible to write axial magnetic flux density in the air gap as

$$B_g = \mu_0 H_g. \tag{3.20}$$

It is difficult to calculate the pole-to-pole leakage flux Φ_{leak}, however, it can be estimated based on the leakage coefficient as

$$\Phi_{leak} = (N_m I_m - H_m L_m)\mathbb{P}_{leak}, \tag{3.21}$$

where $\mathbb{P}_{leak}$ is the leakage permeance. The AlNiCo magnet has a nonlinear B-H curve. It is dependent on $H_m(t)$ and time t due to hysteresis. Equation (3.18) can be solved numerically for $H_m(t)$ in terms of $I_m(t)$, and the other parameters

$$\begin{aligned} \frac{\pi}{8} d_m^2 N_{rods}(B_{AlNiCo}(H_m(t), t) + B_r + \mu_0 H_m(t)) = \\ (\frac{\mu_0 ab}{2g} + \mathbb{P}_{leak})(N_m I_m(t) - H_m(t) L_m). \end{aligned} \tag{3.22}$$

Considering the fact that the main flux is perpendicular to the surface of the keeper bars, neglecting leakage terms, the force per area term is given by the T, the normal component of the Maxwell stress tensor is

$$\frac{F}{2ab} = T = \frac{B_g^2}{2\mu_0}. \tag{3.23}$$

The force is obtained if we combine Equation (3.18) and Equation (3.20) by given $H_m(t)$ from the numerical solution of Equation (3.22)

$$F = \mu_0 \frac{ab}{4} \left(\frac{N_m I_m(t) - H_m(t) L_m}{g} \right)^2. \tag{3.24}$$

Note that B_{AlNiCo} and B_{NdFeB} are equal to B_r when the magnets are fully magnetized. In addition, it is assumed that Φ_{leak} becomes zero as g goes to zero. In this case, Equation (3.18) can be expressed as

$$B_g = B_r \frac{\pi d_m^2 N_{rods}}{4ab}. \tag{3.25}$$

Hence, the holding force can be expressed as

$$F = \frac{1}{\mu_0 ab} \left(\frac{\pi B_r d_m^2 N_{rods}}{4} \right)^2. \tag{3.26}$$

It can be inferred from Equation (3.26) that as the pole area ab is decreased, the force increases with the other terms held constant. In order to maximize the force, the pole area is set so that the air gap flux density is just below the saturation flux density of the pole pieces, B_{sat}. The optimal value of the dimension b is expressed as

$$b = \frac{B_r}{B_{sat}} \frac{\pi d_m^2 N_{rods}}{4a}. \tag{3.27}$$

The holding force is obtained as

$$F = \frac{B_{sat}^2 ab}{\mu_0}. \tag{3.28}$$

3.4.1.3. Design of the EPM Device. An EPM device was designed and developed to jam the MRE fibers inserted into the central channel of the variable stiffness device. The EPM device can be seen in Figure 3.18. The device is composed of a hard magnet (N42 Grade, NdFeB) and a soft magnet (AlNiCo 5), two steel caps, and a copper wire coil (AWG 40). The pair N42 grade NdFeB and AlNiCo 5 magnets are selected since they have very similar remnant magnetization (B_r=1.28 T) and different coercivities (AlNiCo=51 kA/m, NdFeB=943 kA/m).

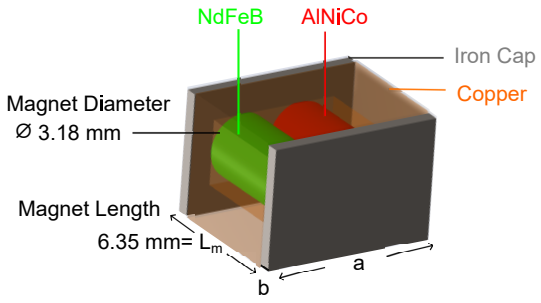

Figure 3.18. CAD model of the EPM device.

3.4.1.4. Magnetic Simulations. This section is dedicated to the simulation of the EPM device. A 3D model has been constructed using a Magnetostatic solver of ANSYS Maxwell. The model consists of two hexagonal-shaped MREs (at the top and the bottom), seven MRE fibers at the center, and six EPM devices, three on the proximal and three on the distal end. The EPM devices are equally spaced in a radial arrangement. The overall model can be seen in Figure 3.19. The EPM device used for simulation has been modeled according to the specifications described in Section 3.4.1.3. The pole directions of the magnets were adjusted as shown in the model. The pole directions of the magnet pairs differ by 60 degrees from each other. The surrounding vacuum domain is modeled as a rectangular prism with a 150 % offset in -x, -y, and -z directions.

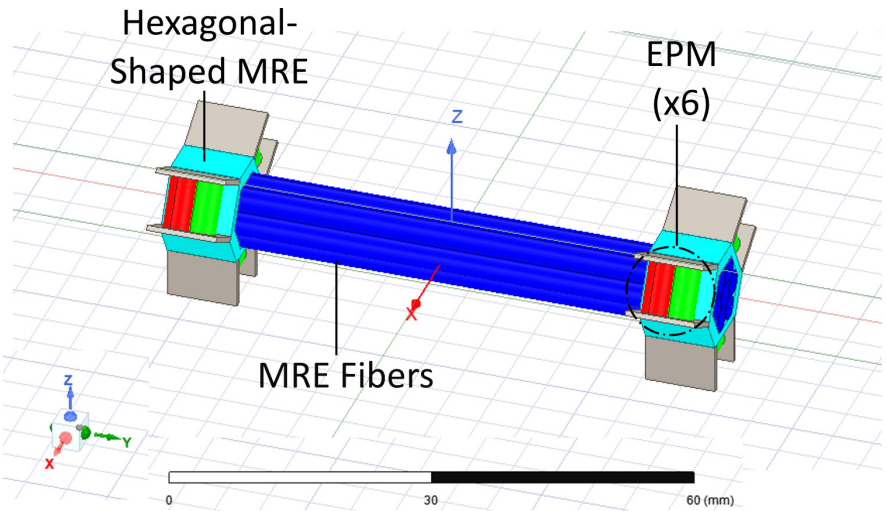

Figure 3.19. 3D model showing the MRE fibers, the hexagonal-shaped MRE, and the EPMs.

Table 3.1. The parameters of the EPM device used in the simulation.

Parameter	**Symbol**	**Value**	**Units**
Magnet diameter	d_m	3.18	mm
Magnet length	L_m	6.35	mm
Cap length	a	8.5	mm
Cap width	b	0.6	mm
Remnant Magnetization	B_r	1.28	T
Coercivity of AlNiCo	H_m	51	kA/m
MRE permeability	f	3.7	N/A

Three different simulations were performed here. First, the $N_m I_m$ value, i.e., ampere-turn to change the polarity of the AlNiCo magnet, was simulated using only the EPM model. Second, the amount of jamming force obtained from an EPM device was simulated using hexagonal-shaped MREs, MRE fibers, and the EPM. Finally, the simulation was performed to calculate the magnetic flux density passing through the MRE fibers. The overall model presented was used for the simulation.

The material properties and the dimensions of the EPM device and MRE fibers for the simulation are shown in Table 3.1. N42 grade NdFeB magnet and AlNiCo 5 magnet are used in the simulation. The diameter and length of the magnets are 3.175 mm and 6.35 mm, respectively. The magnets are enclosed with the copper region. The cross-section area of the region is $L_m w$, where w is the height of the coil. In the simulation, w is taken as 1 mm. Based on Schubert's thesis [106], the permeability value for the isotropic MRE when f=0.3 is selected as 3.7.

3.4.2. The Variable Stiffness Device

3.4.2.1. Design of the Stiffening Device. This section describes the design of a variable stiffness device. The device is integrated into the STIFF-FLOP surgical manipulator. The stiffening device and device-integrated STIFF-FLOP manipulator are shown in

Figure 3.20. The stiffening device consists of six EPMs, two hexagonal MRE pieces, and axially packed seven MRE fibers. The EPMs are located in the base and tip regions. They are used to jam the fibers and provide magnetic fields. The stiffening device has a length of 60 mm. The hexagonal-shaped MRE pieces are placed between the EPMs and MRE fibers to provide magnetic forces.

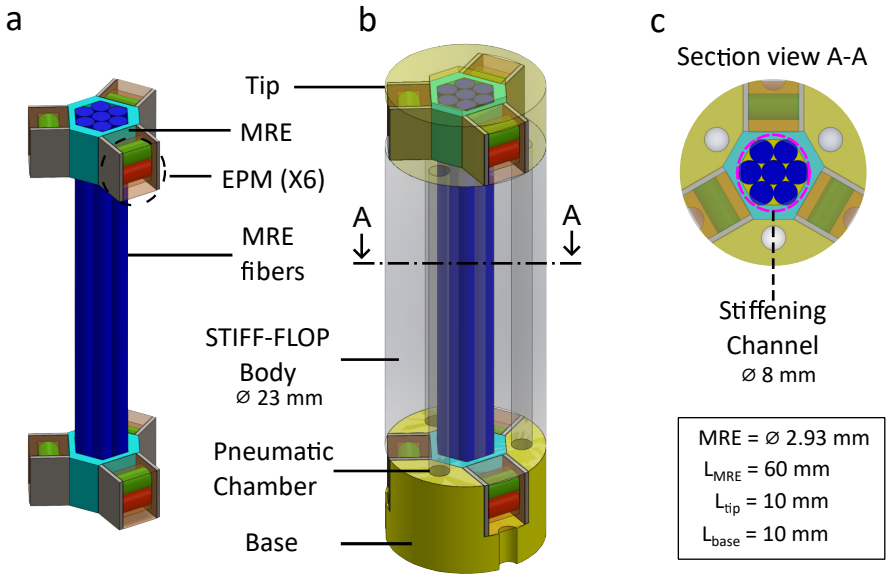

Figure 3.20. CAD drawing of the proposed stiffening device and its implementation to the STIFF-FLOP manipulator. (a) The stiffening device, (b) the device-integrated STIFF-FLOP manipulator, (c) and its cross-section view.

The stiffening device-integrated STIFF-FLOP manipulator is made up of a cylindrical shaped elastomer, including a main body, a base, and a tip. The main body consists of three equally-spaced fluidic chambers and a stiffening chamber at the center. The manipulator has a length of 80 mm and a diameter of 23 mm. The stiffening device has six EMPs. They are located at the base and tip of the manipulator as shown in Figure 3.20. A stiffer material (DragonSkin 30) is used in these regions since the EPMs are embedded here. The number of MRE fibers packed into the stiffening chamber is seven. Since the diameter of the stiffening chamber of the STIFF-FLOP is 8 mm, the diameter of the MRE fibers is 2.93 mm. With this device, it is possible to obtain various stiffening states. In the softest state, the six EPMs are in the OFF state, whereas the rigid state is obtained when the EPMs are switched to the ON state.

Different stiffness states can be obtained between the maximum and minimum values depending on the number of activated EPMs and the configuration.

3.4.2.2. Fabrication of the Stiffening Device. The isotropic MRE fibers containing 30% volume fraction (f) were manufactured using the manufacturing method mentioned in Section 3.2.1. The length and diameter of the MRE samples are 60 mm and 2.93 mm, respectively. The molds were made of PLA material, a non-magnetic material. The curing process was performed at 45 degrees for six hours.

The EPM device is composed of a NdFeB magnet, an AlNiCo magnet, two steel caps, and a copper wire. The N42 grade NdFeB magnets and the AlNiCo 5 magnets were purchased from KJ Magnetic, Inc and McMaster-Carr, respectively. The diameter and the length of the magnets are 3.18 mm and 6.35 mm, respectively. The magnets are glued to the caps using an epoxy adhesive and wrapped with a coil of 80 turns of 40 AWG copper wire. The dimension of the pole pieces is described in Section 3.4.1.4. The manufactured of the MRE fibers and EPM device is shown in Figure 3.21.

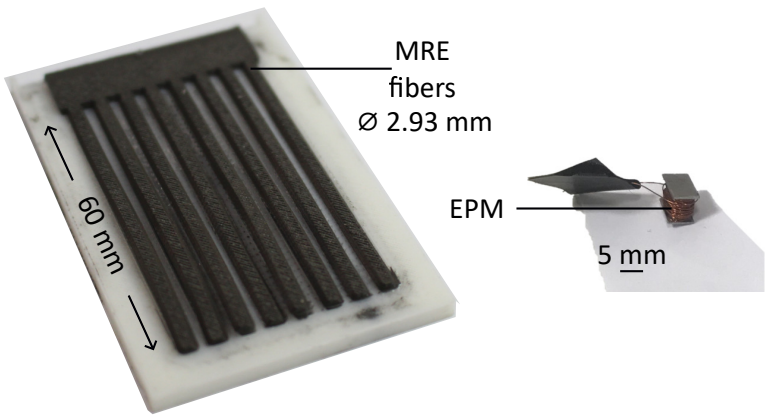

Figure 3.21. (a) The manufactured MRE fibers, (b) and the EPM device.

The manufacturing steps mentioned in Section 3.15 were mainly followed for the variable stiffness device-integrated STIFF-FLOP manipulator. In addition to mentioned fabrication steps, the EPM devices were placed in the corresponding positions at the final stage. The stiffening tests were performed when the EPMs were ON and

OFF states. Each condition was repeated three times. The manufactured manipulator can be seen in Figure 3.22.

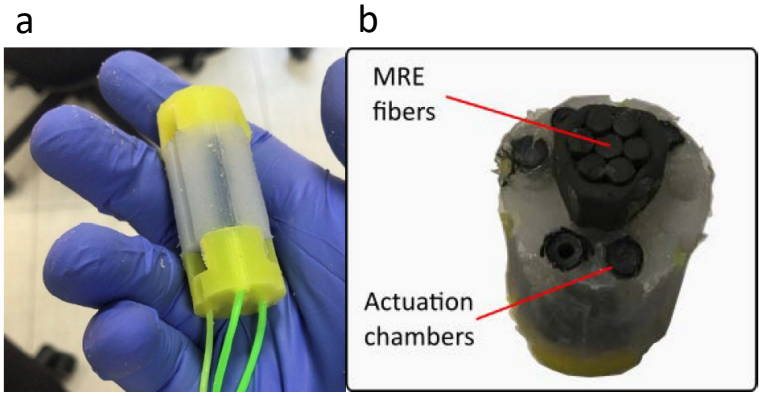

Figure 3.22. The manufactured STIFF-FLOP manipulator. (a) The assembled module without the EPM devices. (b) A cut-view of the manipulator. MRE fibers are placed into a stiffening chamber.

4. RESULTS AND DISCUSSION

This section covers the results of the cantilever bending tests of the MRE samples, the experimental and finite element results of the multi-layer jamming structures, magnetic fiber jamming results, and the results of the electronically-controlled EPM integrated-STIFF-FLOP manipulator.

4.1. Cantilever Bending Results

The results of the cantilever bending of MREs are presented here. The stiffening performance of the MRE samples was examined. The results of the cantilever bending experiments were compared to the analytical model developed by Lockette *et al.* [120] and the analytical model I have developed mentioned in Section 3.1.1.

The results of the cantilever bending experiment and theoretical model developed by Lockette *et al.* are shown in Figure 4.1. The results indicate that the resultant force at the tip shows a nearly linear behavior ($R^2 \geq 0.9943$) with tip displacement for each case.

Slopes of the force vs. displacement curves give stiffness values of the MRE samples. It can be inferred from the subfigures of Figure 4.1 that MRE stiffness increases with increasing volume fraction. For instance, the experimental stiffness of the MRE sample with f=9.09% is calculated as 0.63 N/cm while the stiffness of the MRE sample with f=36.36% is calculated as 1.67 N/cm when T= 203 mT. The stiffness increases with increasing magnetic field as well (magnetic field value is color-coded in Figure 4.1). For example, the experimental stiffness of the MRE sample with f=27.27% is 0.84 N/cm when there is no field, while it is calculated as 1.32 N/cm when T=203 mT. The stiffness of the MRE samples is summarized in Table 4.1.

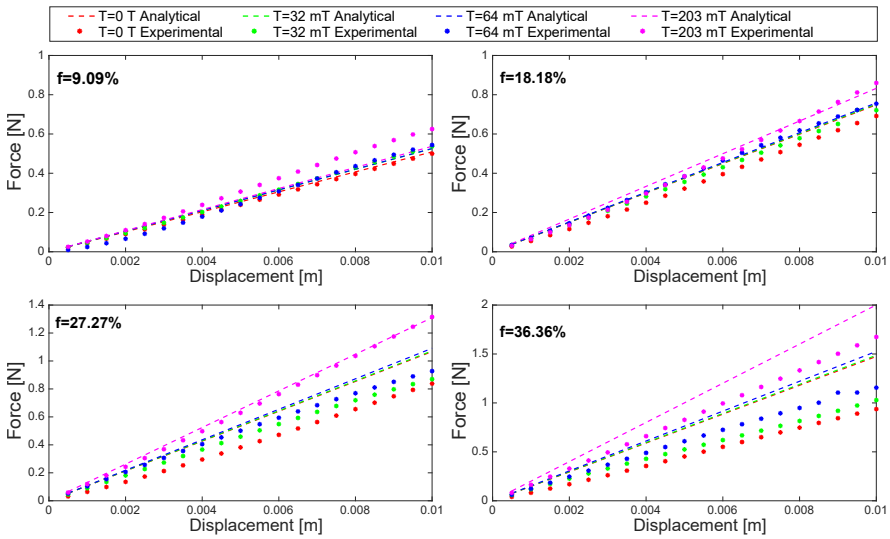

Figure 4.1. Comparison of experimental (dotted data points) and theoretical (developed by Lockette *et al.* [120] results: Force vs. displacement for the MRE samples with four different CIP volume fractions under four different magnetic fields.

Table 4.1. Experimental stiffness [N/cm] values for the MRE samples.

CIP volume fraction	**Magnetic Field**			
	T=0 mT	**T=32 mT**	**T=64 mT**	**T=203 mT**
f=9.09%	0.50	0.54	0.55	0.63
f=18.18%	0.69	0.72	0.75	0.86
f=27.27%	0.84	0.87	0.93	1.32
f=36.36%	0.94	1.03	1.16	1.67

In addition to the presented stiffness values, the percent error between the experimental stiffness and the analytical stiffness values were calculated as follows

$$Error = \frac{P_E - P}{P} 100, \tag{4.1}$$

where P_E and P represent the experimental and the analytical resultant force, respectively. The percent error between the experimental and analytical results is summarized in Table 4.2. The theoretical results partially agree with the experimental results for MRE containing 9.09% and 18.18% volume fractions. However, the error between the experimental and the analytical stiffness is higher for the MRE containing 27.27% and

36.36% volume fractions. The average error of the stiffness values between experimental and analytical results for all cases is calculated as 12.7 %. The results also indicate that the difference between experimental stiffness and theoretical stiffness increases with increasing volume fraction (f).

Table 4.2. Percent error between the experimental and the theoretical model results developed by Lockette *et al.*.

Volume	**Magnetic Field**			
Fraction	**T=0 mT**	**T=32 mT**	**T=64 mT**	**T=203 mT**
f=9.09%	1.8	2.2	3.4	16.4
f=18.18%	7.6	4.1	0.5	3.3
f=27.27%	21.5	18.9	15.0	0.4
f=36.36%	36.5	30.8	24.3	16.4

As mentioned in Section 3.1.1, the viscosity law relates E of composite materials to f, and Equation (3.16) is not valid for high-volume fractions. Therefore, it is obtained a higher-order equation that best fits the experimental data.

$$E = E_0(0.99 + 1.93f + 18.76f^2 - 37.07f^3) \tag{4.2}$$

The Maxwell-Garnett theory aims to approximate a complex electromagnetic medium in terms of permittivity and *f*. However, it generally underestimates the effect of c in Equation (3.14). We have fitted experimental data and established a third-order polynomial to calculate the effect of c

$$c = c_1 f^3 + c_2 f^2 + c_3 f + c_4, \tag{4.3}$$

where c_1, c_2, c_3, and c_4 were found using symbolic toolbox of MATLAB®.

We derived Equation (4.2) and Equation (4.3) based on the cantilever bending behavior of our MREs, which was our main contribution to the analytical equations. We have introduced a new analytical model and implemented it into Matlab. The results of the cantilever bending experiments were compared to the results obtained by the developed model (see Figure 4.2).

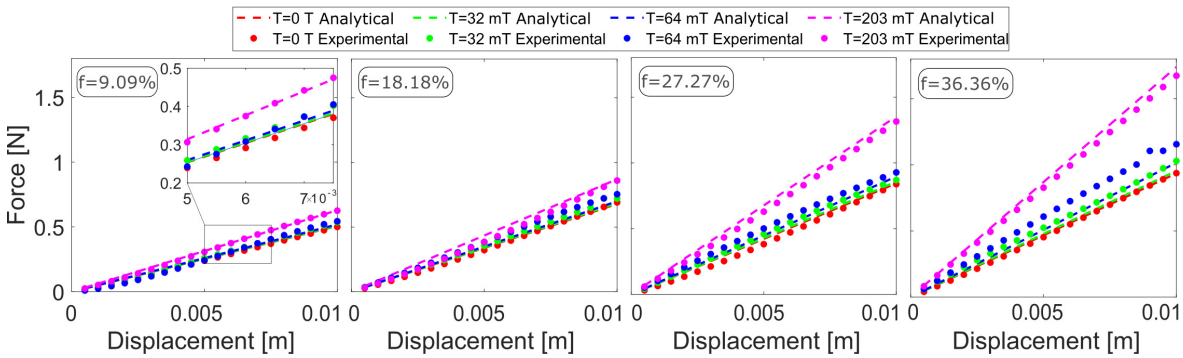

Figure 4.2. Comparison of experimental (dotted data points) and the developed analytical model (dashed lines) results: Tip force vs. displacement for the MRE samples with four different CIP volume fractions (f) under four different magnetic fields (color coded).

It can be inferred from Figure 4.2 that the equations fit better with our experimental data. The error percentages for the 16 cases can be seen in Table 4.3. The results indicate that the developed analytical results almost agree with the experimental results for four different volume fractions of MRE and four different magnetic fields. For instance, the percent error between the resultant experimental and analytical forces for the MRE sample with f=9.09% is 1.5%; the sample with f=36.36% volume fraction is 0.2% when there is no magnetic field. The average error of the stiffness values between experimental and analytical results for all cases is calculated as 3.9%. Thus, the developed model outperforms Lockette *et al.* model in capturing the field-dependent material properties of the developed MREs, especially for higher volume fractions.

Table 4.3. Percent error between the experimental results and the analytical model.

Volume	**Magnetic Field**			
Fraction	**T=0 mT**	**T=32 mT**	**T=64 mT**	**T=203 mT**
f=9.09%	1.5	5.2	4.8	0.5
f=18.18%	1.8	5.2	7.8	1.2
f=27.27%	0.8	1.4	3.5	2.8
f=36.36%	0.2	7.8	13.8	3.8

4.2. Magnetic Layer Jamming Results

The stress vs. strain curves of the MREs and NdFeB magnet tested under tensile tests are shown in Figure 4.3. The reader is referred to Appendix A for the multi-cycle test and friction results. The results indicate that the mechanical behavior of the MREs is nonlinear. The Neo-Hookean model was selected to obtain the mechanical properties of the MRE samples and the NdFeB magnet since it is the simplest form of all hyperelastic models and suitable for 25% strain. Furthermore, apart from the uniaxial tensile test, it is required to perform biaxial tension and shear tests to characterize a hyperelastic material fully. The Neo Hookean model response is reliable in the three-point bending test. The strain energy function of the Neo-Hookean model is expressed as

$$W = \frac{\mu}{2}(\bar{I}_1 - 3) + \frac{1}{D_1}(J-1)^2, \tag{4.4}$$

where μ is the shear modulus, D_1 is the incompressibility factor, J is the Jacobian, and $\bar{I}_1$ is the first invariant of the strain tensor. The material constants μ and D_1 are obtained from the curve fitting on the experimental tensile test data and DIC measurements, respectively. The material properties are shown in Table 4.4.

$$D_1 = \frac{6(1-2\nu)}{E}, \tag{4.5}$$

where ν is Poisson's ratio.

Table 4.4. Material properties for the MRE samples and the NdFeB sample.

Sample	**Density [g/cc]**	μ **[MPa]**	D_1 $[MPa^{-1}]$	**COF with an identical material**	**COF with NdFeB**
PDMS	1.25	0.19	1.99	1.42	1.35
f=0.1	1.64	0.30	1.73	1.03	0.84
f=0.2	2.30	0.52	1.26	1.1	0.72
f=0.3	2.93	0.75	0.58	0.8	0.67
f=0.4	3.62	1.30	0.5	0.62	0.48
NdFeB	5.00	1.35	0.52	N/A	N/A

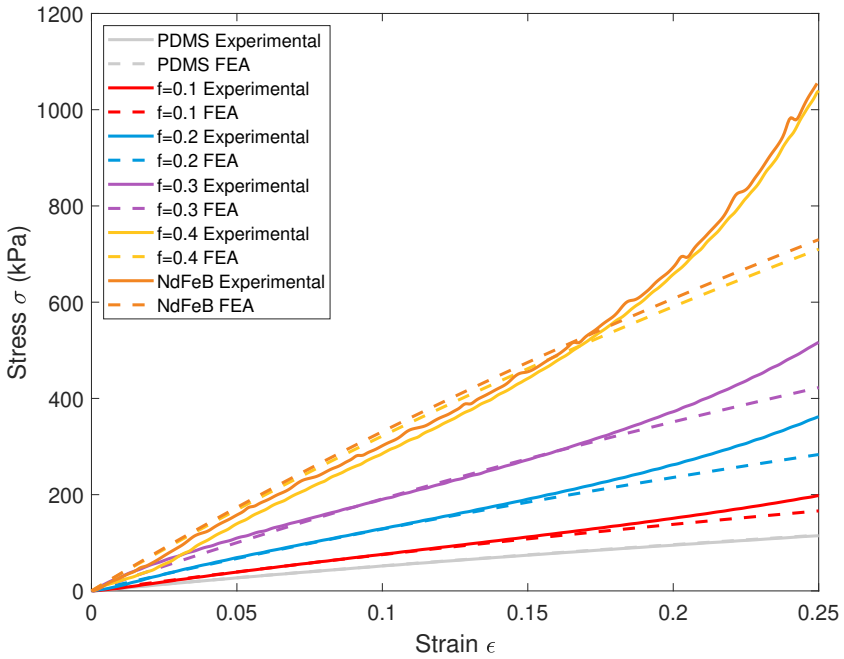

Figure 4.3. Stress vs. strain for the MRE samples with different volume fractions (f) and the NdFeB magnet. The experimental and FEA results are represented as solid and dashed lines, respectively.

The results of the magnetic surface force of the flexible NdFeB magnets are shown in Figure 4.4. The results show that the magnetic force generated from the magnets increases when a higher volume fraction of MRE is used at the core. For instance, the flexible magnet offers an average magnetic force of 0.49 N, 0.52 N, 0.54 N, 0.55 N, 0.56 N for f=0 (PDMS), f=0.1, f=0.2, f=0.3, f=0.4, respectively when there is no deflection. In addition, the magnetic force decreases as the deflection (δ) of the model increases. For instance, the average magnetic force of the top magnet is decreased from 0.52 N to 0.28 N, whereas the average magnetic force of the bottom magnet is decreased from 0.52 N to 0.17 N when f=0.1. The results also indicate that the difference between the force values produced by the top and bottom magnets increases as the deflection increases. The reason is due to the fact that the radius of curvature of the magnets increases as the layer jamming structure deflected, affecting the uniformity of the magnetic force distribution.

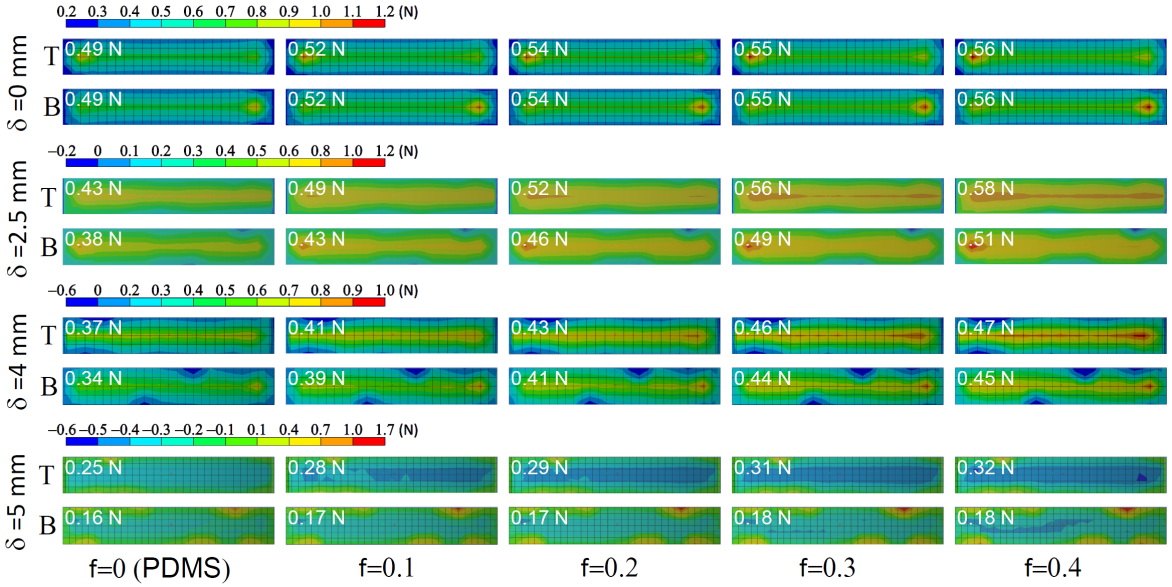

Figure 4.4. Top view of magnetic force contours of the flexible magnets. The average magnetic force values obtained from the magnets are shown in the upper left corner for each image. T and B represent the top and the bottom flexible magnets, respectively.

Figure 4.5 shows the results of the 3-point bending test of the multilayer jamming structure. Slopes of the resulting force vs. deflection curve give bending stiffness values of the structure. The results indicate that the resulting force shows a linear behavior ($R^2 \geq 0.993$) with deflection for each case. The results also indicate that the pre-slip stiffness of the jammed structure is higher than that of the unjammed structure for each case. It is an expected result since magnetic forces jam the MRE layers, and the overall stiffness of the structure increases. The stiffness values for each case are summarized in Table 4.5. It can be inferred from Table 4.5 that the stiffness of the jamming structure in the OFF State decreases when the number of layers is increased. For instance, when f =0.2, the stiffness of the structure with 3-layer, 4-layer, and 7-layer are calculated as 0.52 N/mm, 0.38 N/mm, and 0.30 N/mm, respectively. The FEA results have very similar results for this case. The values are 0.53 N/mm, 0.35 N/mm, and 0.29 N/mm, respectively.

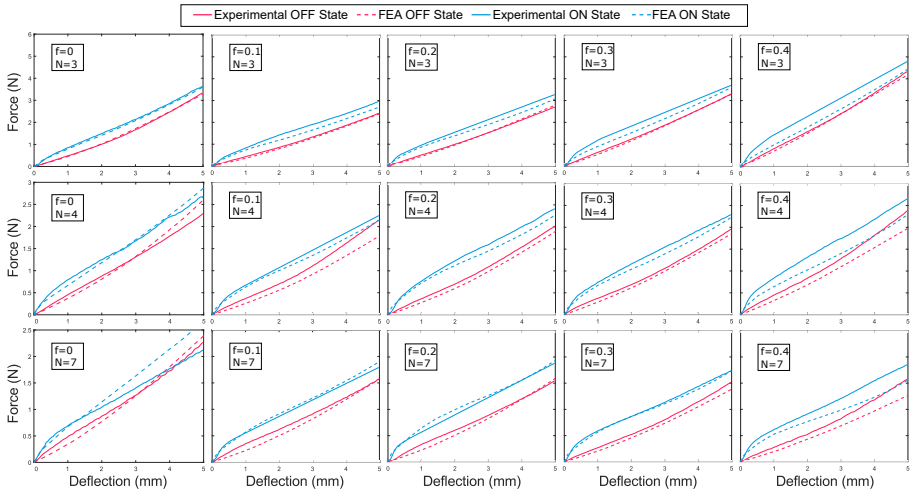

Figure 4.5. Finite element analysis (dashed lines) and experimental (solid lines) results for N-layer jamming structures. Blue and red color stand for *ON* States and *OFF* States, respectively. The structures were loaded in three-point bending for the magnetized NdFeB magnet and the non-magnetized NdFeB magnet for each MRE with different volume fractions.

Table 4.5. Stiffness [N/mm] values of the multilayer jamming structure.

Sample	**State**	**N=3**		**N=4**		**N=7**	
		Exp*	**FEA**	**Exp***	**FEA**	**Exp***	**FEA**
PDMS	OFF	0.6	0.61	0.45	0.47	0.44	0.44
	ON	1.08	1.19	1.05	1.14	1.03	1.05
f=0.1	OFF	0.46	0.46	0.40	0.36	0.31	0.33
	ON	1.15	1.14	0.93	1.13	0.87	1.05
f=0.2	OFF	0.52	0.51	0.38	0.34	0.30	0.28
	ON	1.50	1.61	1.02	1.24	1.04	1.16
f=0.3	OFF	0.64	0.62	0.37	0.35	0.28	0.27
	ON	1.67	1.4	1.14	1.20	0.97	1.43
f=0.4	OFF	0.84	0.84	0.45	0.40	0.29	0.25
	ON	2.14	1.85	1.43	1.58	1.07	1.47

* Experiments

In addition to the presented stiffness values for the multilayer MRE jamming structure, change in stiffness values is calculated for each volume fraction and the number of layers. Let K be the ratio of the stiffness of the jammed structure to the stiffness of the unjammed structure. The results (see Figure 4.6) show that simulation results are larger than experimental results. The reason is that the magnetic properties of the NdFeB magnet are less than the simulation values due to the attenuation effect caused by the losses in the production stage. In addition, K increases with the increasing number of layers stacked within the jamming structure. For instance, when f=0.4, the stiffness ratio of the jamming structure with 3-layer, 4-layer, and 7-layer is calculated as 2.21, 3.95, and 5.63, respectively. However, this situation is not valid for the experiment results for f=0.1 and f=0.2. The value K is slightly decreasing from N=3 to N=4. The main reason for this situation is that the number of friction contact types differs. There are two different friction interactions when N=4 (MRE-to-MRE and MRE-to-NdFeB), whereas there is only one (MRE-to-NdFeB) when N=3. The results show that the best performance was obtained when N=7 and f=0.4.

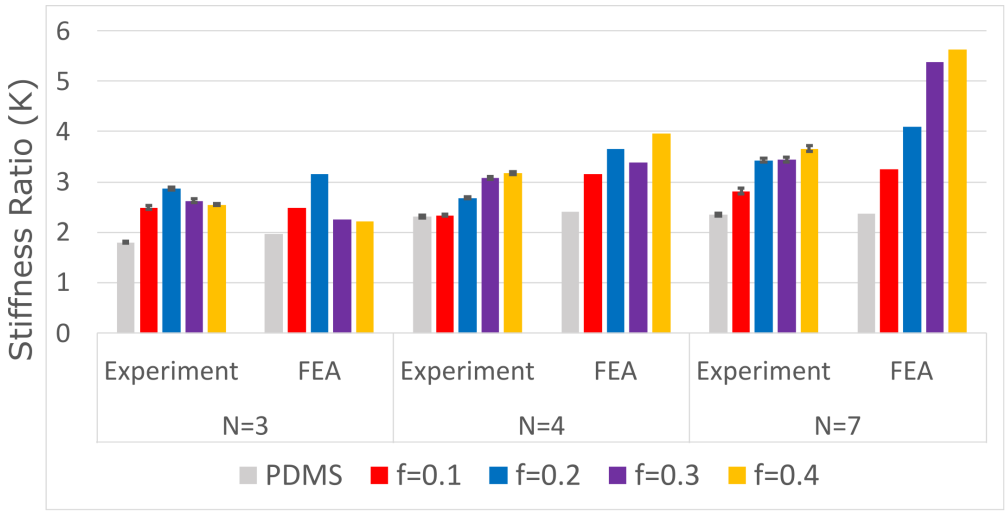

Figure 4.6. The mean of the stiffness ratio of the MRE-based layer jamming structures. The bars represent the standard deviation of the experimental results.

The main reason to use MREs in the middle layers is to benefit from viscoelasticity change in MREs under a magnetic field. We can observe changes in stiffness caused by the jamming and MR effects. For instance, when N=7, the experimental K value of the

PDMS is 2.35, which is solely due to jamming. On the other hand, the corresponding K value is 3.66 for f=0.4. This increase in stiffness change can be attributed to both the MR effect and the increase in magnetic jamming force due to iron particles in the MRE layers. In any case, these results show the benefit of using MREs in a layer-jamming structure.

The stiffness change is theoretically proportional to the square of the number of layers involved in layer jamming. According to this theory, the resulting stiffness ratios would be K = 9, 16, 49 for N=3, 4, 7 respectively. However, the experimentally obtained values for f=0.4 are 2.55, 3.17, and 3.66 for N=3, 4, and 7, respectively. It is obvious that the N^2 relationship does not work. The main reason for this may be due to the way jamming force is applied. For a pneumatic continuous layer jamming system, the jamming force is generated by applying a vacuum to a sealed and thin membrane. Unlike pneumatic jamming, no uniform pressure is acting on the entire outer surface of our jamming structure.

The results also show that this increased stiffness is only sustained under a limited range of loads. For 16 cases, the mean slip point for the experiments and finite element simulations was calculated as 0.35 mm and 0.16 mm, respectively. Full slip occurs when deflection is 0.88 mm for the experiments and the simulations. Although the experiments and the simulations experience the full-slip region at almost the same points, the simulations reach the slip point earlier. It is because it was assumed constant coefficient of friction and used coefficient of kinetic friction in the simulations instead of coefficient of static friction.

4.3. Magnetic Fiber Jamming Results

The experimental tests described in Section 3.3.3 are presented here. It includes fiber jamming structure performances in terms of bending and elongation capability and stiffening variation range.

The relationship between the pressure placed on the chambers and the corresponding bending angle is illustrated in Figure 4.7. The results indicate that similar behavior between one-chamber and two-chamber activation is observed until the applied pressure is reached 0.3 bar. Beyond that point, there is an increasing trend with one actuation chamber. A higher bending angle is obtained when one chamber is actuated. The structures with seven fibers used in the stiffening chamber are observed to be saturated at around 0.9 bar pressure when one line is pressurized. On the other hand, the same structures can stand 0.5 bar pressure when two pressure lines are inflated. The capture images can be seen in Figure 4.7. Omnidirectional bending tests showed that it is possible to bend the structure at an angle of 66.2 degrees when only one chamber is inflated at 0.9 bar pressure and 24.4 degrees when using two chambers simultaneously at 0.5 bar pressure. As for elongation, three chambers were activated simultaneously to calculate the elongation. However, we could not observe a pure elongation. The structure initially bent and then continued to elongate.

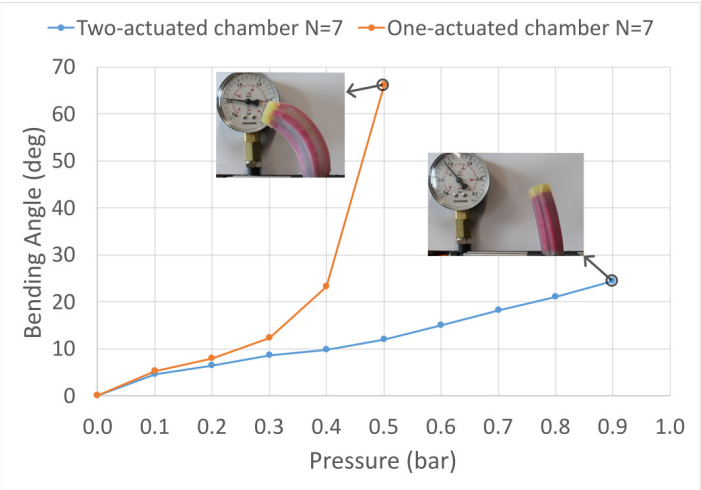

Figure 4.7. Bending capacity of a single module under increasing pressure: the blue color line indicates activation of two chambers; the orange color line indicates activation of a single chamber.

The results of the compression tests of the fiber jamming structure are shown in Figure 4.8(a,b). The results indicate that the resultant stress upon loading shows a nearly linear behavior (R^2 >0.9960) with strain for each case. Slopes of the stress

vs. strain curves give compression modulus values of the fiber jamming structures. It can be inferred from the figures that the compression modulus increases when the magnetized NdFeB magnets are used in the structure. For instance, the modulus of the OFF state structure is calculated as 394.9 kPa when N=1, while the ON state modulus is calculated as 436.84 kPa. In addition, the results indicate that the compression modulus decreases with increasing N. For example, the modulus of the unjammed structure when N=7 is 378.4 kPa, while it is calculated as 394.9 kPa when N=1. The results of the cantilever bending tests of the fiber jamming structure are shown in Figure 4.8(c,d). The stress-strain curves exhibited a highly noticeable hysteresis behavior. The area between the curves signifies the amount of dissipated energy. The slope of the force vs. displacement curves upon loading gives the stiffness value of the fiber jamming structure. The results indicate that the resulting stiffness increases when the magnetized NdFeB magnets are used in the jamming structure. For instance, the OFF state stiffness of the structure with a single piece of MRE is calculated as 0.39 N/cm while the ON state stiffness is calculated as 0.43 N/cm in cantilever bending tests. In addition, the corresponding increase is also observed when N=7. The stiffness is increased from 0.33 N/cm to 0.4 N/cm.

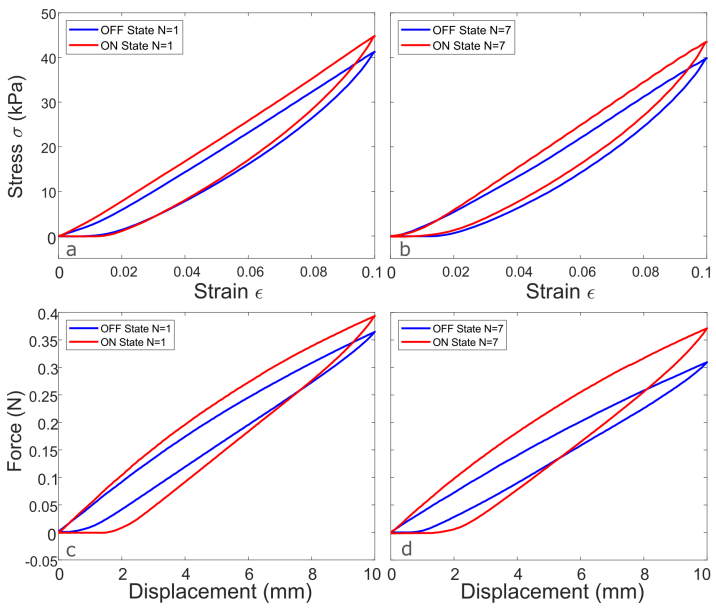

Figure 4.8. The stiffening tests: The structures were compressed in (a) and (b). The structures were performed in cantilever bending tests in (c) and (d).

In addition to the presented stiffness values for the fiber jamming structures, the stiffness ratio, K, is calculated as well. The cantilever bending results show that K increases with increasing N. For instance, K is 1.1 when $N = 1$ while it is 1.21 when N=7. As for compression tests, the change in modulus is calculated as 1.11 for each case. Considering the fact that axially-oriented fibers in a jamming structure have no effect on stiffness change under compression. Hence, the change in stiffness can be considered due to the MRE effect. The optimal stiffness change of the structure is observed when N=7. We observed a 21.2% increase in the stiffness variation of the structure. The theoretical stiffness change of the fiber jamming structure is presented in Section 2.3.2.2. According to the theory, the resulting stiffness change would be K=8.61 for N=7. However, we obtained K=1.21 from the experiments. The main reason is that there is a considerable amount of unjammed material in the structure. The diameter of the jammed region is 6.5 mm, while the structure's diameter is 17 mm. The K value can be optimized by performing the stiffening tests of fiber jamming structure with MRE fibers containing different volume fractions *f*. The results of the fiber jamming structure are summarized in Table 4.6.

Table 4.6. The performance of the module.

Bending Angle (one chamber)	**Bending Angle (two chambers)**	**Elongation**	**Stiffness Variation**
66.2 deg	24.4 deg	N/A	21.2 %

The results of the layer jamming structures are promising for the stiffness variation of soft robots. However, the proposed structures have certain disadvantages. Despite its effectiveness in enhancing the stiffness of soft robots, the current form of the proposed hybrid stiffening method, which combines a jamming-based and a viscosity-based method, is not applicable to soft robots. The most significant drawback of this study is the jamming transition that is induced mechanically. The non-magnetized NdFeB magnets must be changed with the magnetized NdFeB magnets to make a transition from OFF State to ON State. The problem can be solved with an electronically-driven mechanism to alter the polarity of the NdFeB magnet. A proper

mechanism consists of a flexible magnet and a coil. Two microparticles with the same retentivity and different coercivity can be used to manufacture the magnet. A coil is wrapped around the magnet so that the polarity of the magnet is changed. Since the aim of this section was to focus on investigating the effect of magnetic jamming of MRE layers, we used permanent NdFeB magnets to generate magnetic fields. However, magnetic fields can be generated electronically using electromagnets or electro-permanent magnets (EPMs) for a possible implementation of electronically controlled jamming and stiffening [68].

4.4. Electronically-Controlled Magnetic Fiber Jamming Results

4.4.1. Simulation Results

In order to change the state of the EPM device from the OFF state to the ON state, the magnetic polarity of the AlNiCo magnet must be changed. The required pulse current to revert the pole direction is calculated assuming the term g in Equation (3.17) goes to zero, and the amount of ampere-turn is found as

$$N_m I_m = H_m L_m = 324. \tag{4.6}$$

On the other hand, magnetic simulation results give us the $N_m I_m$ term approximately as 1200 (see Figure 4.9). The simulation result does not correspond with the theory. It is because the term g is assumed to be zero. Assuming the number of coil turn in an EPM is 80, the required current pulse is calculated as 15 A. The magnetic simulation force provided to the MRE material by the EPM was found as 0.46 N. Since we have three EPMs, the amount of jamming force at the tip is calculated as 1.38 N.

The magnetic flux density of the overall model in the xz plane is shown in Figure 4.10. The simulation results show that the volume average value of the magnetic flux density passing through the MRE fibers when the EPM devices in ON states and in OFF states are found as 0.2 mT and 16.7 mT, respectively. On the other hand, the volume average value of the magnetic flux density passing through hexagonal-shaped MREs is found as 200 mT.

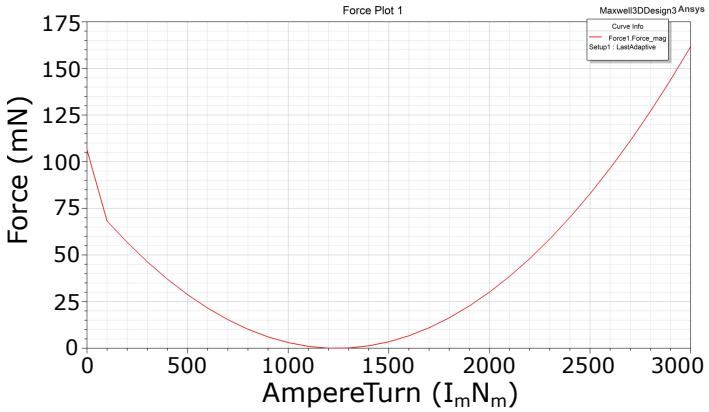

Figure 4.9. The amount of current-turn to switch the state of the EPM device.

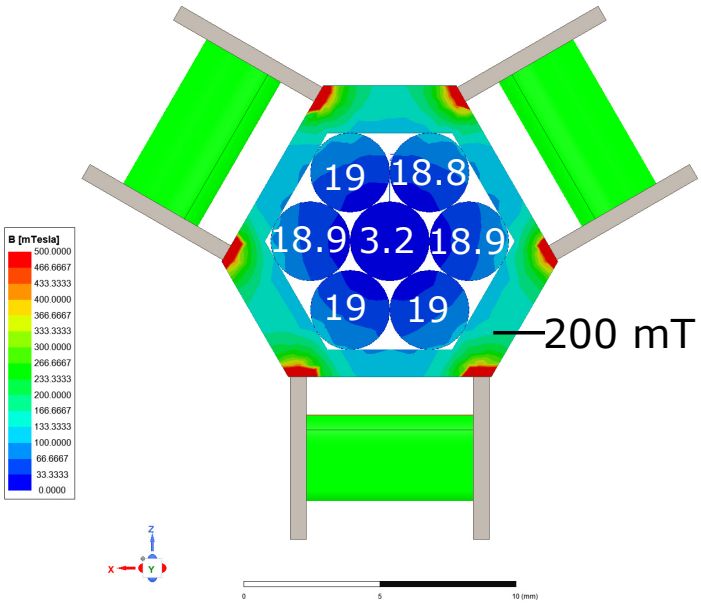

Figure 4.10. Magnetic flux density passing through the MRE fibers and the hexagonal-shaped MREs.

4.4.2. Experimental Results

The stiffness device integrated-STIFF-FLOP manipulator was performed in stiffening tests. Cantilever bending experiments were performed in the unjammed case (i.e., the EPMs are in the OFF state) and in the jammed case (i.e., the EPMs are in the OFF state). The cantilever bending test results are shown in Figure 4.11. The results indicate that no notable change in stiffness was observed for the following rea-

sons. The stiffness due to the MR effect disappeared due to the lost contact between the MRE samples and the EPM devices when the manipulator was deflected. In addition, stiffness change due to the jamming effect also suffered from contact loss. Furthermore, due to the geometrical constraints of the EPM devices, the outer diameter of the manipulator needed to be expanded. Abidi *et al.* [132] developed a STIFF-FLOP manipulator for MIS operations, reducing the outer diameter of the manipulator to 14.5 mm. It is approximately seven times softer than our robot. Contrary to the simulation results, the EPMs could not create enough magnetic force to jam the MRE fibers due to leakage flux and manufacturing errors such as improper coil winding and adhesive operation. The proposed device has some design problems. The EPM devices in the present form are not suitable for providing continuous jamming force. Although they are radially oriented at the base and the tip, they exert only discrete jamming forces, which have no effect on the jamming of the MRE fibers located in the main body. On the contrary, the presence of MRE fibers with a certain weight in this region has a detrimental impact on the stiffness change of the device. Furthermore, the EPMs located at the base do not affect stiffness change due to the jamming effect since the base was fixed in the cantilever bending experiment.

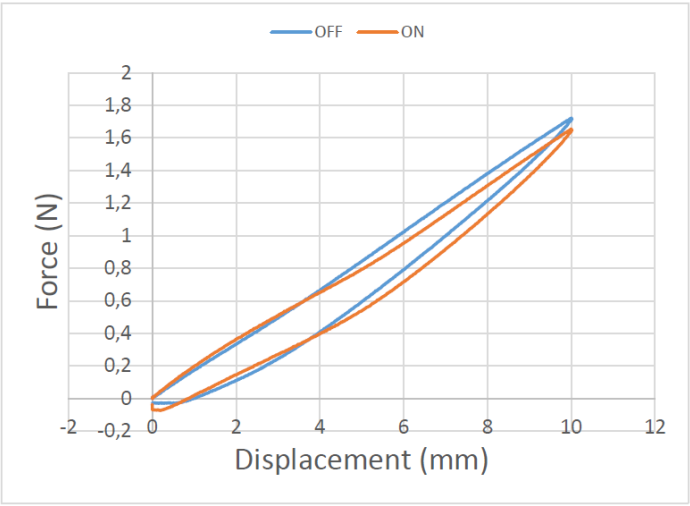

Figure 4.11. Cantilever bending results of the device integrated STIFF-FLOP manipulator.

5. CONCLUSION

In this thesis, a novel variable stiffness method combining jamming with viscoelasticity modification has been developed to achieve variable stiffness. The proposed method is innovative as it utilizes the benefits of magnetic jamming in MREs to enhance stiffness variation. We demonstrated the increase in stiffness by utilizing this hybrid method in the STIFF-FLOP manipulator under different deformation modes. The results indicate that the proposed hybrid stiffening method is promising for achieving variable and controllable stiffness in soft robots.

In Section 3.1, the cantilever bending behavior of MREs in terms of their dependence on the volume fraction of magnetizable particles and the external magnetic field was investigated. It is observed that isotropic MRE stiffness increases with increasing volume fraction and applied magnetic field. An analytical model was developed, and the analytical results were compared to the experimental ones. The analytical model capturing MREs' magnetorheological behavior is further improved by adding additional terms to the magnetoelastic governing equation described in Section 3.1.1, and the overall error was decreased.

In Section 3.2, we investigated the behavior of magnetically-induced jamming of magnetorheological elastomer layers as a first step towards a hybrid variable stiffness method. The MRE and NdFeB layers were characterized using uniaxial tensile tests supported with a DIC system. The bending stiffness of the jamming structure was tested using 3-point bending experiments, and finite element simulations validated the experiments. The multi-layer jamming structure composed of MRE and NdFeB layers has certain advantages. First, the response time of MREs is fast, i.e., the change in stiffness occurs instantaneously. Second, no vacuum actuation is needed for the jamming transition, which reduces the complexity of the structure. In addition, the destiffening (transition from rigid state to soft state) speed of the vacuum is slow, which is on the order of seconds. Finally, we proved that a higher stiffness variation was

achieved in the pre-slip regime when MREs were used instead of PDMS. This shows the benefit of the hybrid approach combining magnetic layer jamming with viscoelasticity change. The results show that this increased stiffness was only sustained under a limited range of loads. It is because shear forces at the interfaces between the MRE layers caused by magnetic forces are quite low. Furthermore, we showed the stiffness ratio increases when the number of MRE layers is increased within the multi-layer jamming structure.

In Section 3.3, we investigated the behavior of magnetically-induced jamming of MRE fibers. The fiber jamming structure consisting of MRE fibers and a flexible NdFeB magnet is implemented on the STIFF-FLOP manipulator. The stiffening tests were performed on the device-integrated manipulator. The tests were repeated with the magnetized and unmagnetized NdFeB magnets to explore the stiffness change. The manipulator achieved stiffness variation under different deformation modes, such as bending and compression.

Section 3.4 proposes a novel variable stiffness device consisting of MRE fibers and EPMs for soft robots. Stiffening tests were conducted on the device integrated-STIFF-FLOP manipulator to evaluate its stiffening capabilities. The desired change in stiffness could not be achieved as the reasons explained in Section 4.4.2. To address the limitations and challenges faced, it is recommended that the design of the EPM device needs to be revised. Although a considerable jamming force is exerted by an EPM device based on the simulation results, three EPMs could not produce a sufficient jamming effect for the device-integrated STIFF-FLOP manipulator. Instead of utilizing a discrete jamming principle, which is insufficient for soft robotic applications, an elevated design using a continuous jamming concept should be adopted. This may be possible with a more compact EPM device consisting of magnets with pole directions in the radial direction.

5.1. Contributions and Originality

The originality of this thesis is based on the development of a novel variable stiffness method utilizing two stiffening methods: a jamming-based method and a viscosity-based method. The proposed method is innovative since stiffness variation performance is boosted with this hybrid stiffening method with a less complex design and fast response time. The variable stiffness methods reviewed in the literature are compared in terms of stiffness variation, speed of stiffening, different modes of stiffening, and complexity. MREs are advantageous due to their fast response time and suitability for various stiffening modes. However, they require an extremely high magnetic field to achieve considerable stiffness variation. Jamming-based methods, on the other hand, are appealing due to their high stiffness variation capabilities, cost-effectiveness, and ease of fabrication. However, their integration into a system can be complicated because they require an external membrane. In addition, the speed of this method is not particularly fast. No research has been found in the literature that utilizes these two methods in a stiffening device. The stiffening method proposed in this thesis has the potential to achieve a high range of stiffness variation, a fast response time, and suitability for different modes when implemented in a soft manipulator.

5.2. Outlook and Future Work

The lack of a hybrid stiffening method providing stiffness change both due to jamming and variable viscosity in the literature has prompted us to work on this subject. We proposed a novel hybrid stiffening method and exhibited its efficacy in the jamming structures as a proof-of-concept. However, we could not achieve stiffness change in an actual robot implementation due to the reasons mentioned in Section 4.4.2.

Future work will be to enhance the electronically-controlled EPM device. The EPM devices utilized in the stiffening device provide only discrete jamming. Because most of the soft robotic tasks are performed in cylindrical coordinates, there is a need for

new EPM designs capable of providing jamming in the radial direction. One potential suggestion is to design an EPM device consisting of two nested hollow cylinder-shaped permanent magnets with radial magnetic polarization. Instead of using multiple EPMs in a stiffening device, which results in complexity in the implementation, a single EPM would enable continuous jamming to be achieved.

The stiffness variation of the proposed jamming structures can also be further improved with future research. First, the thickness or diameter of the manufactured MRE samples used in the jamming structures can be decreased using more advanced fabrication techniques such as micro molding and extrusion-based 3D printing. Therefore, more MRE layers or fibers can be stacked within the jamming structure. Second, anisotropic MRE samples can be used in the jamming structures. The CIP arrangement plays a vital role in determining the mechanical properties of the MREs. Third, the MR effect is boosted when anisotropic MRE samples are used within the jamming structure such that the magnetization direction of the NdFeB magnets and the direction of the CIPs are the same. In addition, MR materials used in the field active mode can deform in the direction of the applied field. Suppose a large external magnetic field is applied in the desired direction to the MR material. In that case, a magnetostriction effect is combined with a jamming phenomenon, leading to a performance boost in terms of change in stiffness. Fourth, the MR effect is increased when an elastomer matrix with a lower modulus is used in the MRE fabrication. Lastly, the curing temperature also plays a role in determining the rigidity of the manufactured elastomer-based materials. The lower the temperature, the softer the material is. Since the MR effect depends on elastomer modulus, stiffness of a jamming structure is increased if MRE samples cured at room temperature, which lasts approximately two days to manufacture, are used. During this long period, particle sedimentation appears, impairing the material's flexibility. Hence, the curing process should be supported with a continuous rotary motion mechanism.

REFERENCES

1. Kim, S., C. Laschi and B. Trimmer, "Soft Robotics: A Bioinspired Evolution in Robotics", *Trends in Biotechnology*, Vol. 31, No. 5, pp. 287–294, 2013.

2. Majidi, C., "Soft robotics: A Perspective—Current Trends and Prospects for the Future", *Soft Robotics*, Vol. 1, No. 1, pp. 5–11, 2014.

3. Trivedi, D., C. D. Rahn, W. M. Kier and I. D. Walker, "Soft robotics: Biological Inspiration, State of the Art, and Future Research", *Applied Bionics and Biomechanics*, Vol. 5, No. 3, pp. 99–117, 2008.

4. Venkatraman, S., F. Boey and L. L. Lao, "Implanted Cardiovascular Polymers: Natural, Synthetic and Bio-Inspired", *Progress in Polymer Science*, Vol. 33, No. 9, pp. 853–874, 2008.

5. Mammoto, T. and D. E. Ingber, "Mechanical Control of Tissue and Organ Development", *Development*, Vol. 137, No. 9, pp. 1407–1420, 2010.

6. Manti, M., V. Cacucciolo and M. Cianchetti, "Stiffening in Soft Robotics: A Review of the State of the Art", *IEEE Robotics & Automation Magazine*, Vol. 23, No. 3, pp. 93–106, 2016.

7. Wakimoto, S., I. Kumagai and K. Suzumori, "Development of Large Intestine Endoscope Changing Its Stiffness", *Proceedings of the 2009 IEEE International Conference on Robotics and Biomimetics*, Guilin, China, pp. 2320–2325, 2009.

8. Loeve, A., P. Breedveld and J. Dankelman, "Scopes Too Flexible... and Too Stiff", *IEEE Pulse*, Vol. 1, No. 3, pp. 26–41, 2010.

9. Langer, M., E. Amanov and J. Burgner-Kahrs, "Stiffening Sheaths for Continuum Robots", *Soft Robotics*, Vol. 5, No. 3, pp. 291–303, 2018.

10. Wang, T., J. Zhang, Y. Li, J. Hong and M. Y. Wang, "Electrostatic Layer Jamming Variable Stiffness for Soft Robotics", *IEEE/ASME Transactions on Mechatronics*, Vol. 24, No. 2, pp. 424–433, 2019.

11. Autumn, K., C. Majidi, R. Groff, A. Dittmore and R. Fearing, "Effective Elastic Modulus of Isolated Gecko Setal Arrays", *Journal of Experimental Biology*, Vol. 209, No. 18, pp. 3558–3568, 2006.

12. Yasa, O., Y. Toshimitsu, M. Y. Michelis, L. S. Jones, M. Filippi, T. Buchner and R. K. Katzschmann, "An Overview of Soft Robotics", *Annual Review of Control, Robotics, and Autonomous Systems*, Vol. 6, pp. 1–29, 2023.

13. Martinez, R. V., J. L. Branch, C. R. Fish, L. Jin, R. F. Shepherd, R. M. Nunes, Z. Suo and G. M. Whitesides, "Robotic Tentacles with Three-dimensional Mobility Based on Flexible Elastomers", *Advanced Materials*, Vol. 25, No. 2, pp. 205–212, 2013.

14. Mosadegh, B., P. Polygerinos, C. Keplinger, S. Wennstedt, R. F. Shepherd, U. Gupta, J. Shim, K. Bertoldi, C. J. Walsh and G. M. Whitesides, "Pneumatic Networks for Soft Robotics that Actuate Rapidly", *Advanced Functional Materials*, Vol. 24, No. 15, pp. 2163–2170, 2014.

15. Marchese, A. D., R. K. Katzschmann and D. Rus, "A Recipe for Soft Fluidic Elastomer Robots", *Soft Robotics*, Vol. 2, No. 1, pp. 7–25, 2015.

16. Hawkes, E. W., L. H. Blumenschein, J. D. Greer and A. M. Okamura, "A Soft Robot That Navigates Its Environment Through Growth", *Science Robotics*, Vol. 2, No. 8, p. eaan3028, 2017.

17. Talas, S. K., B. A. Baydere, T. Altinsoy, C. Tutcu and E. Samur, "Design and Development of a Growing Pneumatic Soft Robot", *Soft Robotics*, Vol. 7, No. 4, pp. 521–533, 2020.

18. McDonald, K. and T. Ranzani, "Hardware Methods for Onboard Control of Fluidically Actuated Soft Robots", *Frontiers in Robotics and AI*, p. 266, 2021.

19. Pelrine, R. E., R. D. Kornbluh and J. P. Joseph, "Electrostriction of Polymer Dielectrics with Compliant Electrodes as a Means of Actuation", *Sensors and Actuators A: Physical*, Vol. 64, No. 1, pp. 77–85, 1998.

20. Perju, E., Y. S. Ko, S. J. Dünki and D. M. Opris, "Increased Electromechanical Sensitivity of Polysiloxane Elastomers by Chemical Modification with Thioacetic Groups", *Materials & Design*, Vol. 186, p. 108319, 2020.

21. Huang, J., T. Lu, J. Zhu, D. R. Clarke and Z. Suo, "Large, Uni-Directional Actuation in Dielectric Elastomers Achieved by Fiber Stiffening", *Applied Physics Letters*, Vol. 100, No. 21, p. 211901, 2012.

22. Youn, J.-H., S. M. Jeong, G. Hwang, H. Kim, K. Hyeon, J. Park and K.-U. Kyung, "Dielectric Elastomer Actuator for Soft Robotics Applications and Challenges", *Applied Sciences*, Vol. 10, No. 2, p. 640, 2020.

23. Cianchetti, M., "Fundamentals on the Use of Shape Memory Alloys in Soft Robotics", *Interdisciplinary Mechatronics*, pp. 227–254, 2013.

24. Laschi, C., M. Cianchetti, B. Mazzolai, L. Margheri, M. Follador and P. Dario, "Soft Robot Arm Inspired by the Octopus", *Advanced Robotics*, Vol. 26, No. 7, pp. 709–727, 2012.

25. Abbott, J. J., E. Diller and A. J. Petruska, "Magnetic Methods in Robotics", *Annual Review of Control, Robotics, and Autonomous Systems*, Vol. 3, pp. 57–90, 2020.

26. Kim, Y. and X. Zhao, "Magnetic Soft Materials and Robots", *Chemical Reviews*, Vol. 122, No. 5, pp. 5317–5364, 2022.

27. Kim, Y., G. A. Parada, S. Liu and X. Zhao, "Ferromagnetic Soft Continuum Robots", *Science Robotics*, Vol. 4, No. 33, p. eaax7329, 2019.

28. Cianchetti, M., T. Ranzani, G. Gerboni, I. De Falco, C. Laschi and A. Menciassi, "STIFF-FLOP Surgical Manipulator: Mechanical Design and Experimental Characterization of the Single Module", *Proceedings of the 2013 IEEE/RSJ International Conference on Intelligent Robots and Systems*, Tokyo, Japan, pp. 3576–3581, 2013.

29. De Falco, I., M. Cianchetti and A. Menciassi, "A Soft and Controllable Stiffness Manipulator for Minimally Invasive Surgery: Preliminary Characterization of the Modular Design", *Proceedings of the IEEE Engineering in Medicine and Biology Society*, Chicago, USA, 2014.

30. Ranzani, T., M. Cianchetti, G. Gerboni, I. de Falco, G. Petroni and A. Menciassi, "A Modular Soft Manipulator with Variable Stiffness", *3rd Joint Workshop on New Technologies for Computer/Robot Assisted Surgery*, Verona, Italy, pp. 11–13, 2013.

31. Shiva, A., A. Stilli, Y. Noh, A. Faragasso, I. De Falco, G. Gerboni, M. Cianchetti, A. Menciassi, K. Althoefer and H. A. Wurdemann, "Tendon-Based Stiffening for a Pneumatically Actuated Soft Manipulator", *IEEE Robotics and Automation Letters*, Vol. 1, No. 2, pp. 632–637, 2016.

32. Carpi, F., G. Frediani, C. Gerboni, J. Gemignani and D. De Rossi, "Enabling Variable-Stiffness Hand Rehabilitation Orthoses with Dielectric Elastomer Transducers", *Medical Engineering & Physics*, Vol. 36, No. 2, pp. 205–211, 2014.

33. Correll, N., Ç. D. Önal, H. Liang, E. Schoenfeld and D. Rus, "Soft Autonomous Materials—Using Active Elasticity and Embedded Distributed Computation", *Experimental Robotics: The 12th International Symposium on Experimental Robotics*, Berlin, Germany, pp. 227–240, 2014.

34. Suzumori, K., S. Wakimoto, K. Miyoshi and K. Iwata, "Long Bending Rubber Mechanism Combined Contracting and Extending Fluidic Actuators", *Proceedings of the 2013 IEEE/RSJ International Conference on Intelligent Robots and Systems*, Tokyo, Japan, pp. 4454–4459, 2013.

35. Immega, G. and K. Antonelli, "The KSI Tentacle Manipulator", *Proceedings of the 1995 IEEE International Conference on Robotics and Automation*, Nagoya, Japan, pp. 3149–3154, 1995.

36. McMahan, W., B. A. Jones and I. D. Walker, "Design and Implementation of a Multi-section Continuum Robot: Air-Octor", *Proceedings of the 2005 IEEE/RSJ International Conference on Intelligent Robots and Systems*, Edmonton, Canada, pp. 2578–2585, 2005.

37. Stilli, A., H. A. Wurdemann and K. Althoefer, "Shrinkable, Stiffness-Controllable Soft Manipulator Based on a Bio-Inspired Antagonistic Actuation Principle", *Proceedings of the 2014 IEEE/RSJ International Conference on Intelligent Robots and Systems*, Chicago, USA, pp. 2476–2481, 2014.

38. Maghooa, F., A. Stilli, Y. Noh, K. Althoefer and H. A. Wurdemann, "Tendon and Pressure Actuation for a Bio-inspired Manipulator Based on an Antagonistic Principle", *Proceedings of the 2015 IEEE International Conference on Robotics and Automation*, Seattle, USA, pp. 2556–2561, 2015.

39. Nagase, J. Y., S. Wakimoto, T. Satoh, N. Saga and K. Suzumori, "Design of a Variable-stiffness Robotic Hand Using Pneumatic Soft Rubber Actuators", *Smart Materials and Structures*, Vol. 20, No. 10, p. 105015, 2011.

40. Cianchetti, M., M. Calisti, L. Margheri, M. Kuba and C. Laschi, "Bioinspired Locomotion and Grasping in Water: The Soft Eight-Arm OCTOPUS Robot", *Bioinspiration & Biomimetics*, Vol. 10, No. 3, p. 035003, 2015.

41. Henke, M. and G. Gerlach, "A Multi-layered Variable Stiffness Device Based on Smart Form Closure actuators", *Journal of Intelligent Material Systems and Structures*, Vol. 27, No. 3, pp. 375–383, 2016.

42. Henke, M., J. Sorber and G. Gerlach, "Multi-layer Beam with Variable Stiffness Based on Electroactive Polymers", *Proceedings of the Electroactive Polymer Actuators and Devices 2012*, Vol. 8340, pp. 412–424, 2012.

43. Cheng, N. G., A. Gopinath, L. Wang, K. Iagnemma and A. E. Hosoi, "Thermally Tunable, Self-Healing Composites for Soft Robotic Applications", *Macromolecular Materials and Engineering*, Vol. 299, No. 11, pp. 1279–1284, 2014.

44. McEvoy, M. A. and N. Correll, "Thermoplastic Variable Stiffness Composites with Embedded, Networked Sensing, Actuation, and Control", *Journal of Composite Materials*, Vol. 49, No. 15, pp. 1799–1808, 2015.

45. Shan, W., T. Lu and C. Majidi, "Soft-Matter Composites with Electrically Tunable Elastic Rigidity", *Smart Materials and Structures*, Vol. 22, No. 8, p. 085005, 2013.

46. Schubert, B. E. and D. Floreano, "Variable Stiffness Material Based on Rigid Low-Melting-Point-Alloy Microstructures Embedded in Soft Poly (Dimethylsiloxane)(PDMS)", *Rsc Advances*, Vol. 3, No. 46, pp. 24671–24679, 2013.

47. Shintake, J., B. Schubert, S. Rosset, H. Shea and D. Floreano, "Variable Stiffness Actuator for Soft Robotics Using Dielectric Elastomer and Low-Melting-Point Alloy", *Proceedings of the 2015 IEEE/RSJ International Conference on Intelligent Robots and Systems*, pp. 1097–1102, 2015.

48. Gandhi, F. and S.-G. Kang, "Beams with Controllable Flexural Stiffness", *Smart Materials and Structures*, Vol. 16, No. 4, p. 1179, 2007.

49. Mcknight, G., R. Doty, A. Keefe, G. Herrera and C. Henry, "Segmented Re-

inforcement Variable Stiffness Materials for Reconfigurable Surfaces", *Journal of Intelligent Material Systems and Structures*, Vol. 21, No. 17, pp. 1783–1793, 2010.

50. Chenal, T. P., J. C. Case, J. Paik and R. K. Kramer, "Variable Stiffness Fabrics with Embedded Shape Memory Materials for Wearable Applications", *Proceedings of the 2014 IEEE/RSJ International Conference on Intelligent Robots and Systems*, Chicago, USA, pp. 2827–2831, 2014.

51. Liu, A. J. and S. R. Nagel, "Jamming Is Not Just Cool Any More", *Nature*, Vol. 396, No. 6706, pp. 21–22, 1998.

52. van Hecke, M., "Jamming of Soft Particles: Geometry, Mechanics, Scaling and Isostaticity", *Journal of Physics: Condensed Matter*, Vol. 22, No. 3, p. 033101, 2009.

53. Bi, D., J. Zhang, B. Chakraborty and R. P. Behringer, "Jamming by Shear", *Nature*, Vol. 480, No. 7377, pp. 355–358, 2011.

54. Aktaş, B., Y. S. Narang, N. Vasios, K. Bertoldi and R. D. Howe, "A Modeling Framework for Jamming Structures", *Advanced Functional Materials*, Vol. 31, No. 16, p. 2007554, 2021.

55. Brown, E., N. Rodenberg, J. Amend, A. Mozeika, E. Steltz, M. R. Zakin, H. Lipson and H. M. Jaeger, "Universal Robotic Gripper Based on the Jamming of Granular Material", *Proceedings of the National Academy of Sciences*, Vol. 107, No. 44, pp. 18809–18814, 2010.

56. Cheng, N. G., M. B. Lobovsky, S. J. Keating, A. M. Setapen, K. I. Gero, A. E. Hosoi and K. D. Iagnemma, "Design and Analysis of a Robust, Low-Cost, Highly Articulated Manipulator Enabled by Jamming of Granular Media", *Proceedings of the 2012 IEEE International Conference on Robotics and Automation*, Saint Paul, USA, pp. 4328–4333, 2012.

57. Kim, Y.-J., S. Cheng, S. Kim and K. Iagnemma, "Design of a Tubular Snake-like Manipulator with Stiffening Capability by Layer Jamming", *Proceedings of the 2012 IEEE/RSJ International Conference on Intelligent Robots and Systems*, Vilamoura-Algarve, Portugal, pp. 4251–4256, 2012.

58. Kim, Y.-J., S. Cheng, S. Kim and K. Iagnemma, "A Novel Layer Jamming Mechanism with Tunable Stiffness Capability for Minimally Invasive Surgery", *IEEE Transactions on Robotics*, Vol. 29, No. 4, pp. 1031–1042, 2013.

59. Ou, J., L. Yao, D. Tauber, J. Steimle, R. Niiyama and H. Ishii, "jamSheets: Thin Interfaces with Tunable Stiffness Enabled by Layer Jamming", *Proceedings of the 8th International Conference on Tangible, Embedded and Embodied Interaction*, Munich, Germany, pp. 65–72, 2014.

60. Narang, Y. S., J. J. Vlassak and R. D. Howe, "Mechanically Versatile Soft Machines Through Laminar Jamming", *Advanced Functional Materials*, Vol. 28, No. 17, p. 1707136, 2018.

61. Brancadoro, M., M. Manti, F. Grani, S. Tognarelli, A. Menciassi and M. Cianchetti, "Toward a Variable Stiffness Surgical Manipulator Based on Fiber Jamming Transition", *Frontiers in Robotics and AI*, Vol. 6, p. 12, 2019.

62. Brancadoro, M., M. Manti, S. Tognarelli and M. Cianchetti, "Fiber Jamming Transition as a Stiffening Mechanism for Soft Robotics", *Soft Robotics*, Vol. 7, No. 6, pp. 663–674, 2020.

63. Vasios, N., Y. Narang, B. Aktaş, R. Howe and K. Bertoldi, "Numerical Analysis of Periodic Laminar and Fibrous Media Undergoing a Jamming Transition", *European Journal of Mechanics-A/Solids*, Vol. 75, pp. 322–329, 2019.

64. Arleo, L., L. Lorenzon and M. Cianchetti, "Variable Stiffness Linear Actuator Based on Differential Drive Fiber Jamming", *IEEE Transactions on Robotics*,

2023.

65. Majidi, C. and R. J. Wood, "Tunable Elastic Stiffness with Microconfined Magnetorheological Domains at Low Magnetic Field", *Applied Physics Letters*, Vol. 97, No. 16, p. 164104, 2010.

66. Cao, C. and X. Zhao, "Tunable Stiffness of Electrorheological Elastomers by Designing Mesostructures", *Applied Physics Letters*, Vol. 103, No. 4, p. 041901, 2013.

67. McDonald, K., A. Rendos, S. Woodman, K. A. Brown and T. Ranzani, "Magnetorheological Fluid-Based Flow Control for Soft Robots", *Advanced Intelligent Systems*, Vol. 2, No. 11, p. 2000139, 2020.

68. Gaeta, L. T., K. J. McDonald, L. Kinnicutt, M. Le, S. Wilkinson-Flicker, Y. Jiang, T. Atakuru, E. Samur and T. Ranzani, "Magnetically Induced Stiffening for Soft Robotics", *Soft Matter*, Vol. 19, No. 14, pp. 2623–2636, 2023.

69. Li, Y., J. Li, T. Tian and W. Li, "A Highly Adjustable Magnetorheological Elastomer Base Isolator for Applications of Real-Time Adaptive Control", *Smart Materials and Structures*, Vol. 22, No. 9, p. 095020, 2013.

70. Li, Y., J. Li, W. Li and H. Du, "A State-of-the-Art Review on Magnetorheological Elastomer Devices", *Smart Materials and Structures*, Vol. 23, No. 12, p. 123001, 2014.

71. Popp, K. M., M. Kröger, W. h. Li, X. Z. Zhang and P. B. Kosasih, "MRE Properties under Shear and Squeeze Modes and Applications", *Journal of Intelligent Material Systems and Structures*, Vol. 21, No. 15, pp. 1471–1477, 2010.

72. Carlson, J. D. and M. R. Jolly, "MR Fluid, Foam and Elastomer Devices", *Mechatronics*, Vol. 10, No. 4-5, pp. 555–569, 2000.

73. Kallio, M., *The Elastic and Damping Properties of Magnetorheological Elastomers*, Technical Research Centre of Finland, Espoo, Finland, 2005.

74. Wu, J., X. Gong, Y. Fan and H. Xia, "Anisotropic Polyurethane Magnetorheological Elastomer Prepared Through In Situ Polycondensation under a Magnetic Field", *Smart Materials and Structures*, Vol. 19, No. 10, p. 105007, 2010.

75. Munoz, B. and M. Jolly, *Performance of Plastics*, Carl Hanser Verlag, Munich, Germany, 2001.

76. Burhannuddin, N. L., N. A. Nordin, S. A. Mazlan, S. A. A. Aziz, N. Kuwano, S. K. M. Jamari and Ubaidillah, "Physicochemical Characterization and Rheological Properties of Magnetic Elastomers Containing Different Shapes of Corroded Carbonyl Iron Particles", *Scientific Reports*, Vol. 11, No. 1, p. 868, 2021.

77. Jung, H. S., S. H. Kwon, H. J. Choi, J. H. Jung and Y. G. Kim, "Magnetic Carbonyl Iron/natural Rubber Composite Elastomer and Its Magnetorheology", *Composite Structures*, Vol. 136, pp. 106–112, 2016.

78. Lee, C. J., S. H. Kwon, H. J. Choi, K. H. Chung and J. H. Jung, "Enhanced Magnetorheological Performance of Carbonyl Iron/natural Rubber Composite Elastomer with Gamma-ferrite Additive", *Colloid and Polymer Science*, Vol. 296, pp. 1609–1613, 2018.

79. Dargahi, A., R. Sedaghati and S. Rakheja, "On the Properties of Magnetorheological Elastomers in Shear mode: Design, Fabrication and Characterization", *Composites Part B: Engineering*, Vol. 159, pp. 269–283, 2019.

80. Lokander, M. and B. Stenberg, "Performance of Isotropic Magnetorheological Rubber Materials", *Polymer Testing*, Vol. 22, No. 3, pp. 245–251, 2003.

81. Boczkowska, A., S. F. Awietjan, S. Pietrzko and K. J. Kurzydłowski, "Mechanical Properties of Magnetorheological Elastomers Under Shear Deformation", *Com-*

posites Part B: Engineering, Vol. 43, No. 2, pp. 636–640, 2012.

82. Kumar, V. and D.-J. Lee, "Iron Particle and Anisotropic Effects on Mechanical Properties of Magneto-Sensitive Elastomers", *Journal of Magnetism and Magnetic Materials*, Vol. 441, pp. 105–112, 2017.

83. Zheng, D., T. Liu, L. Zhou and Y. Xu, "Electromagnetic Absorbing Property of the Flaky Carbonyl Iron Particles by Chemical Corrosion Process", *Journal of Magnetism and Magnetic Materials*, Vol. 419, pp. 119–124, 2016.

84. Hapipi, N. M., S. A. Mazlan, M. H. A. Khairi and N. Mohamad, "The Damping Properties of Plate-like Magnetorheological Elastomer", *Key Engineering Materials*, Vol. 772, pp. 56–60, 2018.

85. Wang, F., C. Long, T. Wu, W. Li, Z. Chen, F. Xia, J. Wu and J. Guan, "Enhancement of Low-Frequency Magnetic Permeability and Absorption by Texturing Flaky Carbonyl Iron Particles", *Journal of Alloys and Compounds*, Vol. 823, p. 153827, 2020.

86. Tian, T., W. Li, G. Alici, H. Du and Y. Deng, "Microstructure and Magnetorheology of Graphite-based MR Elastomers", *Rheologica Acta*, Vol. 50, No. 9-10, pp. 825–836, 2011.

87. Liao, G., X. Gong, S. Xuan, C. Kang and L. Zong, "Development of a Real-Time Tunable Stiffness and Damping Vibration Isolator Based on Magnetorheological Elastomer", *Journal of Intelligent Material Systems and Structures*, Vol. 23, No. 1, pp. 25–33, 2012.

88. Shen, Y., M. F. Golnaraghi and G. R. Heppler, "Experimental Research and Modeling of Magnetorheological Elastomers", *Journal of Intelligent Material Systems and Structures*, Vol. 15, No. 1, pp. 27–35, 2004.

89. Deng, H.-x., X.-l. Gong and L.-h. Wang, "Development of an Adaptive Tuned

Vibration Absorber with Magnetorheological Elastomer", *Smart Materials and Structures*, Vol. 15, No. 5, p. N111, 2006.

90. Li, R., X. Li, Y. Li, P.-a. Yang and J. Liu, "Experimental and Numerical Study on Surface Roughness of Magnetorheological Elastomer for Controllable Friction", *Friction*, Vol. 8, No. 5, pp. 917–929, 2020.

91. Rabinow, J., "The Magnetic Fluid Clutch", *Electrical Engineering*, Vol. 67, No. 12, pp. 1167–1174, 1948.

92. Rigbi, Z. and L. Jilken, "The Response of an Elastomer Filled with Soft Ferrite to Mechanical and Magnetic Influences", *Journal of Magnetism and Magnetic Materials*, Vol. 37, No. 3, pp. 267–276, 1983.

93. Jolly, M. R., J. D. Carlson, B. C. Muñoz and T. A. Bullions, "The Magneto-viscoelastic Response of Elastomer Composites Consisting of Ferrous Particles Embedded in a Polymer Matrix", *Journal of Intelligent Material Systems and Structures*, Vol. 7, No. 6, pp. 613–622, 1996.

94. Ginder, J. M., M. E. Nichols, L. D. Elie and J. L. Tardiff, "Magnetorheological Elastomers: Properties and Applications", *Proceedings of the Smart Structures and Materials 1999: Smart Materials Technologies*, Newport Beach, USA, pp. 131–138, 1999.

95. Ginder, J., S. Clark, W. Schlotter and M. Nichols, "Magnetostrictive Phenomena in Magnetorheological Elastomers", *International Journal of Modern Physics B*, Vol. 16, No. 17n18, pp. 2412–2418, 2002.

96. Zhou, G. Y. and Z. Y. Jiang, "Dynamic Deformation in MR Elastomer Driven by Magnetic Field", *Proceedings of the Smart Structures and Materials 2003: Active Materials: Behavior and Mechanics*, San Diego, USA, pp. 603–611, 2003.

97. Diguet, G., E. Beaugnon and J. Cavaillé, "Shape Effect in the Magnetostriction of

Ferromagnetic Composite", *Journal of Magnetism and Magnetic Materials*, Vol. 322, No. 21, pp. 3337–3341, 2010.

98. Gong, X., G. Liao and S. Xuan, "Full-Field Deformation of Magnetorheological Elastomer under Uniform Magnetic Field", *Applied Physics Letters*, Vol. 100, No. 21, 2012.

99. Stepanov, G., E. Y. Kramarenko and D. Semerenko, "Magnetodeformational Effect of the Magnetoactive Elastomer and Its Possible Applications", *Journal of Physics: Conference Series*, Vol. 412, pp. 012–031, 2013.

100. Li, W., K. Kostidis, X. Zhang and Y. Zhou, "Development of a Force Sensor Working with MR Elastomers", *Proceedings of the International Conference on Advanced Intelligent Mechatronics*, Singapore, pp. 14–17, 2009.

101. Caglar, M. B., *Sensing Behavior of Magnetorheological Elastomers*, Ph.D. Thesis, University of Nevada, Reno, 2008.

102. Bica, I., "Compressibility Modulus and Principal Deformations in Magneto-Rheological Elastomer: The effect of the Magnetic Field", *Journal of Industrial and Engineering Chemistry*, Vol. 15, No. 6, pp. 773–776, 2009.

103. Boczkowska, A. and S. Awietjan, "Microstructure and Properties of Magnetorheological Elastomers", *Advanced Elastomers-Technology, Properties and Applications*, Vol. 595, 2012.

104. Li, W., X. Zhang and H. Du, "Magnetorheological Elastomers and Their Applications", *Advances in Elastomers I: Blends and Interpenetrating Networks*, pp. 357–374, Springer, 2013.

105. Zhou, Y., S. Jerrams, A. Betts and L. Chen, "The Effect of Microstructure on the Dynamic Equi-Biaxial Fatigue Behaviour of Magnetorheological Elastomers", *Constitutive Models for Rubber VIII*, pp. 701–706, CRC Press, 2013.

106. Schubert, G., *Manufacture, Characterisation and Modelling of Magneto-Rheological Elastomers*, Ph.D. Thesis, University of Glasgow, 2014.

107. Deng, H. and X. Gong, "Adaptive Tuned Vibration Absorber Based on Magnetorheological Elastomer", *Journal of Intelligent Material Systems and Structures*, Vol. 18, No. 12, pp. 1205–1210, 2007.

108. Deng, H.-x. and X.-l. Gong, "Application of Magnetorheological Elastomer to Vibration Absorber", *Communications in Nonlinear Science and Numerical Simulation*, Vol. 13, No. 9, pp. 1938–1947, 2008.

109. Lerner, A. A. and K. Cunefare, "Performance of MRE-Based Vibration Absorbers", *Journal of Intelligent Material Systems and Structures*, Vol. 19, No. 5, pp. 551–563, 2008.

110. Zhang, X. and W. Li, "Adaptive Tuned Dynamic Vibration Absorbers Working with MR Elastomers", *Smart Structures and Systems, An International Journal*, Vol. 5, No. 5, pp. 517–529, 2009.

111. Kim, Y.-K., H.-I. Bae, J.-H. Koo, K.-S. Kim and S. Kim, "Note: Real Time Control of a Tunable Vibration Absorber Based on Magnetorheological Elastomer for Suppressing Tonal Vibrations", *Review of Scientific Instruments*, Vol. 83, No. 4, 2012.

112. Li, W., X. Zhang and H. Du, "Development and Simulation Evaluation of a Magnetorheological Elastomer Isolator for Seat Vibration Control", *Journal of Intelligent Material Systems and Structures*, Vol. 23, No. 9, pp. 1041–1048, 2012.

113. Ni, Z., X. Gong, J. Li and L. Chen, "Study on a Dynamic Stiffness-Tuning Absorber with Squeeze-Strain Enhanced Magnetorheological Elastomer", *Journal of Intelligent Material Systems and Structures*, Vol. 20, No. 10, pp. 1195–1202, 2009.

114. Sun, S., Y. Chen, J. Yang, T. Tian, H. Deng, W. Li, H. Du and G. Alici, "The De-

velopment of an Adaptive Tuned Magnetorheological Elastomer Absorber Working in Squeeze Mode", *Smart Materials and Structures*, Vol. 23, No. 7, p. 075009, 2014.

115. Kavlicoglu, B., B. Wallis, H. Sahin and Y. Liu, "Magnetorheological Elastomer Mount for Shock and Vibration Isolation", *Proceedings of the Active and Passive Smart Structures and Integrated Systems 2011*, Vol. 7977, pp. 344–350, 2011.

116. Kallio, M., T. Lindroos, S. Aalto, E. Järvinen, T. Kärnä and T. Meinander, "Dynamic Compression Testing of a Tunable Spring Element Consisting of a Magnetorheological Elastomer", *Smart Materials and Structures*, Vol. 16, No. 2, p. 506, 2007.

117. Böse, H., T. Gerlach and J. Ehrlich, "Magnetorheological Elastomers—An Underestimated Class of Soft Actuator Materials", *Journal of Intelligent Material Systems and Structures*, Vol. 32, No. 14, pp. 1550–1564, 2021.

118. Kashima, S., F. Miyasaka and K. Hirata, "Novel Soft Actuator Using Magnetorheological Elastomer", *IEEE Transactions on Magnetics*, Vol. 48, No. 4, pp. 1649–1652, 2012.

119. Borcea, L. and O. Bruno, "On the Magneto-Elastic Properties of Elastomer–Ferromagnet Composites", *Journal of the Mechanics and Physics of Solids*, Vol. 49, No. 12, pp. 2877–2919, 2001.

120. von Lockette, P. v., S. Lofland, J. Biggs, J. Roche, J. Mineroff and M. Babcock, "Investigating New Symmetry Classes in Magnetorheological Elastomers: Cantilever Bending Behavior", *Smart Materials and Structures*, Vol. 20, No. 10, p. 105022, 2011.

121. Brown, W. F., *Magnetostatic Principles in Ferromagnetism*, North-Holland Publishing, Amsterdam, Netherlands, 1962.

122. Guth, E., "Theory of Filler Reinforcement", *Rubber Chemistry and Technology*, Vol. 18, No. 3, pp. 596–604, 1945.

123. Mullins, L. and N. Tobin, "Stress Softening in Rubber Vulcanizates. Part I. Use of a Strain Amplification Factor to Describe the Elastic Behavior of Filler-Reinforced Vulcanized Rubber", *Journal of Applied Polymer Science*, Vol. 9, No. 9, pp. 2993–3009, 1965.

124. Hintze, C., D. Y. Borin, D. Ivaneyko, V. Toshchevikov, M. Saphiannikova-Grenzer and G. Heinrich, "Soft Magnetic Elastomers with Controllable Stiffness: Experiments and Modelling", *Kautschuk Gummi Kunststoffe*, Vol. 67, No. 4, pp. 53–59, 2014.

125. Bira, N., P. Dhagat and J. R. Davidson, "A review of Magnetic Elastomers and Their Role in Soft Robotics", *Frontiers in Robotics and AI*, Vol. 7, p. 588391, 2020.

126. Kitano, S., T. Komatsuzaki, I. Suzuki, M. Nogawa, H. Naito and S. Tanaka, "Development of a Rigidity TunableFlexible Joint Using Magneto-Rheological Compounds—Toward a Multijoint Manipulator for Laparoscopic Surgery", *Frontiers in Robotics and AI*, Vol. 7, p. 59, 2020.

127. Diani, J., B. Fayolle and P. Gilormini, "A Review on the Mullins Effect", *European Polymer Journal*, Vol. 45, No. 3, pp. 601–612, 2009.

128. Graham, R. L., B. D. Lubachevsky, K. J. Nurmela and P. R. Östergård, "Dense Packings of Congruent Circles in a Circle", *Discrete Mathematics*, Vol. 181, No. 1-3, pp. 139–154, 1998.

129. McDonald, K. J., L. Kinnicutt, A. M. Moran and T. Ranzani, "Modulation of Magnetorheological Fluid Flow in Soft Robots Using Electropermanent Magnets", *IEEE Robotics and Automation Letters*, Vol. 7, No. 2, pp. 3914–3921, 2022.

130. Knaian, A. N., *Electropermanent Magnetic Connectors and Actuators: Devices and Their Application in Programmable Matter*, Ph.D. Thesis, Massachusetts Institute of Technology, 2010.

131. Fitzgerald, A. E., C. Kingsley, S. D. Umans and B. James, *Electric Machinery*, McGraw-Hill, New York, NY, USA, 2003.

132. Abidi, H., G. Gerboni, M. Brancadoro, J. Fras, A. Diodato, M. Cianchetti, H. Wurdemann, K. Althoefer and A. Menciassi, "Highly Dexterous 2-module Soft Robot for Intra-Organ Navigation in Minimally Invasive Surgery", *The International Journal of Medical Robotics and Computer Assisted Surgery*, Vol. 14, No. 1, p. e1875, 2018.

APPENDIX A: TENSILE AND FRICTION TEST RESULTS

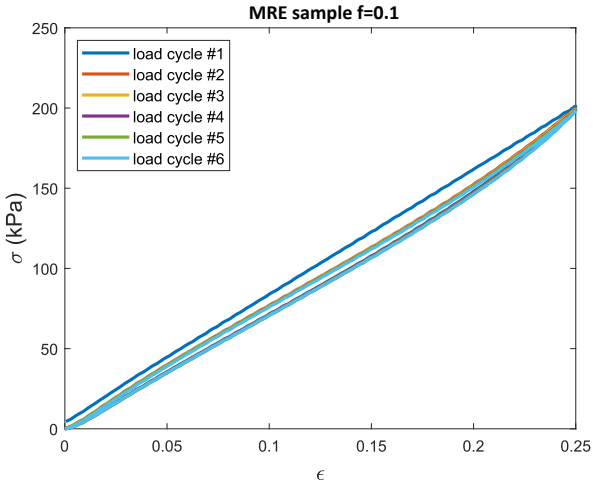

Figure A.1. Stress vs. strain curves of a six-cycle tensile test for the MRE sample when f=0.1.

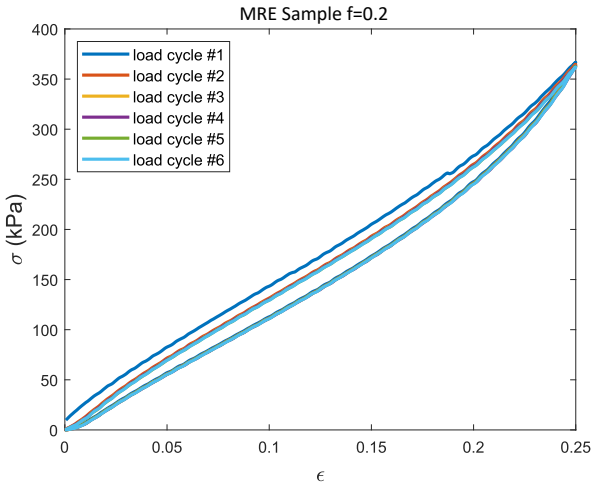

Figure A.2. Stress vs. strain curves of a six-cycle tensile test for the MRE sample when f=0.2.

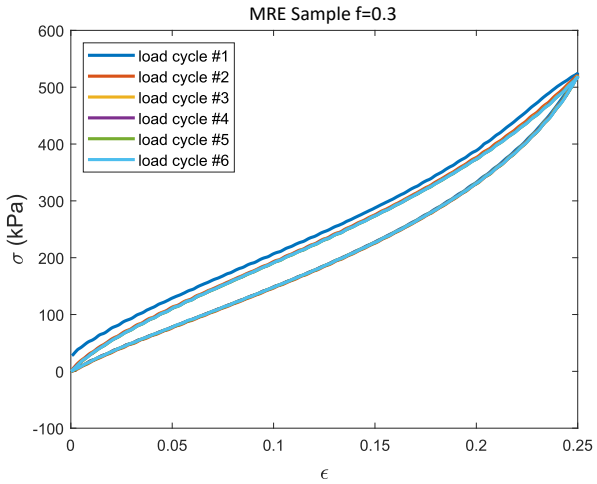

Figure A.3. Stress vs. strain curves of a six-cycle tensile test for the MRE sample when f=0.3.

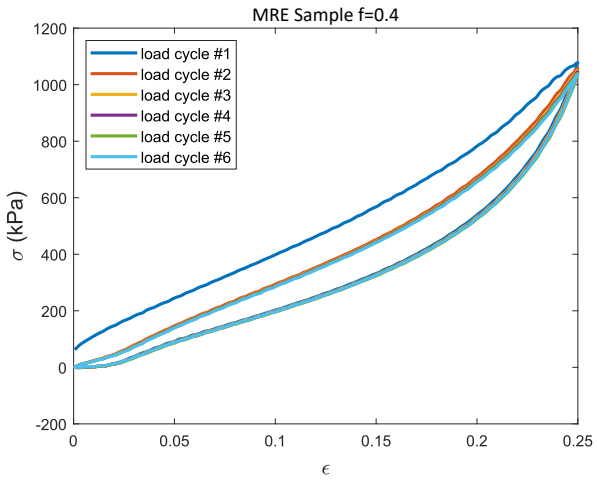

Figure A.4. Stress vs. strain curves of a six-cycle tensile test for the MRE sample when f=0.4.

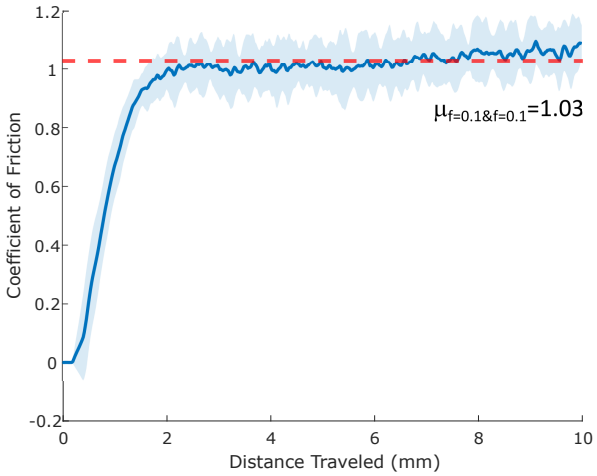

Figure A.5. Coefficient of friction results between the MRE sample (f)=0.1 and the MRE sample (f)=0.1.

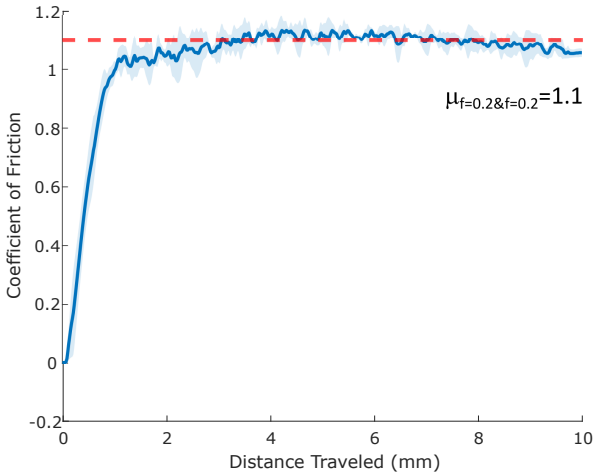

Figure A.6. Coefficient of friction results between the MRE sample (f)=0.2 and the MRE sample (f)=0.2.

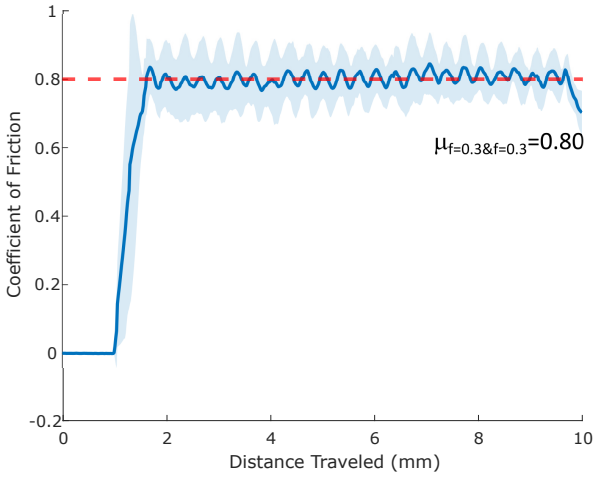

Figure A.7. Coefficient of friction results between the MRE sample (f)=0.3 and the MRE sample (f)=0.3.

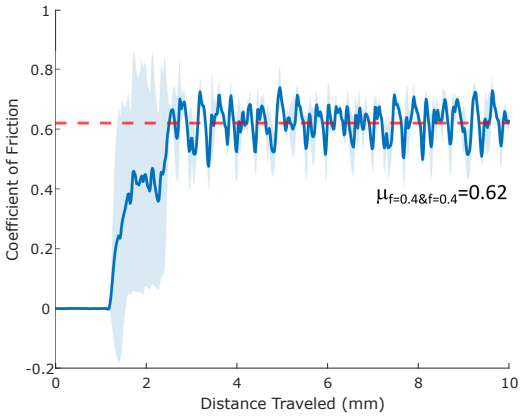

Figure A.8. Coefficient of friction results between the MRE sample (f)=0.4 and the MRE sample (f)=0.4.

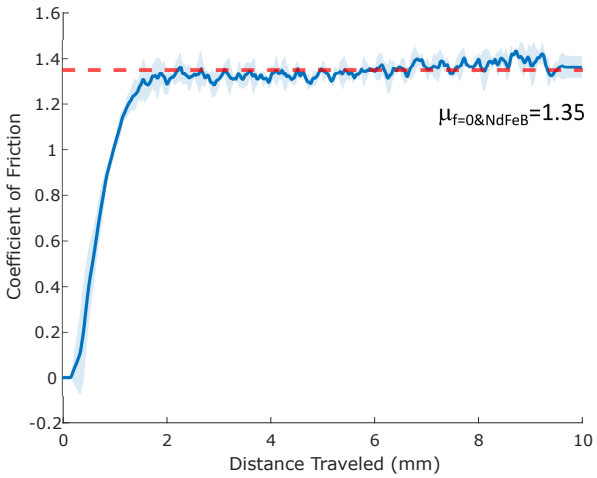

Figure A.9. Coefficient of friction results between the MRE sample (f)=0 and the NdFeB.

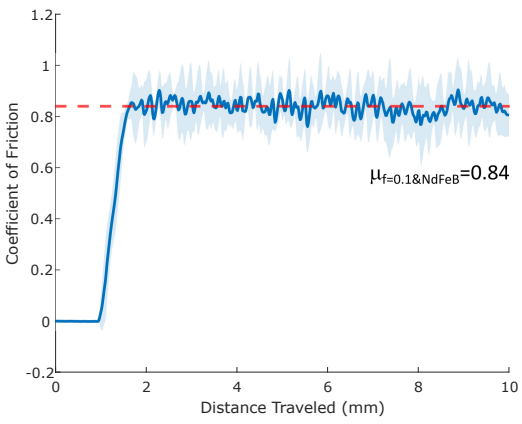

Figure A.10. Coefficient of friction results between the MRE sample (f)=0.1 and the NdFeB.

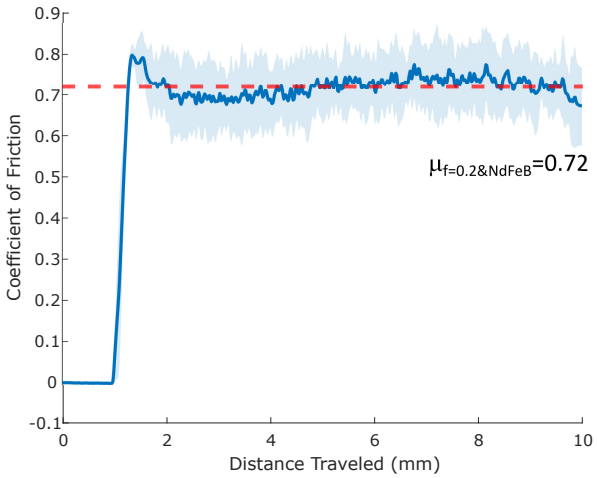

Figure A.11. Coefficient of friction results between the MRE sample (f)=0.2 and the NdFeB.

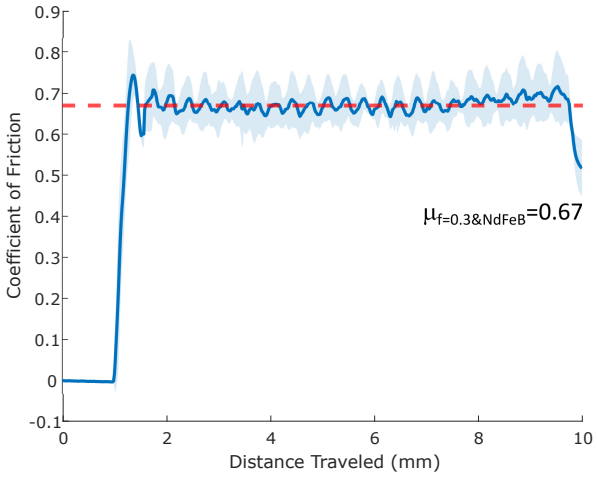

Figure A.12. Coefficient of friction results between the MRE sample (f)=0.3 and the NdFeB.

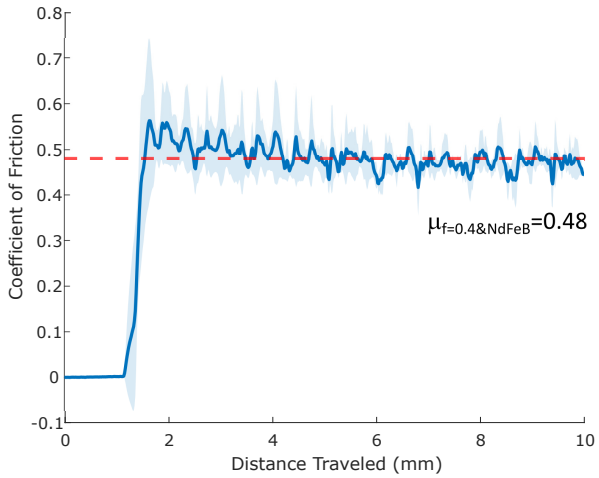

Figure A.13. Coefficient of friction results between the MRE sample (f)=0.4 and the NdFeB.